Ph.D. Thesis

# Realization of superconducting bulk magnets with higher magnetic field gradient to provide a quasi-zero gravity space on earth

March 2021

Keita Takahashi
*Division of Fundamental and Applied Sciences,*
*Graduate school of Science and Engineering, Iwate University*

# Contents

# Chapter 1

# Introduction

# 1.1 Fundamentals of bulk superconducting materials

## 1.1.1 Development of superconducting bulk materials

Bulk superconductors such as (RE)BaCuO (RE: rare earth elements or Y) or $MgB_2$ can be utilized as the so-called trapped field magnet (TFM) that can "trap" a magnetic field over several Tesla by exploiting the flux pinning effect of Type-II superconductors. The magnitude of the trapped field, $B_T$, increases depending on its critical current density, $J_c$, and its sample size, $d$, according to Bean's critical state model as follows [1].

$$B_T \propto J_c \cdot d. \tag{1}$$

An experimental $J_c(B, T)$ data, measured from a small sample of a bulk superconductor shows that the maximum supercurrent induced inside the bulk is determined upon a certain condition with a finite magnetic field, $B$, and a temperature, $T$ [2]. Thus, to enhance $B_T$ in such TFMs, the crystallization process refinement is a fundamental issue for realizing a higher $J_c$ and a larger sample size. To magnetize the bulk, the magnetizing technique must be performed. A field-cooled magnetization (FCM) is a typical conventional method, in which the external magnetic field is applied to the bulk with a certain temperature over a critical temperature, $T_c$, and then decreased to zero Tesla after the bulk is cooled under $T_c$. This, hence, includes both the cooling process and the magnetizing process. The higher trapped field would be obtained for a lower temperature, *e.g.*, from 2 T at 77 K to 9 T at 40 K, which depends its $J_c$ capability [3]. This trapped field can be sustained inside the bulk quasi-permanently once it is magnetized and kept at a constant temperature. The magnetic field profile becomes a conical shaped with a peak at the center because of the overlap of an induced, circumferential supercurrent inside the bulk.

Regarding to some issues for the trapped field enhancement, it has been reported that the mechanical fracture sometimes happens during the magnetization process exploiting a particular large magnetic field over 10 T [4]. The internal mechanical stress, such as the radial stress, $\sigma_r$, and hoop stress, $\sigma_\theta$, exerts on a bulk element during the magnetization [5]. Generally, a crack would occur along the characteristic direction of the crystal alignment due to the principal component of $\sigma_\theta$. To avoid the mechanical fracture during magnetization process, the bulk must be reinforced by metal ring and/or epoxy resin.

The trapped field capability can be estimated based on a numerical assumption. The numerical results of the trapped field at the intermediate position of the stacked, disc shaped GdBaCuO bulk pair magnetized with FCM would be over 20 T at a lower temperature below 40 K [6]. The maximum of the trapped field is equivalent to the applied field; hence, can be increased if a larger applied field can

be provided by an external magnetizing coil magnet. To date, the achieved, record-high trapped field is 17.6 T at 22.5 K, in which a two-stack GdBaCuO bulk pair was reinforced using outer shrink-fit, stainless-steel rings and laminations [6]. In this sense, the optimized reinforcement and thermal stability must be required to realize a higher trapped field. There is a limit in the trapped field enhancement according to the tripartite relation between Electromagnetic field, Temperature and Mechanical stress as shown in figure 1-1.

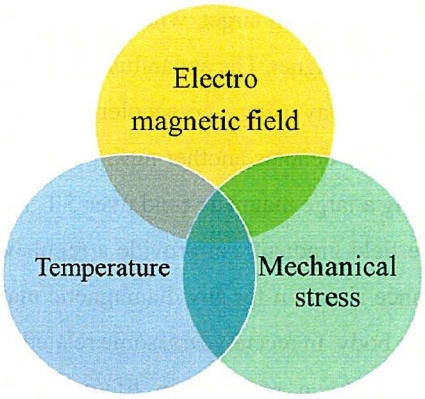


Figure 1-1. Tripartite balance relation between Electromagnetic field, Temperature and Mechanical stress, which stands on the trapped field enhancement for superconducting bulk magnets.

On contrary to TFMs, the magnetic lens using the same bulk material, can provide a concentrated field higher than an external applied field by exploiting the diamagnetic effect of Type-II superconductors. In this case, the bulk needs to be machined into a conical-shaped cylinder with slits. The zero field-cooled magnetization (ZFCM) is used for the magnetization, where the bulk is kept under $T_c$ at all the times to prevent the flux penetration into the bulk itself. It is reported that a concentrated field of 12 T at 20 K was achieved with an applied field of 8 T using an external superconducting coil magnet [7].

The development of the magnetizing technique is essential to utilize bulk superconductors as TFMs or magnetic lenses. On the contrary to the slower FCM and ZFCM, pulsed-field magnetization (PFM) is a more practical, faster magnetizing technique, which incorporates the ZFCM process that is completed within milliseconds using a pulsed magnetic field by a conventional solenoid coil. The most significant issue in this PFM process is known that the heat generation due to the magnetic flux movement would degrade the resultant trapped field after magnetization. To date, the record-high $B_T$ of 5.2 T on the surface by using a modified multi pulse technique with soft iron yokes [8], and 5.3 T at the intermediate position between a two stacked GdBaCuO bulk pair at 30 K by using an optimized two-step pulse sequence [9], were achieved, respectively. Those $B_T$ values is lower by one-third in comparison with that by FCM due to the complex flux movement during the magnetizing process. It has been reposted that the trapped field enhancement can be done even from views of external

magnetizing condition, such as exploiting soft iron yokes [10] and changing the shape of pulsed field [11].

### 1.1.2 Applicational target of bulk superconductors

Figure 1-2 summarizes the potential applicational field of bulk superconductors, which is divided into three regions: Magnet application, Magnetic levitation application and Conductor application. These areas can be classified into the existing target, where the bulk materials can be a candidate to replace or co-exist with a conventional magnet. The apparatus can use the bulk magnets with magnetic fields with several Tesla in an efficient way using a cryocooler or any coolants such as liquid nitrogen at 77 K. On the other hand, the author denotes another new, potential target, high field application, which can be realized by only using a large magnetic field over 5 T. It is known that a large magnetic field in combination with a large field gradient can provide a repulsive force against gravity on the Earth and achieve a counter-balance situation for any diamagnetic materials such as water, common metals and even cells of the human body. In recent years, some related studies, exploiting the so-called "magnetic microgravity condition", have reported in life/medical sciences such as biological characterization [12] and protein crystallization [13], in which a conventional Nd-Fe based permanent magnet or large-scale superconducting magnets are used. It is expected that superconducting technologies relating to bulk magnets create a state-of-the-art innovation that can contribute significantly to the Sustainable Development Goals (SDGs) in different regions including the medical science, space biology, environment and energy.

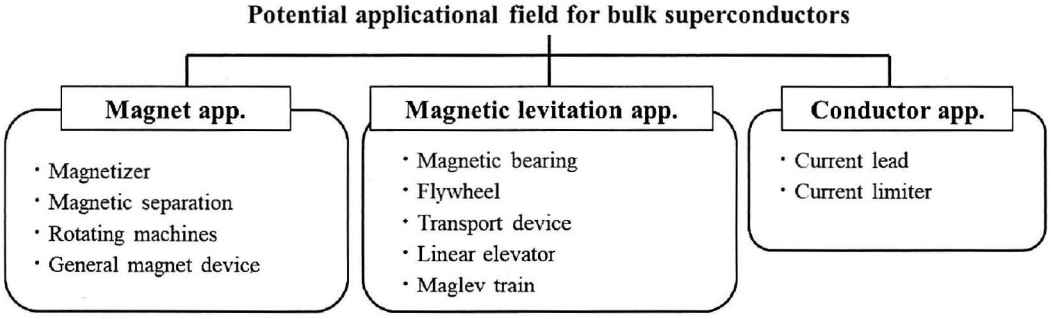


Figure 1-2. Potential applicational field of bulk superconductors, which is divided into three regions: Magnet application, Magnetic levitation application and Conductor application.

## 1.2 Preface

Superconducting technologies have satisfied several demands for high magnetic fields. The most significant issue is that such a comparatively large magnetic field value has been realized only in a specialized facility by only using conventional, large-scale superconducting magnets [14]. For practical uses, it is desirable for the magnetic source to be lightweight, mobile, and cost-effective as a desktop-type apparatus, and preferably cryogen-free, *i.e.*, operating without the need for any coolant such as liquid helium.

The exploration of practical use of TFM can be classified into three phases: fabrication, magnetization, and applications [15]. Such experimental work has showed the significant potential of such TFMs as a powerful magnetic source. However, its configuration would not be appropriate for practical use in applications, which sometimes require a large magnetic field and/or gradient product to be provided in an open space inside or outside vacuum chamber. Hence, in this study, the author suggests two types of a new trapped field magnet, a hybrid trapped field magnet lens (HTFML), which can generate a concentrated field higher than the applied field, and a high gradient-type TFM (HG-TFM), which focuses on the enhancement of the magnetic field gradient product. These devices deserve to be unique that suggests a new pathway to enhance the trapped field from the viewpoint of the magnetizing method in contrast to conventional approaches that depend on the superconducting properties of the bulk itself. Additionally, these new compact magnets can provide the magnetic field in an open space inside/outside the vacuum chamber. Now, since the prototype device can be installed even in a laboratory scale, further applicational studies would be conducted in a more realistic condition towards the industrial application, in comparison with previous explorations using conventional magnets.

This Ph.D. thesis summarizes six papers published since 2018 to 2021, relating to the development of the HTFML and its applicational aspect for the magnetic separation, and another concept of the HG-TFM. A concept of such hybrid-type TFMs was first considered using a numerical simulation in an efficient way, and then the experimental validation was performed. Important results of each chapter are summarized in the following.

### Chapter 2: A new concept of a hybrid trapped field magnet lens

In this chapter, a new concept of the HTFML is proposed. The HTMFL exploits the "vortex pinning effect" of an outer superconducting bulk cylinder, which is magnetized as a TFM using field-cooled magnetization (FCM), and the "diamagnetic shielding effect" of an inner bulk magnetic lens to generate a concentrated magnetic field higher than the trapped field from the TFM in the bore of the magnetic lens. This requires that, during the FCM process, the outer cylinder is in the normal state ($T$

> $T_c$) and the inner lens is in the superconducting state ($T < T_c$) when the external magnetizing field is applied, followed by cooling to an appropriate operating temperature, then removing the external field. This is explored for two potential cases: 1) exploiting the difference in $T_c$ of two different bulk materials ("case-1"), *e.g.*, $MgB_2$ ($T_c$ = 39 K) and GdBaCuO ($T_c$ = 92 K) or 2) using the same material for the whole HTFML, *e.g.*, GdBaCuO, but utilizing individually controlled cryostats, the same cryostat with different cooling loops or coolants, or heaters that keep the outer bulk cylinder at a temperature above $T_c$ to achieve the same desired effect. The HTFML is verified using numerical simulations for "case-1" using an $MgB_2$ cylinder and GdBaCuO lens pair and for "case-2" using a GdBaCuO cylinder and GdBaCuO lens pair. As a result, the HTFML could reliably generate a concentrated magnetic field $B_c$ = 4.73 T with the external magnetizing field $B_{app}$ = 3 T in the "case-1, and a higher $B_c$ = 13.49 T with higher $B_{app}$ = 10 T in the "case-2," respectively. This could, for example, be used to enhance the magnetic field in the bore of a bulk superconducting NMR/MRI system to improve its resolution.

This idea was applied for opened patent serial No. 2019-125710, "hybrid trapped field magnet lens device" [16].

## Chapter 3: Design Optimization of a Hybrid Trapped Field Magnet Lens (HTFML)

In this chapter, a design optimization of the inner GdBaCuO magnetic lens within the GdBaCuO TFM cylinder in the HTFML was carried out using numerical simulations based on the finite element method, in order to maximize the concentrated magnetic field. The HTFML with an optimized shape and size achieved a concentrated magnetic field of $B_c$ = 5.6 and 12.8 T at the center of the lens for applied magnetic fields of $B_{app}$ = 3 and 10 T, respectively. A maximum tensile stress of +135 MPa exists in the outer GdBaCuO TFM cylinder during the magnetizing process for $B_{app}$ = 10 T, which exceeds the fracture strength of the bulk. This result suggests that mechanical reinforcement is necessary to avoid mechanical fracture under such high magnetic field conditions.

## Chapter 4: Experimental realization of a hybrid trapped field magnet lens using a GdBaCuO magnetic lens and $MgB_2$ bulk cylinder

This chapter presents the experimental realization of the HTFML using a GdBaCuO magnetic lens and $MgB_2$ trapped field magnet cylinder. A maximum concentrated magnetic field of $B_c$ = 3.55 T was achieved at the central bore of the HTFML after removing an applied field of $B_{app}$ = 2.0 T at T = 20 K. For higher $B_{app}$, the $B_c$ value was not enhanced because of a weakened lens effect due to magnetic flux penetration into the bulk GdBaCuO material comprising the lens. The enhancement of the trapped field using such an HTFML for the present experimental setup is discussed in detail.

## Chapter 5: Experimental realization of a 10 T-class, all-(RE)BaCuO hybrid trapped

**field magnet lens**

In this chapter, all-(RE)BaCuO hybrid trapped field magnet lens HTFML has been verified experimentally using only one cryocooler and a special technique named the "loose contact method". In the experimental setup, only the inner magnetic lens was tightly connected to the cold stage and cooled at all times, and the outer TFM cylinder was loosely connected to the cold stage before the magnetizing process by introducing a gap between the outer TFM and cold stage of the cryocooler. As a result, the superconducting state for zero-field cooled magnetization (ZFCM) of the inner magnetic lens and the non-superconducting (normal) state for field-cooled magnetization (FCM) of the outer TFM cylinder can co-exist at the same time. A maximum concentrated field of $B_c = 9.8$ T was achieved for the magnetizing process with an applied field of $B_{app} = 7$ T in the present HTFML, consistent with the numerical estimation in our previous conceptual study. These results validate the HTFML concept as a compact and desktop-type magnet device that can provide 10 T-class magnetic field enhancement from the viewpoint of the magnetizing method. However, during magnetization with a higher $B_{app}$ of 10 T, thermal instability of the outer stacked TFM cylinder caused flux jumps to occur, resulting in mechanical fracture of multiple bulks. These results suggest that the further development of a practical cooling method that can realize a stable and controllable cooling process for each part of the HTFML is necessary based on fundamental studies relating to the thermal stability of the large stacked TFM cylinder.

## Chapter 6: Simulation study for magnetic levitation in pure water exploiting the ultra-high magnetic field gradient product of a hybrid trapped filed magnet lens (HTFML)

In this chapter, a new additional advantage of the HTFML is proposed numerically, which could be applicable for magnetic levitation and separation. The HTFML device consisting of GdBaCuO bulk cylinder and GdBaCuO magnetic lens, after the magnetization process from an applied field, $B_{app}$ = 10 T, can generate a maximum trapped field, $B_c$ = 11.4 T, as well as an ultra-high magnetic field gradient product, $B_z \cdot dB_z/dz$, over $\pm$3000 T$^2$/m at $T_s$ = 20 K, which is higher than that of existing superconducting magnets (SM) and large-scale hybrid magnets (HM). Through detailed numerical simulations, the HTFML device is considered for magnetic separation of a mixture of precious metal particles (Pt, Au, Ag and Cu) dispersed in pure water, by exploiting the magneto-Archimedes effect. The HTFML can be realized as a compact and mobile desktop-type superconducting bulk magnet system and there are a wide range of potential industrial applications, such as in the food and medical industries.

## Chapter 7: A conceptual study of a High Gradient Trapped Field Magnet (HG-TFM) toward providing a quasi-zero gravity space on Earth

In this chapter, a new concept of a High Gradient Trapped Field Magnet (HG-TFM) is proposed. The HG-TFM is made from (RE)BaCuO bulk superconductors, in which slit ring bulks (slit-TFMs) are tightly stacked with TFM cylinders (full-TFMs), and state-of-the-art numerical simulations were used to investigate the magnetic and mechanical properties in detail during and after magnetization. A maximum value of the magnetic field gradient product of $B_z \cdot dB_z/dz$ = 6040 $T^2/m$ was obtained after conventional field cooled magnetization (FCM) with an applied field, $B_{app}$, of 10 T of the HG-TFM with 60 mm in outer diameter and 10 mm in inner diameter. This value may be the highest value ever reported compared to any other magnetic sources. The $B_z \cdot dB_z/dz$ value increased with decreasing inner diameter of the HG-TFM and with increasing $B_{app}$ during FCM. The electromagnetic stress in the HG-TFM during the FCM process mainly results from the hoop stress along the circumferential direction. The simulations suggested that there is no fracture risk of the bulk components during FCM from 10 T in a proposed realistic configuration of the HG-TFM where both TFM parts are mounted in Al-alloy rings and the whole HG-TFM is encapsulated in a steel capsule. A quasi-zero gravity space can be realized in the HG-TFM with a high $B_z \cdot dB_z/dz$ value in an open space outside the vacuum chamber. The HG-TFM device can act as a compact and cryogen-free desktop-type magnetic source to provide a large magnetic force and could be useful in a number of life/medical science applications, such as protein crystallization and cell culture.

This idea was applied for closed patent serial No. 2020-180228, "High gradient-type trapped field magnet device" [17].

## Chapter 8: Conclusion

In the final chapter, the conclusion of this research is summarized. The development requirement of a desktop-type, bulk magnet device is also suggested towards the potential application for crystallization system.

## 1.3 References


[1] Bean C P 1962 Magnetization of Hard Superconductors *Phys. Rev. Lett.* **8** 250.

[2] Ainslie M D and Fujishiro H 2019 *Numerical Modelling of Bulk Superconductor Magnetization. IOP Expanding Physics* (Bristol: IOP Publishing).

[3] Teshima H, Morita M, Arayashiki T, Naito T and Fujishiro H 2013 *Phys. Proc.* **45** 61-64.

[4] Miyamoto T, Nagashima K, Sakai N and Murakami M 2000 Direct measurements of mechanical properties for large-grain bulk superconductors *Physica C* **340** 41-50.

[5] Johansen T H and Shantsev D V 2003 Magnetostrictive behaviour of thin superconducting disks *Supercond. Sci. Technol.* **16** 1109.

[6] Huang K *et al.* 2020 Composite stacks for reliable >17 T trapped fields in bulk superconductor magnets *Supercond. Sci. Technol.* **33** 02LT01.

[7] Zhang Z Y, Matsumoto S, Teranishi R and Kiyoshi T 2013 Improving the properties of GdBaCuO magnetic lenses by adopting a new design and resin impregnation *Supercond. Sci. Technol.* **26** 045001.

[8] Fujishiro H, Tateiwa T, Fujiwara A, Oka T and Hayashi H 2006 Higher trapped field over 5 T on HTSC bulk by modified pulse field magnetizing *Physica C* **445-448** 334-338.

[9] Zhou D *et al.* 2018 Exploiting flux jumps for pulsed field magnetization *Supercond. Sci. Technol.* **31** 105005.

[10] Takahashi K, Ainslie M D, Fujishiro H, Naito T, Shi Y-H, Cardwell D A 2017 Trapped field properties of a Y–Ba–Cu–O bulk by pulsed field magnetization using a split coil inserted by iron yokes with various geometries and electromagnetic properties *Physica C* **536** 1-10.

[11] Ida T, Li Z, Miki M, Watasaki M and Izumi M 2018 Waveform Control Pulse Magnetization for HTS Bulk With Flux Jump *IEEE Trans. Appl. Supercond.* **28** 6801905.

[12] Durmus N G *et al.* 2015 Magnetic levitation of single cells *PNAS* **112** E3661-3668.

[13] Wada H *et al.* 2012 Application of High-Field Superconducting Magnet to Protein Crystallization *Phys. Procedia Technol.* **36** 953-957.

[14] Yin D-C 2015 Protein crystallization in a magnetic field *Prog. Cryst. Growth Chract. Mater.* **61** 1-26.

[15] Durrell J H, Ainslie M D, Zhou D, Vanderbemden P, Bradshaw T, Speller S, Filipenko M and Cardwell D A 2018 Bulk superconductors: a roadmap to applications *Supercond. Sci. Technol.* **31** 103501.

[16] Japanese patent application: No. 2019-125710, "hybrid trapped field magnet lens device".

[17] Japanese patent application: No. 2020-180228, "High gradient-type trapped field magnet device".

# Chapter 2

# A new concept of a hybrid trapped field magnet lens

## 2.1 Preface of Chapter 2

The superconducting characteristics of REBaCuO bulks continue to be enhanced due to the introduction of strong pinning centers and the improvement of crystal growth techniques, which have resulted in increased critical current density, $J_c$ [1, 2]. As a result, such bulks exhibit higher trapped field capabilities using field-cooled magnetization (FCM) and have significant potential for practical applications as high-strength trapped field magnets (TFMs) capable of generating magnetic field of several Tesla.

Figure 2-1(a) shows the time sequence of conventional FCM of superconducting bulks to utilize them as TFMs (the case shown is for a cylindrical ring bulk superconductor). Although the trapped field, $B_T$, of REBaCuO bulks, which can be estimated from the $J_c(B, T)$ characteristics, could be over 20 T at 20 K in a bulk pair [3], the mechanical strength of the brittle ceramic material restricts the practical maximum trapped field of such TFMs experimentally. Such TFMs, in which the field is trapped using the strong "vortex pinning effect" of the material, require a high, stationary magnetic field to magnetize them and they can trap fields nearly the same or slightly lower than the applied field, $B_{app}$, using FCM, but such high fields are only available from specialized magnets at a limited number of facilities worldwide.

Figure 2-1(b) shows the time sequence of magnetizing process for a conventional bulk superconducting magnetic lens, for which zero-field-cooled magnetization (ZFCM) is used. The existence of slits in the superconducting hollow cone is essential to suppress the current along the circumferential direction and to concentrate the magnetic flux. A concentrated field of $B_c$ = 12.42 T has been achieved at 20 K for a background field of $B_{app}$ = 8 T using a bulk GdBaCuO magnetic lens [4] and $B_c$ = 30.4 T has been achieved at the center of the lens in higher background field of $B_{app}$ = 28.3 T [5]. Using a bulk $MgB_2$ magnetic lens, a concentrated field of $B_c$ = 2.18 T at 4.2 K has also been achieved for a background field of $B_{app}$ = 1 T [6]. Mechanical reinforcement of the magnetic lens and the avoidance of the flux jump are necessary to achieve the magnetic lens effect stably [7]. Since the magnetic lens effect vanishes after the applied field decreased to zero, the external magnet must be operated continuously, which consumes a large amount of energy.

In this chapter, the author proposes a new concept of a "hybrid trapped field magnet lens (HTFML)", consisting of a cylindrical bulk TFM using the "vortex pinning effect," combined with a bulk magnetic lens using the "diamagnetic shielding effect". The HTFML can reliably generate a magnetic field at the center of the magnetic lens higher than the trapped field in the single cylindrical bulk TFM and the external magnetizing field, even after the externally applied field decreases to zero. This concept requires that, during the FCM process, the outer cylinder is in the normal state ($T > T_c$) and the inner lens is in the superconducting state ($T < T_c$) when the external magnetizing field is applied, followed

by cooling to an appropriate operating temperature, then removing the external field. This is explored for two potential cases: 1) exploiting the difference in $T_c$ of two different bulk materials ("case-1"), *e.g.*, $MgB_2$ ($T_c$ = 39 K) and GdBaCuO ($T_c$ = 92 K) or 2) using the same material for the whole HTFML, *e.g.*, GdBaCuO, but utilizing individually-controlled cryostats, the same cryostat with different cooling loops or coolants, or heaters that keep the outer bulk cylinder at a temperature above $T_c$ to achieve the same desired effect. The effectiveness and superiority of the HTFML is verified using numerical simulations for two cases: "case-1" using an $MgB_2$ cylinder and REBaCuO lens pair, and "case-2" using a REBaCuO cylinder and REBaCuO lens pair. The concentrated magnetic field in the HTFML changes depending on the superconducting characteristics of the bulks [8, 9], their shape and size [6], as well as the magnetizing conditions.

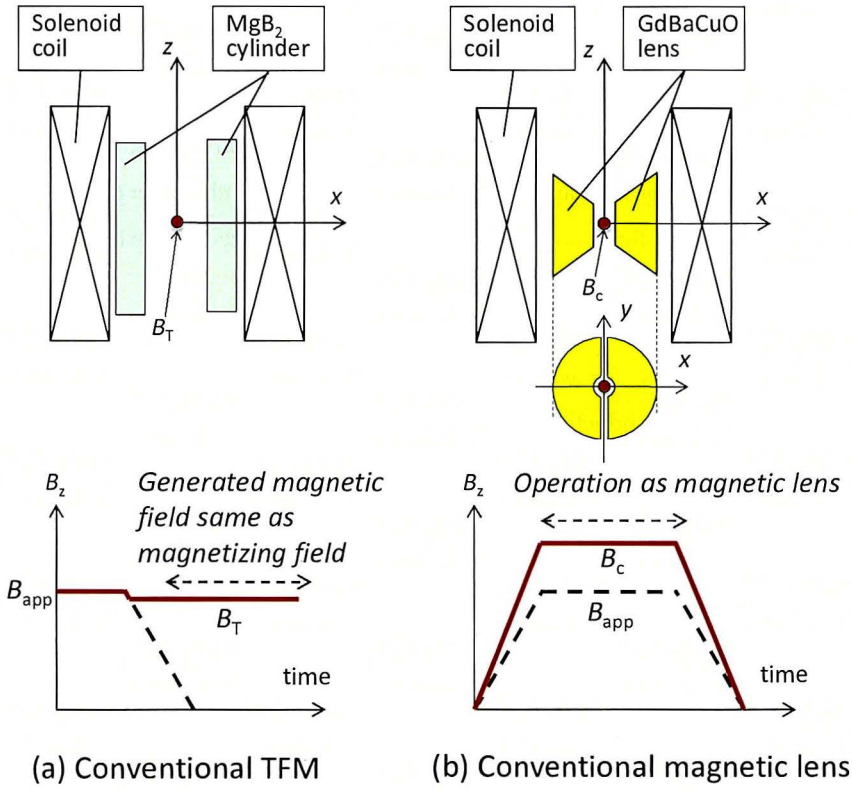


Figure 2-1. Time sequence of (a) conventional magnetizing process of field-cooled magnetization (FCM) of superconducting bulks to utilize them as TFMs and (b) magnetizing process of zero-field magnetization (ZFCM) for a conventional superconducting bulk magnetic lens.

## 2.2 Numerical simulation framework

The following numerical simulation framework for the magnetizing process of the HTFML has been developed. A schematic view of the three-dimensional (3D) numerical model and the relevant dimensions are shown in figure 2-2, in which the superconducting cylinder is made from bulk $MgB_2$ and the superconducting magnetic lens is made from bulk GdBaCuO. This model is abbreviated as "case-1". The bulk $MgB_2$ cylinder is 60 mm in outer diameter (O.D.), 40 mm in inner diameter (I.D.) and 80 mm in height (H). The shape of the magnetic lens is referred from [7], so that the present numerical framework explains the concept of the HTFML based on such a typical lens geometry (as shown in figure 2-2), but importantly two slits exist that are 10° wide. The $MgB_2$ cylinder and GdBaCuO lens are magnetized by a solenoid coil of 170 mm in O.D., 120 mm in I.D. and 200 mm in H. Another example is also provided, in which both the superconducting cylinder and magnetic lens are made from bulk GdBaCuO, which is abbreviated as "case-2". The numerical simulation results for "case-1" and "case-2" are presented in Sections 2.4.1 and 2.4.2, respectively.

Commercial software, Photo-EDDY (Photon Ltd, Japan), was used to analyze the magnetic field profile during the magnetization process, combined with Photo-THERMO to maintain a constant temperature for each bulk component. Electromagnetic phenomena during the magnetization process are described by the fundamental equations shown elsewhere in detail [10-12]. The *E-J* power law is assumed to describe the nonlinear electrical properties of the superconducting bulk:

$$E = E_c \left(\frac{J}{J_c}\right)^n \qquad (2\text{-}1)$$

where $E_c$ ($=10^{-4}$ $Vm^{-1}$) is the characteristic electric field. $n = 20$ for the GdBaCuO bulk and $n = 100$ for the $MgB_2$ bulk are used [13]. The numerical simulation results depend strongly on the $J_c(B, T)$ characteristics of the superconductor [14-16]. For this study, the $J_c(B)$ characteristics for the GdBaCuO bulk are based on the equation presented by Jirsa *et al.* to represent the so-called 'fish-tail' or 'peak' effect found in such superconducting materials [17, 12],

$$J_c(B) = J_{c1}\exp\left(-\frac{B}{B_L}\right) + J_{c2}\frac{B}{B_{max}}\exp\left[\frac{1}{\alpha}\left(1-\left(\frac{B}{B_{max}}\right)^{\alpha}\right)\right]. \qquad (2\text{-}2)$$

The values for the parameters $J_{c1}$, $B_L$, $J_{c2}$, $B_{max}$ and $\alpha$ at 20 and 40 K used in the model are shown in table 2-1, respectively.

The $J_c(B)$ of the $MgB_2$ bulk is described by the following equation [18],

$$J_c(B) = J_{c0}\exp\left[-\left(\frac{B}{B_0}\right)^{\beta}\right] \quad , \qquad (2\text{-}3)$$

where $J_{c0}$, $B_0$ and $\beta$ are fitting parameters, which are summarized in table 2-2. Isothermal conditions are assumed while ramping down the field because the magnetization process is slow; hence, a constant, homogeneous temperature is assumed in the model.

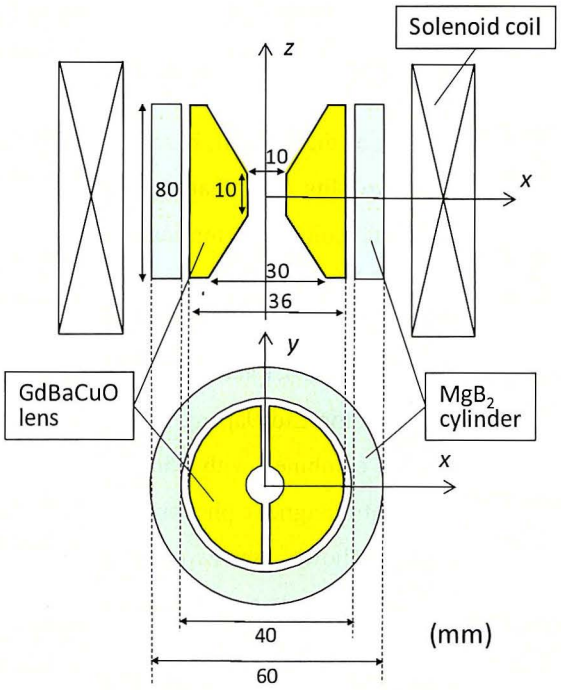


Figure 2-2. Numerical model and dimensions of the $MgB_2$ cylinder, GdBaCuO magnetic lens and solenoid magnetizing coil for "case-1". The $MgB_2$ cylinder is replaced by a GdBaCuO cylinder in "case-2".

Table 2-1. Numerical parameters for the $J_c(B)$ characteristics of the bulk GdBaCuO material at 20 and 40 K using equation (2).

| $T$ (K) | $J_{c1}$ (A/m$^2$) | $B_L$ (T) | $J_{c2}$ (A/m$^2$) | $B_{max}$ (T) | $\alpha$ |
|---|---|---|---|---|---|
| 40 | $3.5 \times 10^9$ | 0.9 | $2.7 \times 10^9$ | 6.0 | 0.8 |
| 20 | $9.0 \times 10^9$ | 1.5 | $5.4 \times 10^9$ | 8.0 | 0.5 |

Table 2-2. Numerical parameters for the $J_c(B)$ characteristics of the bulk $MgB_2$ material at 20 K using equation (3).

| $T$ (K) | $J_{c0}$ (A/m$^2$) | $B_0$ (T) | $\beta$ |
|---|---|---|---|
| 20 | $4.3 \times 10^9$ | 1.1 | 1.5 |

## 2.3 Magnetizing procedure

First, the magnetizing process is described for the following time step sequence, from (1) to (5), for the HTFML for "case-1", in which the bulk $MgB_2$ cylinder and the bulk GdBaCuO magnetic lens are used. Figure 2-3 shows the time sequence of (a) the temperature, $T$ and (b) the external field, $B_{ex}$, and concentrated magnetic field, $B_c$, at the center of the magnetic lens. The magnetizing applied field, $B_{app}$, corresponds to the maximum value of $B_{ex}$.

(1) The bulk $MgB_2$ cylinder and the bulk GdBaCuO lens are cooled from 100 K to $T_H = 40$ K, which is higher than the superconducting transition temperature of $MgB_2$, $T_c = 39$ K, but lower than that of GdBaCuO ($T_c = 92$ K). In this stage, the $MgB_2$ cylinder is in the normal state and the GdBaCuO lens is in the superconducting state (step 0).

(2) The external magnetic field, $B_{ex}$, is ramped up linearly at 0.222 T/min. over 5 steps (steps 1 to 5) up to $B_{app}$, which corresponds to zero-field cooling magnetization (ZFCM) of the GdBaCuO lens. The magnetic field, essentially higher than $B_{app}$ because of the shielding effect by the magnetic lens, completely penetrates the $MgB_2$ cylinder and the magnetic field is concentrated at the center of the lens.

(3) The temperatures of both $MgB_2$ cylinder and GdBaCuO lens are then decreased to $T_L = 20$ K, which is lower than the $T_c$ of $MgB_2$.

(4) $B_{ex}$ is decreased linearly at 0.222 T/min. over 5 steps (steps 6 to 10) down to zero. During this process, the $MgB_2$ cylinder is magnetized by FCM and magnetic flux is trapped in the cylinder. The magnetic field concentration effect slightly decreases due to the decrease of external field. However, a magnetic field at the center of the magnetic lens still remains due to the existence of the trapped field in the $MgB_2$ cylinder.

(5) As a result, HTFML can reliably generate a magnetic field higher than $B_T$ of the single cylindrical TFM and $B_{app}$, even after $B_{ex} = 0$.

There are some examples of a practical cooling system using the difference in $T_c$ of two superconducting components for an aircraft motor design [19] and a magnetic levitation application [20].

In "case-2", in which both the superconducting cylinder and magnetic lens are made from bulk GdBaCuO, (1) and (2) above are changed as follows, labelled at (1') and (2'):

(1') The bulk GdBaCuO cylinder is maintained at 100 K (dotted orange line in figure 2-3) and the bulk GdBaCuO magnetic lens is cooled to $T_H = 40$ K (blue line in figure 2-3). Hence, the bulk GdBaCuO cylinder is in the normal state and the bulk GdBaCuO lens is in the superconducting state (step 0).

(2') The external magnetic field, $B_{ex}$, is increased linearly over 5 steps (steps 1 to 5) up to $B_{app}$, and the magnetic field, essentially equal to $B_{app}$, completely penetrates the GdBaCuO cylinder, but the GdBaCuO lens is magnetized by ZFC.

In the next section, the results of the numerical simulation for "case-1" and "case-2" are presented to prove the effectiveness of the HTFML.

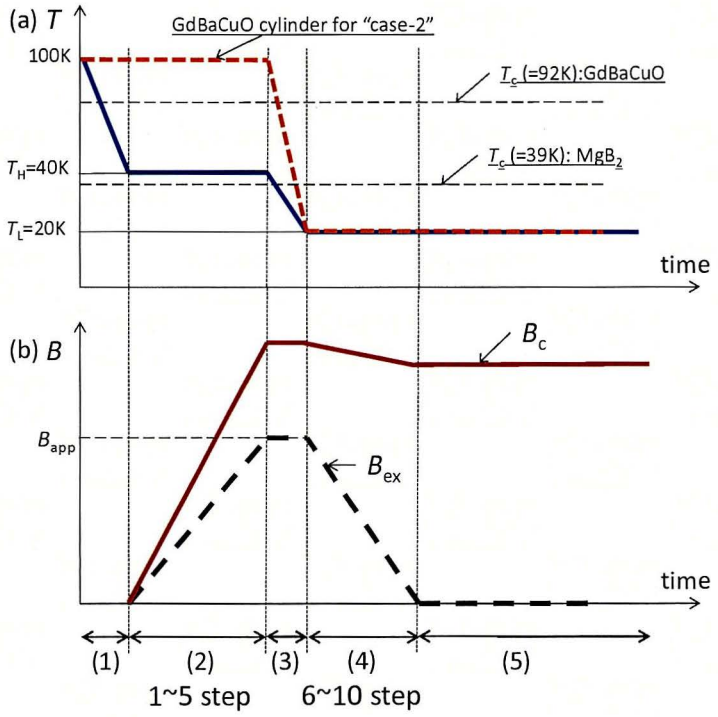


Figure 2-3. Time step sequence of (a) the temperature, $T$ and (b) the external field, $B_{ex}$, and concentrated magnetic field, $B_c$, at the center of magnetic lens for "case-1", in which an $MgB_2$ cylinder and GdBaCuO magnetic lens are used. In "case-2", the temperature of the GdBaCuO lens follows the blue line and the GdBaCuO cylinder follows the dotted orange line in the upper panel (see text).

## 2.4 Simulation result and discussion

### 2.4.1 "Case-1": $MgB_2$ cylinder – GdBaCuO lens

Figure 2-4 shows the time step dependence of the magnetic field profile along the $x$-direction across the center of the lens during (a) the ascending stage and (b) the descending stage of ZFCM of the GdBaCuO lens under an applied field, $B_{app}$ = 3 T in "case-1", which incorporates FCM of the $MgB_2$ cylinder. In figure 2-4(a), during the ascending stage from steps 0 to 5, the concentrated magnetic field, $B_c$, at the center of the GdBaCuO lens was enhanced with increasing $B_{ex}$ owing to the diamagnetic shielding effect of the GdBaCuO lens. It can be found that there is little or no flux penetration in the GdBaCuO lens region ($r$ = $\pm$5 ~ 18 mm) in this case applying a relatively low magnetic field of 3 T by a magnetizing coil. The magnetic flux intrudes into the lens from inner periphery rather than outer edge because of the magnetic flux concentration, which will be discussed later for higher $B_{app}$ in "case-2". In this ascending stage, the GdBaCuO lens is under ZFCM conditions at 40 K; however, the $MgB_2$ cylinder is in the normal state and is not yet utilized as a TFM. In figure 2-4(b), during the descending stage of $B_{ex}$ from steps 5 to 10, which incorporates FCM of the $MgB_2$ cylinder during ZFCM of the GdBaCuO lens, $B_c$ decreased with decreasing $B_{ex}$, but becomes stable after the external field decreases to zero and a magnetic field is trapped in the $MgB_2$ cylinder. As a result, $B_c$ at the center of the GdBaCuO lens settled to $B_c$ = 4.73 T at the final step (step 10), which can be realized quasi-permanently by the novel combination of the "vortex pinning effect" and "diamagnetic shielding effect" of superconducting bulk materials.

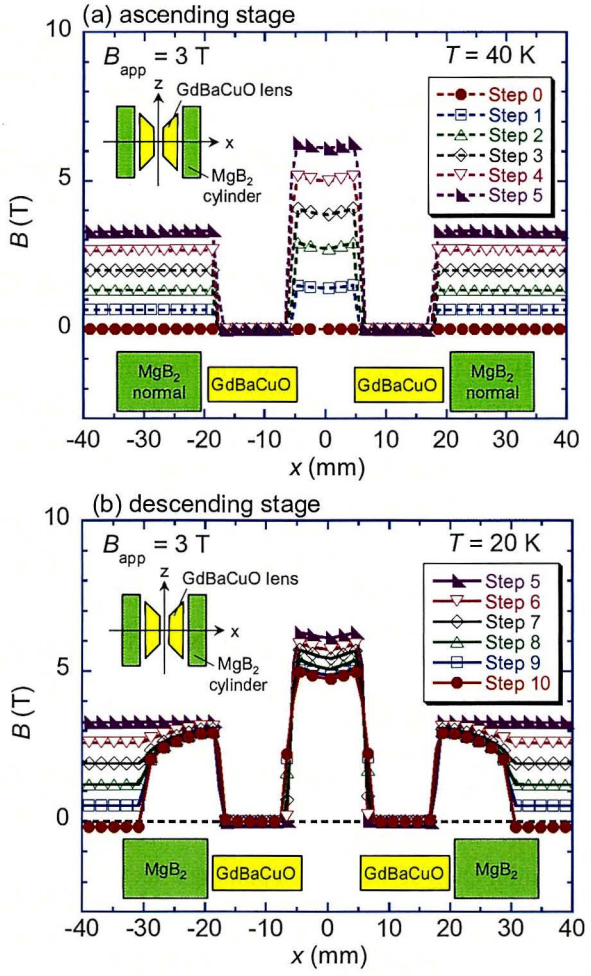


Figure 2-4. Time step dependence of the magnetic field profile along the $x$-direction across the center of the lens during (a) the ascending stage and (b) the descending stage of ZFCM of the GdBaCuO lens under an applied field, $B_{app}$ = 3 T in "case-1", which incorporates FCM of the $MgB_2$ cylinder.

Figures 2-5(a) and 2-5(b), respectively, show the time step dependence of the magnetic field profiles along the $x$-direction across the center of the lens during the ascending and descending stages of FCM for an applied field, $B_{app}$ = 3 T for only the $MgB_2$ cylinder, without the GdBaCuO lens, in "case-1". In figure 2-5(a), when only the $MgB_2$ cylinder is considered, the $B_T$ value is nearly the same as $B_{ex}$ in the ascending stage (steps 0 to 5), and attains a maximum value $B_{ex}$ = 3 T at step 5 with a uniform magnetic field profile along $x$-direction, which corresponds to the applied field profile generated by the externally magnetizing coil. During this ascending stage, the $MgB_2$ cylinder is in the normal state. In figure 2-5(b), in the descending stage (steps 6 to 10), the trapped field, $B_T$, of the $MgB_2$ cylinder by FCM decreases slightly with decreasing $B_{ex}$, and settles to a final value of $B_T$ = 2.85 T at the final step (step 10) in the bore of $MgB_2$ cylinder, now acting as a TFM that can continue to provide the trapped field quasi-permanently. One of the particular characteristics of the HTFML device is to

utilize the trapped field from this TFM, instead of requiring a continuously applied field from an external magnetizing coil. Thus, it is useful to be able to reproduce a magnetic field profile similar to that which might be produced by a magnetizing solenoid coil when we use the TFM as a source of magnetic field for the HTFML, for further concentration of the magnetic flux in the HTFML. This could, for example, allow the realization of higher resolution in a compact and cryogen-free NMR/MRI system using annular REBaCuO superconducting bulks [21, 22].

To achieve the highest concentrated field in the lens, the GdBaCuO magnetic lens must, in the ideal case, completely shield the magnetic field from its interior. However, since it is a type II superconductor, some magnetic flux will penetrate the material, depending on its $J_c(B, T)$ characteristics (and hence operating temperature), as well as its geometry, during the HTFML magnetizing procedure. Figures 2-6(a) and 2-6(b), respectively, show the time step dependence of the magnetic field profiles along the $x$-direction across the center of the lens during the ascending and descending stages of ZFCM for an applied field, $B_{app}$ = 3 T for the only GdBaCuO lens without the $MgB_2$ cylinder in "case-1". Figure 2-6(a) is exactly the same as figure 2-4(a), in which $B_c$ at the center of the GdBaCuO lens was enhanced gradually with increasing $B_{ex}$ in the ascending stage from step 0 to 5. In figure 6(b), in the descending stage from step 6 to 10, it can be seen that there is some flux penetration into the inner edge of GdBaCuO lens at around $r = \pm 5 \sim 7$ mm from step 7 even for a relatively low applied field of 3 T during ZFCM. The magnetic field reached eventually becomes -0.46 T at the center of the GdBaCuO lens at the final step (step 10) after ZFCM, resulting in a reduction from the ideal of the GdBaCuO lens shielding effect in those regions where the magnetic flux penetrates during ZFCM. Thus, to maximize the lens's shielding, and hence its ability to concentrate the magnetic field, the flux penetration should be minimized.

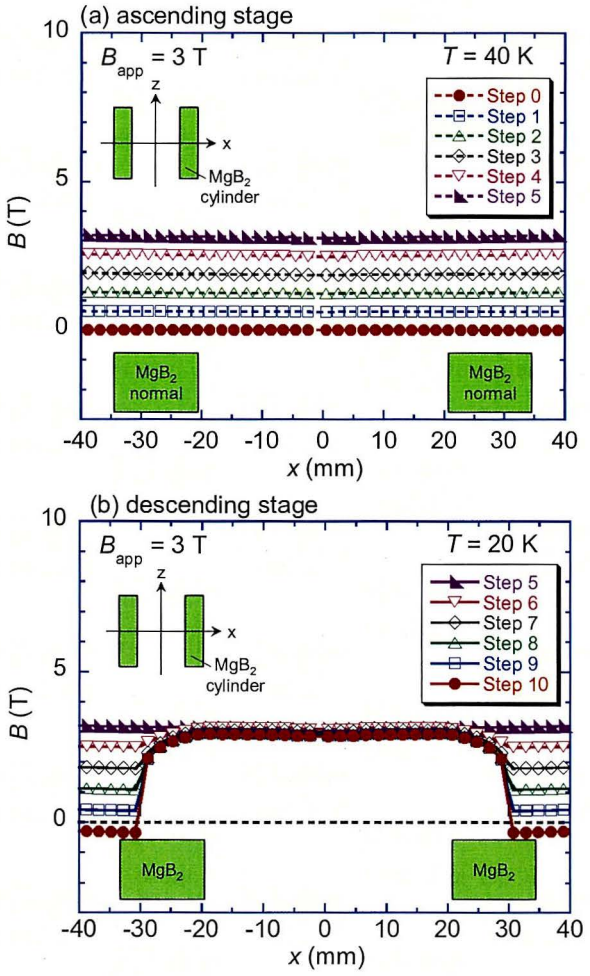


Figure 2-5. Time step dependence of the magnetic field profile along the *x*-direction across the center of the lens during (a) the ascending stage and (b) the descending stage of FCM of the $MgB_2$ cylinder without the GdBaCuO lens for an applied field, $B_{app}$ = 3 T at 20 K.

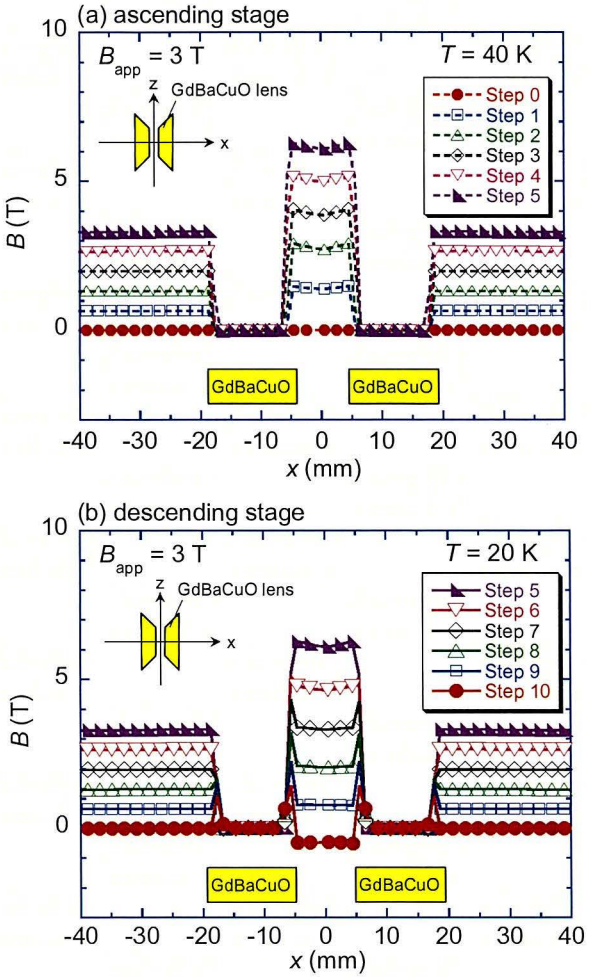


Figure 2-6. Time step dependence of the magnetic field profile along the $x$-direction across the center of the lens during (a) the ascending stage and (b) the descending stage of ZFCM of the GdBaCuO lens without the $MgB_2$ cylinder for an applied field, $B_{app}$ = 3 T at 20 K.

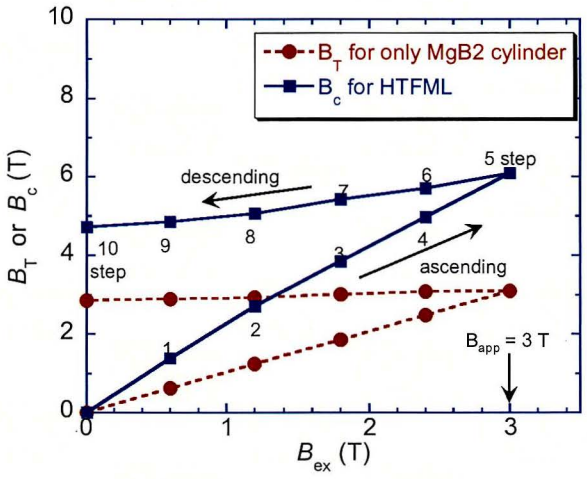


Figure 2-7. Concentrated magnetic field, $B_c$, at the center of the magnetic lens as a function of the external field, $B_{ex}$, for $B_{app}$ = 3 T. The trapped field, $B_T$, at the center of the $MgB_2$ cylinder for the case without the GdBaCuO lens extracted from figure 2-5 is also shown.

Figure 2-7 shows the concentrated magnetic field, $B_c$, at the center of magnetic lens as a function of external field, $B_{ex}$, for $B_{app}$ = 3 T, which was extracted from figure 2-4. The trapped field, $B_T$, at the center of the $MgB_2$ cylinder was also extracted from figure 2-5 for the case without the GdBaCuO lens, which clarifies the effectiveness of the HTFML. For only $MgB_2$ cylinder, the $B_T$ value is nearly the same as $B_{ex}$ in the ascending stage from step 0 and attains a maximum value $B_{ex}$ = 3 T at step 5. The $B_T$ value is then 2.85 T at the final step (step 10) once $B_{ex}$ = 0, showing that 3 T is a reasonable value to fully magnetize the $MgB_2$ cylinder by FCM at 20 K. In the case of the HTFML using both the $MgB_2$ cylinder and GdBaCuO lens, $B_c$ at the center of the GdBaCuO lens was enhanced up to 6.10 T at step 5 due to the shielding effect of lens and settled to $B_c$ = 4.73 T at the final step (step 10), which is higher than both $B_{app}$ from the magnetizing coil and $B_T$ from the $MgB_2$ TFM. These results indicate the superiority of the proposed HTFML device, which can reliably generate the concentrated magnetic field higher than the applied field by the external magnetizing coil and the trapped field of the TFM, even after removal of the external field.

### 2.4.2 "Case-2": GdBaCuO cylinder – GdBaCuO lens

In this subsection, the other example of "case-2" using a REBaCuO cylinder and REBaCuO lens pair for further concentration of the trapped magnetic flux is explored.

Figure 2-8 shows the time step dependence of the magnetic field profile along the $x$-direction across the center of the lens during (a) the ascending stage and (b) the descending stage for $B_{app}$ = 10 T in "case-2". In this case, it should be noted that the temperature of the GdBaCuO cylinder and lens must be controlled individually. Similar results were shown previously for "case-1" in figure 2-4(a), where the magnetic field profile was shown during the ascending stage of ZFCM for $B_{app}$ = 3 T for the GdBaCuO lens from steps 0 to 5 (noting that the $MgB_2$ cylinder is in the normal state). In figure 2-8(a), the $B_c$ value was enhanced up to $B_c$ = 16 T at the center of the lens at step 5 when applying $B_{app}$ = 10 T. The GdBaCuO lens could retain its shielding effect even in a higher external magnetic field of 10 T, although the magnetic shielding effect weakens with increasing applied field due to further penetration of magnetic flux [5]. In figure 2-8(b), during the descending stage (steps 5 to 10), the GdBaCuO cylinder maintains a trapped field similar to $B_{app}$ at the final step (step 10) as it is magnetized by FCM, but below its full capability based on its high $J_c$-$B$ characteristics at 20 K. The $B_c$ value gradually decreased during the descending stage and settled to a final value of $B_c$ = 13.5 T at the center of the lens.

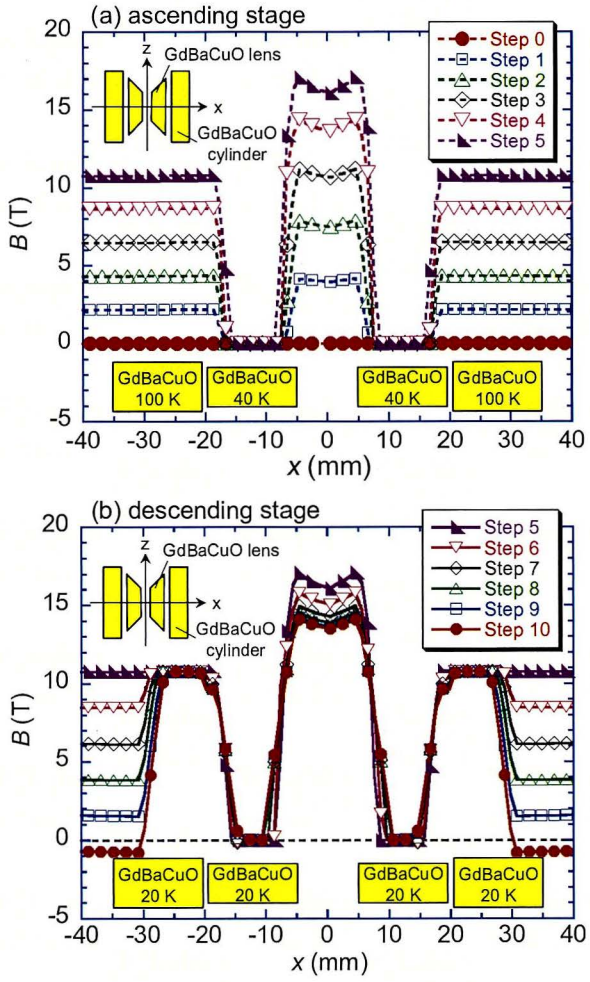


Figure 2-8. Time step dependence of magnetic field profile along the $x$-direction across the center of the lens during (a) the ascending stage and (b) the descending stage for $B_{app}$ = 10 T in "case-2".

Figure 2-9 shows the time step dependence of the concentrated magnetic field, $B_c$, and external field, $B_{ex}$, at the center of the GdBaCuO lens for $B_{app}$ = 3, 6 and 10 T for "case-2". Table 2-3 summarizes the concentrated magnetic field, $B_c$, trapped field from the TFM, $B_T$, when only considering the TFM cylinder (*i.e.*, the lens is not present), at the central position at the final step (step 10), and the concentration ratio, $B_c/B_{app}$, in "case-2" extracted from figure 2-9 for each actual $B_{app}$. An accurate value of $B_{app}$ is shown as $B^*_{app}$ = 3.09 T, 6.13 T and 10.18 T in this table, which was named roughly as $B_{app}$ = 3 T, 6 T, 10 T so far. Similar results for "case-1" from figure 2-4 are also shown for comparison. For the lower $B_{app}$ = 3 T, a magnetic field concentration ratio of $B_c/B_{app}$ = 1.70 is achieved at the final step (step 10) in "case-2," which is higher than 1.53 when using the $MgB_2$ cylinder in "case-1". This results from the higher $B_T$ value of 3.09 T in "case-2", where the outside GdBaCuO cylinder was magnetized below its full capability. Furthermore, in "case-2", the concentration ratio decreased with increasing $B_{app}$ from 1.70 for $B_{app}$ = 3 T to 1.33 for $B_{app}$ = 10 T. In figure 2-9, the higher $B_{app}$ resulted in a larger flux creep during the descending stage of FCM of the TFM cylinder and further penetration of magnetic flux in the ZFCM of the GdBaCuO lens. There is a possibility to achieve further enhancement of $B_c$ and $B_c/B_{app}$ by optimization of the magnetic design, including the geometry of the cylinder and lens, and the magnetization conditions, including temperature and applied field. The shielding property of the magnetic lens should be also exploited for further concentration of the trapped field, such as for hollow bulk cylinders [8]. These results show that the effectiveness of the HTFML would be enhanced in terms of the characteristics of the superconducting material(s) used, including the possibility of utilizing new and improved materials, such as $BaFe_2As_2$ ($T_c$ = 38 K) [23, 24].

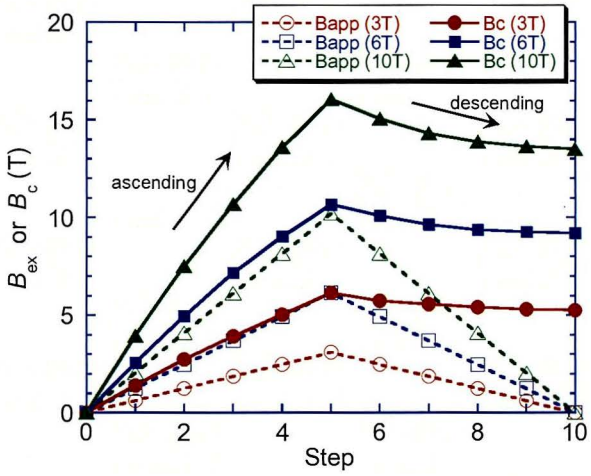


Figure 2-9. Time step dependence of the concentrated magnetic field, $B_c$, at the center of the GdBaCuO lens in the HTFML for $B_{app}$ = 3, 6 and 10 T for "case-2". The external field, $B_{ex}$, generated by the solenoid magnetizing coil is also shown for each $B_{app}$.

Table 2-3. Concentrated magnetic field, $B_c$, trapped field by TFM, $B_T$, at the center of the GdBaCuO lens at the final step (step 10), and magnetic field concentration ratio, $B_c/B_{app}$, in "case-2" extracted from figure 2-9 for each actual applied field, $B^*_{app}$. Similar results for "case-1" from figure 2-4 are also shown for comparison.

| | $B_{app}$ (T) | $B^*_{app}$ (T) | $B_T$ (T) | $B_c$ (T) | $B_c/B_{app}$ |
|---|---|---|---|---|---|
| "case-1" (MgB2 cylinder) | 3 | 3.09 | 2.85 | 4.73 | 1.53 |
| "case-2" (GdBaCuO cylinder) | 3 | 3.09 | 3.09 | 5.25 | 1.70 |
| | 6 | 6.13 | 6.13 | 9.19 | 1.50 |
| | 10 | 10.18 | 10.18 | 13.49 | 1.33 |

## 2.5 Summary of Chapter 2

A new concept of a "hybrid trapped field magnet lens (HTFML)," consisting of a superconducting bulk cylinder TFM using the "vortex pinning effect," combined with a bulk magnetic lens using the "diamagnetic shielding effect," is proposed, which can reliably generate a magnetic field at the center of the magnetic lens higher than the trapped field by TFM and the maximum external magnetizing field, even after the externally applied field decreases to zero. The effectiveness and superiority of the HTFML was verified using numerical simulations for two examples: 1) an $MgB_2$ cylinder and GdBaCuO lens pair ("case-1") and 2) a GdBaCuO cylinder and GdBaCuO lens pair ("case-2"). In "case-1," using the outer $MgB_2$ cylinder and inner GdBaCuO lens pair, the $MgB_2$ cylinder was magnetized by FCM with an applied field, $B_{app} = 3$ T, during the descending stage, also corresponding to ZFCM of the GdBaCuO lens. The trapped field, $B_T = 2.85$ T, in the $MgB_2$ TFM cylinder was concentrated by the introduction of GdBaCuO lens, and a concentrated magnetic field, $B_c = 4.73$ T, was reliably achieved at the center of the lens. In "case-2," using the outer GdBaCuO TFM cylinder and inner GdBaCuO lens pair, in which the GdBaCuO cylinder is held above $T_c$ and the GdBaCuO lens is cooled below $T_c$ for the ascending stage of magnetization, followed by both bulks being cooled below $T_c$ for the descending stage, a higher $B_c = 13.49$ T, was reliably achieved at the center of the magnetic lens for $B_{app} = 10$ T.

The advantages and disadvantages of each HTFML, comparing use of the $MgB_2$ cylinder and the GdBaCuO cylinder are summarized as follows:

"case-1": The $MgB_2$ HTFML only needs one cooling process for the whole device by exploiting the difference in $T_c$ of the two superconducting materials. Its weight would also be lower due to the use of the lighter bulk $MgB_2$ cylinder. However, the trapped field capability is limited in comparison to the GdBaCuO cylinder ("case-2") because of the comparatively inferior $J_c(B)$ characteristics of $MgB_2$ and it must operate at a temperature lower than the superconducting transition temperature of $MgB_2$, $T_c = 39$ K.

"case-2": The all-GdBaCuO HTFML offers higher concentrated fields at temperatures much higher than 39 K, but does require separate cooling of the cylinder and lens parts to obtain the necessary effect and it would weigh more.

This HTFML device could become a standard method for trapped field enhancement in several practical applications using a superconducting bulk and there is a scope for optimization of the magnetic design, including geometry around two bulks, and magnetization conditions, including temperature and applied field. The effectiveness of the HTFML would be enhanced with improvements in the characteristics of the superconducting material(s) used, including the possibility of utilizing new and improved materials such as $BaFe_2As_2$ ($T_c = 38$ K). The device could, for example,

be used to enhance the magnetic field in the bore of a bulk superconducting NMR/MRI system to improve its resolution.

## 2.6 References


[1] Shi Y-H, Namburi D K, Zhao W, Durrell J H, Dennis A R and Cardwell D A 2016 The use of buffer pellets to pseudo hot seed (RE)-Ba-Cu-O-(Ag) single grain bulk superconductors *Supercond. Sci. Technol.* **29** 015010.

[2] Muralidhar M, Sakai N, Chikumoto N, Jirsa M, Machi T, Nishiyama M, Wu Y and Murakami M 2002 New Type of Vortex Pinning Structure Effective at Very High Magnetic Fields *Phys. Rev. Lett.* **89** 237001.

[3] Tomita M and Murakami M 2003 High-temperature superconductor bulk magnets that can trap magnetic fields over 17 tesla at 29 K *Nature* **421** 517–20.

[4] Zhang Z Y, Matsumoto S, Teranishi R and Kiyoshi T 2012 Magnetic field, temperature and mechanical crack performance of a GdBCO magnetic lens *Supercond. Sci. Technol.* **25** 115012.

[5] Choi S, Yoon J-H, Lee B-S, Won M-S, Ok J-W, Zhang Z-Y, Kiyoshi T, Matsumoto S and Lee S-H 2012 Magnetic lens effect using Gd-Ba-Cu-O bulk superconductor in very high magnetic field *J. Appl. Phys.* **111** 07E728.

[6] Zhang Z Y, Choi S, Matsumoto S, Teranishi R, Giunchi G, Albisetti A Figini and Kiyoshi T 2012 Magnetic lenses using different $MgB_2$ bulk superconductors *Supercond. Sci. Technol.* **25** 025009.

[7] Zhang Z Y, Matsumoto S, Teranishi R and Kiyoshi T 2013 Improving the properties of GdBCO magnetic lenses by adopting a new design and resin impregnation *Supercond. Sci. Technol.* **26** 045001.

[8] Lousberg GP, Fagnard JF, Ausloos M, Vanderbemden P and Vanderheyden B 2010 Numerical Study of the Shielding Properties of Macroscopic Hybrid Ferromagnetic/Superconductor Hollow Cylinders *IEEE Trans. Appl. Supercond.* **20** 33-41.

[9] Rabbers J J, Oomen M P, Bassani E, Ripamonti G and Giunchi G 2010 Magnetic shielding capability of $MgB_2$ cylinders *Supercond. Sci. Technol.* **23** 125003.

[10] Fujishiro H and Naito T, 2011 Simulation of temperature and magnetic field distribution in superconducting bulk during pulsed field magnetization *Supercond. Sci. Technol.* **23** 105021.

[11] Fujishiro H, Ainslie M D, Takahashi K, Naito T, Yanagi Y, Itoh Y and Nakamura T 2017 Simulation studies of mechanical stresses in REBaCuO superconducting ring bulks with infinite and finite height reinforced by metal ring during field-cooled magnetization *Supercond. Sci. Technol.* **30** 085008.

[12] Takahashi K, Fujishiro H, Naito T, Yanagi Y, Itoh Y and Nakamura T 2017 Fracture behavior analysis of EuBaCuO superconducting ring bulk reinforced by a stainless steel ring during field-

cooled magnetization *Supercond. Sci. Technol.* **30** 115006.

[13] Fujishiro H, Naito T and Yoshida T 2014 Numerical simulation of the trapped field in $MgB_2$ bulk disks magnetized by field cooling *Supercond. Sci. Technol.* **27** 065019.

[14] Ainslie M D, Zou J, Mochizuki H, Fujishiro H, Shi Y-H, Dennis A R and Cardwell D A 2015 Pulsed field magnetization of 0°–0° and 45°–45° bridge-seeded Y–Ba–Cu–O bulk superconductors *Supercond. Sci. Technol.* **28** 125002.

[15] Ainslie M D and Fujishiro H 2015 Modelling of bulk superconductor magnetization *Supercond. Sci. Technol.* **28** 053002.

[16] Ainslie M D, Zhou D, Fujishiro H, Takahashi K, Shi Y-H and Durrell J H 2016 Flux jump-assisted pulsed field magnetisation of high-$J_c$ bulk high-temperature superconductors *Supercond. Sci. Technol.* **29** 124004.

[17] Jirsa M, Půst L, Dlouhý D and Koblischka M R 1997 Fishtail shape in the magnetic hysteresis loop for superconductors: Interplay between different pinning mechanisms *Phys. Rev.* B **55** 3276–84.

[18] Xiang F X, Wang X L, Xun X, Silva K S B De, Wang Y X and Dou S X 2013 Evidence for transformation from $\delta T_c$ to $\delta l$ pinning in $MgB_2$ by graphene oxide doping with improved low and high field $J_c$ and pinning potential *Appl. Phys. Lett.* **102** 152601.

[19] Masson P J, Breschi M, Tixador P and Luongo C A 2007 Design of HTS Axial Flux Motor for Aircraft Propulsion *IEEE Trans. Appl. Supercond.* **17** 1533-1536.

[20] Patel A, Giunchi G, Albisetti A F, Shi Y, Hopkins S C, Palka R, Cardwell D A and Glowacki B A 2012 High Force Magnetic Levitation Using Magnetized Superconducting Bulks as a Field Source for Bearing Applications *Phys. Procedia* **36** 937-942.

[21] Nakamura T, Tamada D, Yanagi Y, Itoh Y, Nemoto T, Utsumi H and Kose K 2015 Development of a superconducting bulk magnet for NMR and MRI *J. Magn. Reson.* **259** 68-75.

[22] Ogawa K, Nakamura T, Terada Y, Kose K and Haishi T 2011 Development of a magnetic resonance microscope using a high $T_c$ bulk superconducting magnet *Appl. Phys. Lett.* **98** 234101.

[23] Weiss J D, Yamamoto A, Polyanskii A A, Richardson R B, Larbalestier D C and Hellstrom E E 2015 Demonstration of an iron-pnictide bulk superconducting magnet capable of trapping over 1 T *Supercond. Sci. Technol.* **28** 112001.

[24] Ainslie M D, Yamamoto A, Fujishiro H, Weiss J D and Hellstrom E E 2017 Numerical modelling of iron-pnictide bulk superconductor magnetization *Supercond. Sci. Technol.* **30** 105009.

# Chapter 3

# Design Optimization of

# a Hybrid Trapped Field Magnet Lens (HTFML)

## 3.1 Preface of Chapter 3

In this chapter 3, a new concept of a hybrid trapped field magnet lens (HTFML) was proposed, can reliably generate a concentrated magnetic field in the center of the magnetic lens higher than the trapped field of the TFM and the applied magnetic field, even after the external magnetizing field decreases to zero. In this chapter, the optimization of the shape and size of the inner GdBaCuO magnetic lens in the HTFML is carried out using numerical simulations, which is inserted into an outer GdBaCuO TFM cylinder. The mechanical stress during the magnetization process, resulting from the combination of the current and magnetic field in the HTFML, is also analyzed.

## 3.2 Numerical simulation framework

In this chapter, the electromagnetic model presented in our original paper describing the concept of the HTFML [1] is coupled with a mechanical model and is used to further evaluate the performance of the HTFML during the magnetizing process. Figure 3-1 shows the cross-section of the three-dimensional (3D) numerical model of the HTFML. Assuming that the 10 T superconducting solenoid magnet (170 mm in outer diameter (O.D.), 120 mm in inner diameter (I.D.), and 200 mm in height (H)) located in Iwate University is used as the magnetizing coil, the HTFML is assembled in a room temperature bore 100 mm in diameter. The GdBaCuO magnetic lens is inserted inside the GdBaCuO TFM cylinder (60 mm in O.D., 40 mm in I.D., and 60 mm in H). The magnetic lens part has two slits 10° wide along the *y*-direction, whose role is to allow the magnetic flux to intrude into and be concentrated at the center of the lens.

To optimize the shape and the size of the magnetic lens, five variable parameters (outer diameter, OD, inner diameter, ID, inner diameter 2, ID2, outer height, OH, and inner height, IH) are changed independently, which are indicated in figure 3-1. The detailed values of the size of each parameter (OD $\leq$ 36 mm, ID2 $\leq$ 36 mm, OH $\leq$ 60 mm) are shown in Table 3-1, in which an ID = 10 mm is assumed for all optimization procedures to insert a Hall sensor for experiments planned in future work.

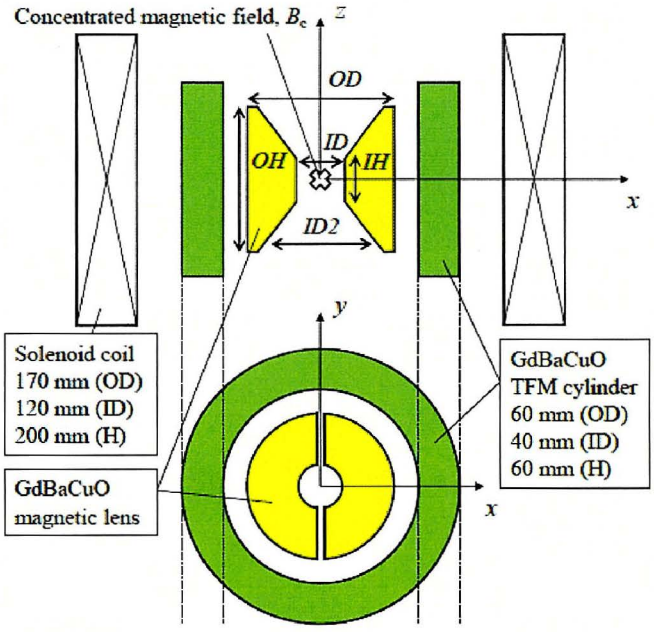


Fig. 3-1. Cross-section of three-dimensional numerical model of an HTFML in a magnetizing solenoid coil.

Table 3-1. Five variable parameters of the GdBaCuO magnetic lens for the design optimization.

| Fig. No. | OD (mm) | ID2 (mm) | ID (mm) | OH (mm) | IH (mm) |
|---|---|---|---|---|---|
| 3-3 (a) | variable | variable | 10 | 45 | 10 |
| 3-3 (b) | 36 | variable | 10 | 45 | 10 |
| 3-3 (c) | 36 | 30 | 10 | variable | 10 |
| 3-3 (d) | 36 | 30 | 10 | 30 | variable |

In the case that both magnetic lens and TFM cylinder are made of the same bulk superconducting material, it is necessary to control the temperature of each part independently. Figure 3-2 shows the schematic view of the time step (*TS*) dependence of the temperature, $T$, of the magnetic lens and the cylindrical TFM, and that of the external magnetic field, $B_{ex}$. The magnetizing procedure of the HTFML comprises the following four stages in this simulation.

1) The temperature of the outer GdBaCuO TFM cylinder is held at $T$ = 100 K (> $T_c$ = 92 K), while the GdBaCuO magnetic lens is cooled to 20 K (step 0).
2) The external magnetic field, $B_{ex}$, is increased linearly up to the maximum magnetic field $B_{app}$ = 3 or 10 T at +0.222 T/min (steps 0–5). The magnetic lens is magnetized under zero-field cooling (ZFC) conditions at 20 K, where the magnetic flux is concentrated in the bore of the lens.
3) The GdBaCuO TFM cylinder is then also cooled to 20 K (< $T_c$) under $B_{app}$, which transitions into the superconducting state (steps 5–6).
4) Finally, $B_{ex}$ is ramped down from $B_{app}$ to zero at -0.222 T/min (steps 6–11). In this process, the GdBaCuO TFM cylinder is magnetized by FCM, which then acts like an external magnetizing coil magnet in a conventional magnetic lens setup, *e.g.*, [2]. As a result, the magnetic flux generated from the TFM cylinder is concentrated in the magnetic lens and a magnetic field higher than $B_{app}$ is still present after the external $B_{ex}$ decreases to zero.

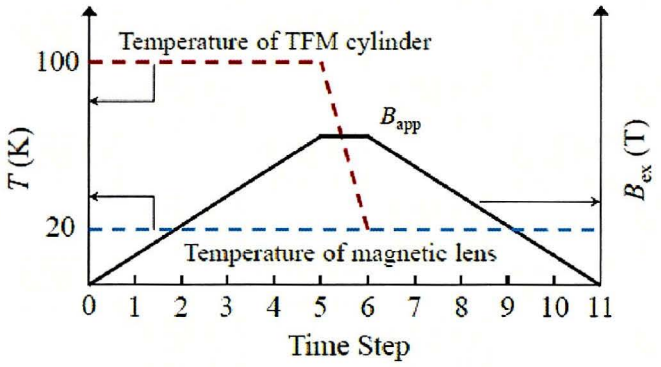


Fig. 3-2. Time step sequence of the temperature, $T$, of the GdBaCuO magnetic lens and GdBaCuO TFM cylinder (left vertical axis), and the external magnetic field, $B_{ex}$ (right vertical axis)

The $n$-power law ($n$ = 20) is used to describe the nonlinear $E$-$J$ characteristic of the bulk [3]. The $J_c(B)$ characteristics at 20 K of the GdBaCuO bulk is defined by the following equation proposed by Jirsa *et al.* [4]

$$J_c(B) = J_{c1}\exp\left(-\frac{B}{B_L}\right) + J_{c2}\frac{B}{B_{max}}\exp\left[\frac{1}{k}\left(1-\left(\frac{B}{B_{max}}\right)^k\right)\right], \qquad (3-1)$$

where $J_{c1}$ = 9.0 × $10^9$ A/m$^2$, $B_L$ = 1.5 T, $J_{c2}$ = 5.4 × $10^9$ A/m$^2$, $B_{max}$ = 8.0 T and $k$ = 0.5 are used for the fitting parameters at 20 K [1, 5]. Elastic behavior can be expressed by Hooke's law, in which the stress tensor, $\sigma_{ij}$, is linearly proportional to strain tensor, $\varepsilon_{ij}$, as follows,

$$\sigma_{ij} = \lambda \cdot e_{kk} \cdot \delta_{ij} + 2G \cdot e_{ij}, \qquad (3-2)$$

$$\lambda = \frac{E \cdot \nu}{(1+\nu)(1-2\nu)}, \qquad (3-3)$$

$$G = \frac{E}{2(1+\nu)}, \qquad (3-4)$$

where $\lambda$ and $G$ are the Lame's coefficients, $\delta_{ij}$ is the Kronecker delta. Young's modulus, $E$ = 100 GPa, and Poisson ratio, $\nu$ = 0.33, are assumed as the mechanical parameters for the REBaCuO bulk [6]. The REBaCuO bulk is also assumed to be an isotropic and linear elastic material. The electromagnetic hoop stress, $\sigma_\theta$, is calculated for each time step of the magnetizing process.

## 3.3 Results and discussion

### 3.3.1 Design optimization of the GdBaCuO magnetic lens

Figure 3-3 shows the concentrated magnetic field, $B_c$, at the center of the magnetic lens ($x = y = z = 0$) for steps 5 and 11 for $B_{app} = 3$ T, as a function of each variable. The magnetic field amplification factor, $B_c/B_{app}$, is also shown on the right axis. In figure 3-3(a), the $B_c$ vs OD relationship is shown, in which the ID2 value is defined as OD minus 6 mm (ID2 = OD − 6 mm), because the ID2 changes depending on the OD value. The $B_c$ value increases linearly with increasing OD, and a $B_c/B_{app}$ of 2.4 is achieved for OD = 36 mm at step 5, where only the magnetic lens is working, and the magnetic flux produced by the magnetizing coil is efficiently concentrated in the bore of the lens. The $B_c$ value at step 11, at which FCM of the outer TFM is finished, is lower than that at step 5 since the external magnetic field decreases during the descending stage and because of flux creep. However, a magnetic field higher than $B_{app} = 3$ T still remains for all cases of OD, which is the advantage of the HTFML.

Figure 3-3(b) shows the ID2 dependence of $B_c$ and $B_c/B_{app}$ at steps 5 and 11 for $B_{app} = 3$ T. For ID2 = 10 mm, *i.e.*, a cylindrical-shaped lens, which is a desirable shape from the viewpoint of machining the lens, the $B_c/B_{app}$ is as small as 1.3. The $B_c$ value increases with increasing ID2, similar to the $B_c$ vs OD relationship shown in figure 3-3(a).

Figure 3-3(c) shows the OH dependence of $B_c$ and $B_c/B_{app}$ at steps 5 and 11 for $B_{app} = 3$ T. With increasing OH, the $B_c$ value increases, takes a maximum for OH = 45 mm, and then decreases slightly for OH = 60 mm, which is the same height as the outer GdBaCuO TFM cylinder. However, there is no significant difference between OH = 30–60 mm. This result means that, in the present situation, OH = 30 mm is enough to maximize the $B_c$ and $B_c/B_{app}$ values and to provide a cost- effective HTFML.

Figure 3-3(d) shows the IH dependence of $B_c$ and $B_c/B_{app}$ at steps 5 and 11 for $B_{app} = 3$ T. For IH = 8 mm, the highest $B_c$ of 5.67 T is achieved at step 11. The inset of figure 3-3(d) shows the cross-section of the magnetic lens for IH = 8 mm, where the intersection of the lines extending from the lens taper corresponds to the lens center ($x = y = z = 0$). This result suggests that an appropriate taper angle for the magnetic lens can maximize the $B_c/B_{app}$ value for a cylindrical TFM.

From the viewpoints of both the magnetic field amplification and cost-effectiveness, and based on these results, it was decided that the optimum shape of the GdBaCuO magnetic lens, which is inserted in the GdBaCuO TFM cylinder (60 mm in O.D., 40 mm in I.D. and 60 mm in H), should be designed with OD = 36 mm, ID2 = 30 mm, ID = 30 mm, OH = 30 mm and IH = 8 mm. Following the same procedure, it was also confirmed that the optimized shape determined by $B_{app} = 3$ T was also effective for the case of $B_{app} = 10$ T, and for the case of outer $MgB_2$ TFM cylinder. That is, the optimum shape of the inner lens depends not on the particular bulk materials used and/or the superconducting properties of the outer TFM cylinder, but only the geometry of the magnetic lens.

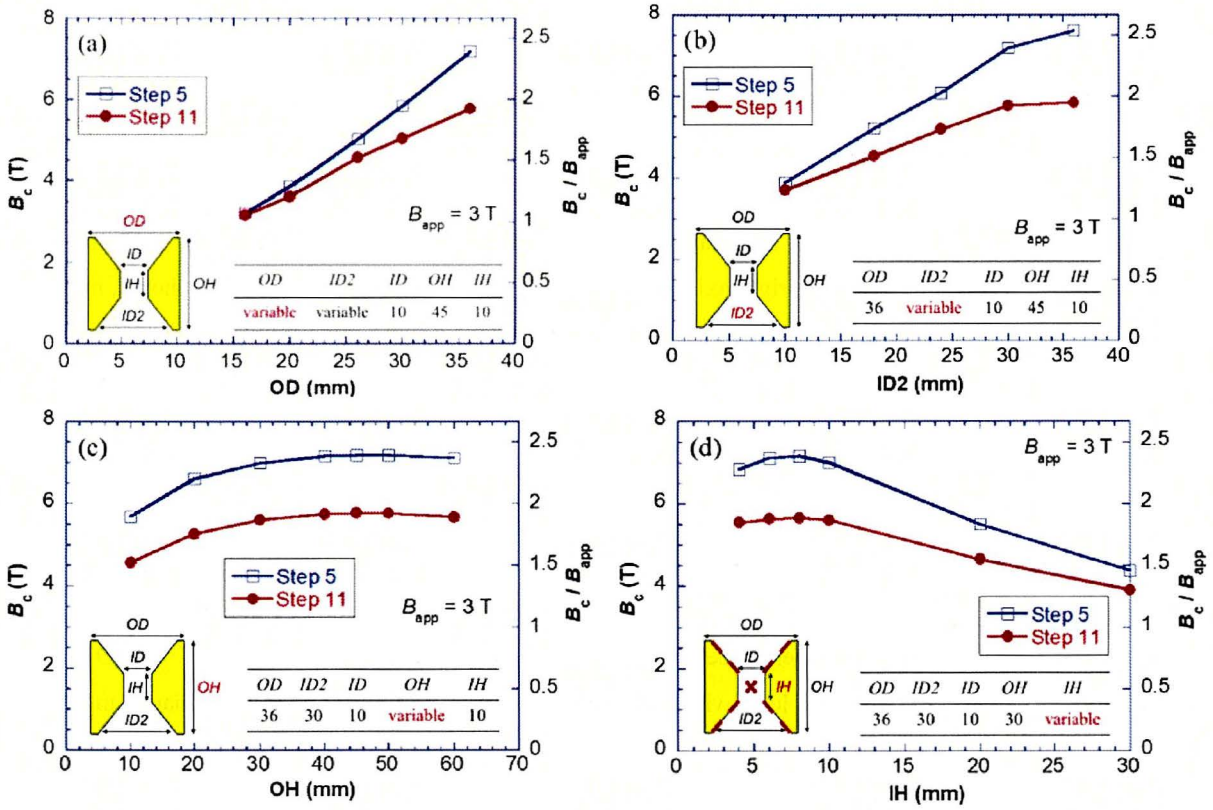


Fig. 3-3. The concentrated magnetic field, $B_c$, at the center of the magnetic lens and the magnetic field amplification factor, $B_c/B_{app}$, as a function of (a) OD, (b) ID2, (c) OH, (d) IH for $B_{app}$ = 3 T.

Figures 3-4(a) and 3-4(b), respectively, show the time step dependence of the magnetic field profile along the $x$-direction across the center of the lens with the optimized design for $B_{app}$ = 3 and 10 T. The contour maps of the magnetic field within the magnetic lens at step 5 are also shown in each figure. The $B_c$ value is enhanced up to 6.9 and 15.5 T at the central region ($-5 < x < 5$) at step 5 for $B_{app}$ = 3 T and 10 T, respectively. The magnetic flux penetration into the GdBaCuO lens from both the inner and outer peripheries can be observed with increasing applied field, as shown in the inset contour maps. As a result, the shielding effect of the GdBaCuO lens weakens in external magnetic fields as high as 10 T. During the descending stage (steps 8 and 11 in the figure), the GdBaCuO TFM cylinder maintains a trapped field similar to $B_{app}$ at the final step (step 11) as it is magnetized by FCM. The $B_c$ value gradually decreases and settles to final values of $B_c$ = 5.6 and 12.8 T, respectively, at the center of the lens.

Figures 3-4(c) and 3-4(d), respectively, show the time step dependence of $B_c$ and $B_c/B_{app}$ at the center of the GdBaCuO lens for $B_{app}$ = 3 and 10 T. In the ascending stage (steps 0–5), $B_c/B_{app}$ increases linearly and reaches 2.3 ($B_c$ = 6.9 T) for $B_{app}$ = 3 T. For $B_{app}$ = 10 T, however, the $B_c/B_{app}$ vs $TS$ curve gradually bends and the $B_c/B_{app}$ value at step 5 decreases to 1.55 ($B_c$ = 15.5 T) due to the weakened

shielding effect of the lens. In the descending stage (steps 6–11), $B_c/B_{app}$ gradually decreases and final values of 1.86 and 1.28 are achieved for $B_{app}$ = 3 and 10 T, respectively.

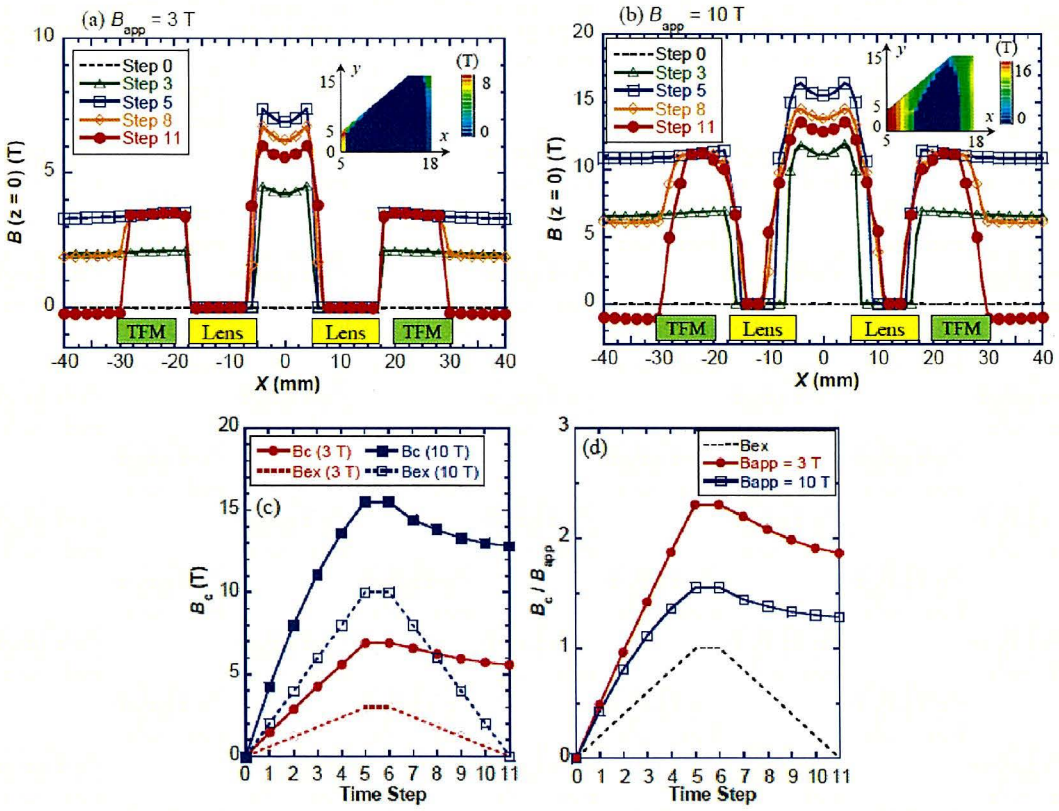


Fig. 3-4. Time step dependence of the magnetic field, $B$, profiles across the center of the HTFML ($z$ = 0) for (a) $B_{app}$ = 3 T and (b) $B_{app}$ = 10 T. Contour maps of the magnetic field profiles at step 5 are also shown in each figure. Time step dependence of (c) the concentrated magnetic field, $B_c$ and (d) the magnetic field amplification factor, $B_c/B_{app}$ for $B_{app}$ = 3 and 10 T.

### 3.3.2 Electromagnetic hoop stress, $\sigma_\theta$, during magnetization

In high-field applications of REBaCuO bulks, mechanical fracture due to large electromagnetic forces must be avoided. Using the coupled electromagnetic-mechanical model, the hoop stress, $\sigma_\theta$, present in the magnetic lens and TFM cylinder in the HTFML was estimated. Figures 3-5(a) and 3-5(b) show the time step dependence of the electromagnetic hoop stress profile, $\sigma_\theta$, across the center of the lens ($z$ = 0) with the optimized design for $B_{app}$ = 3 and 10 T, respectively. During the ascending stage (steps 0–5), a tensile stress exists at the inner periphery of the lens, corresponding to the flux penetration area. The shielding current due to the lens's diamagnetic property results in a compressive stress in the body of the lens.

On the other hand, during the descending stage (steps 6–11), a large tensile stress in the TFM cylinder, resulting from the Lorentz force, increases with increasing time step. The contour map of $\sigma_\theta$ at step 11 is shown in each figure, which details the stress concentration at the inner edge periphery of the TFM cylinder. The maximum $\sigma_\theta$ value reaches +135 MPa at step 11 for $B_{app}$ = 10 T, which exceeds the fracture strength of typical Ag-doped REBaCuO bulk materials (50 ~ 70 MPa) [7, 8]. In the magnetic lens, a maximum tensile stress of +35 MPa exists at the inner periphery of the magnetic lens and a compressive stress exists in other regions. These results suggest that adequate mechanical reinforcement is necessary, at least for the GdBaCuO TFM cylinder, but possibly the magnetic lens as well. The demonstration experiment of an HTFML consisting reinforced GdBaCuO bulks will be conducted based on these simulation results.

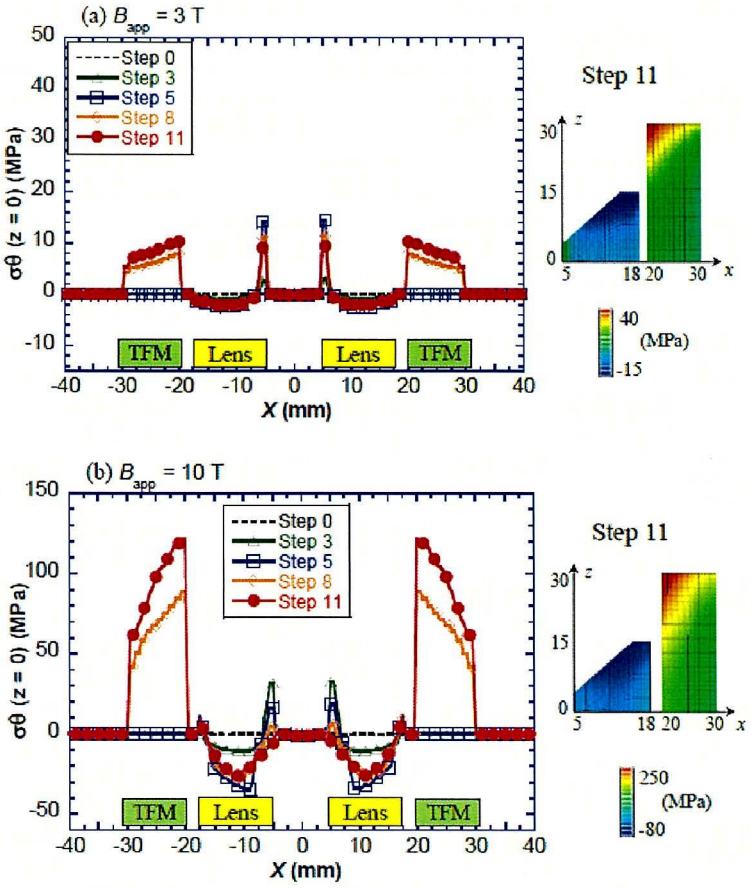


Fig. 3-5. Time step dependence of the electromagnetic hoop stress profile, $\sigma_\theta$, across the center of the HTFML ($z$ = 0) for (a) $B_{app}$ = 3 T and (b) $B_{app}$ = 10 T. Time step dependence of the magnetic field, $B$, profiles across the center of the HTFML ($z$ = 0) for (a) $B_{app}$ = 3 T and (b) $B_{app}$ = 10 T. The contour map of $\sigma_\theta$ at step 11 is also shown in each figure.

## 3.4 Summary of Chapter 3

In this chapter, the optimization of the shape and size of the inner GdBaCuO magnetic lens in a hybrid trapped field magnet lens (HTFML) was carried out using numerical simulations, which is inserted inside an outer GdBaCuO TFM cylinder. The mechanical stress in the HTFML with optimized lens was also analyzed during the magnetizing process. The main conclusions are as follows.

(1) The design optimization of the magnetic lens can be carried out from viewpoints of both the magnetic field amplification and cost-effectiveness.

(2) The HTFML with an optimized lens can achieve concentrated magnetic fields of $B_c$ = 5.6 and 12.8 T at the center of the lens for applied magnetic fields of $B_{app}$ = 3 and 10 T, respectively.

(3) For $B_{app}$ = 10 T, a maximum tensile stress of 35 and 135 MPa exist in the magnetic lens and the TFM cylinder, respectively, during the magnetizing process. These results suggest that adequate mechanical reinforcement is needed in a practical design in order to avoid mechanical fracture at high magnetic fields.

## 3.5 References


[1] K. Takahashi, H. Fujishiro, and M D Ainslie 2018 A new concept of a hybrid trapped field magnet lens *Supercond. Sci. Technol.* **31** 044005.

[2] T. Kiyoshi, S. Choi, S. Matsumoto, T. Asano, and D. Uglietti 2005 Magnetic Flux Concentrator Using Gd-Ba-Cu-O Bulk Superconductors *IEEE Trans. Appl. Supercond.* **19** 2174–2177.

[3] M. D. Ainslie *et al.* 2016 Enhanced trapped field performance of bulk high- temperature superconductors using split coil, pulsed field magnetization with an iron yoke," *Supercond. Sci. Technol.* **29** 074003.

[4] M. Jirsa, L. Ůst, D. Dlouhý and M. R. Koblischka 1997 Fishtail shape in the magnetic hysteresis loop for superconductors: Interplay between different pinning mechanisms *Phys. Rev. B* **55** 3276–3284.

[5] T. Kii *et al.* 2012 Low-temperature operation of a bulk HTSC staggered array undulator *IEEE Trans. Appl. Supercond.* **22** 4100904.

[6] H. Fujishiro *et al.* 2017 Simulation studies of mechanical stresses in REBaCuO superconducting ring bulks with infinite and finite height reinforced by metal ring during field-cooled magnetization *Supercond. Sci. Technol.* **30** 085008.

[7] D. Lee and K. Salama 1990 Enhancements in current density and mechanical properties of Y-Ba-Cu-O/Ag composites *Jpn. J. Appl. Phys.* **29** L2017–2019.

[8] H. Fujimoto and A. Murakami 2012 Mechanical properties of Gd123 superconducting bulks at 77

K *Supercond. Sci. Technol.* **25** 054017.

# Chapter 4

## Experimental realization of a hybrid trapped field magnet lens using a GdBaCuO magnetic lens and $MgB_2$ bulk cylinder

## 4.1 Preface of Chapter 4

In this chapter 2, using numerical simulations, the HTFML was shown to be able to reliably generate a magnetic field in the central bore of the magnetic lens that is higher than both the trapped field in the single cylindrical bulk TFM and the external magnetizing field, even after the externally applied field decreases to zero. For a REBaCuO magnetic lens and $MgB_2$ TFM cylinder, the HTFML could reliably generate a concentrated magnetic field of $B_c = 4.73$ T with an external magnetizing field $B_{app} = 3$ T [1]. In addition, the shape of the magnetic lens in the HTFML has been optimized, and the mechanical stress in the cylinder and lens parts has also been estimated during the magnetizing process in the chapter 3.

In this chapter, the author present, for the first time, the experimental realization of the HTFML using a GdBaCuO magnetic lens and $MgB_2$ TFM cylinder, based on the same magnetizing procedure proposed in [1]. The experimental results are compared with the simulated ones and enhancement of the $B_c$ value in HTFML is discussed in detail.

## 4.2 Experimental procedure

### 4.2.1 Experimental setup

Figure 4-1(a) shows the schematic cross-section of the experimental setup of the HTFML on the cold stage of a refrigerator. The $MgB_2$ cylindrical bulk (60 mm in outer diameter (OD), 40 mm in inner diameter (ID), and 60 mm in height (H)) was fabricated using the infiltration method by Experiments Projects Constructions S. R. I., Italy [2, 3]. Figure 4-1(b) shows the cross-section and top view of the GdBaCuO magnetic lens. The GdBaCuO magnetic lens was prepared by the following process: stacked GdBaCuO cylindrical bulks (OD = 36 mm, ID = 10 mm, H = 30 mm), fabricated using the QMG™ method by Nippon Steel Corporation, Japan [4, 5], were machined into a cone-shape of OD = 30 mm, ID = 10 mm, ID2 = 26 mm, outer height (OH) = 30 mm and inner height (IH) = 8.0 mm, as shown in figure 4-1(b). The dimensions of the bulk magnetic lens were optimized using numerical simulations [6]. Thin slits of width 200 μm was made to disrupt the circumferential flow of the shielding current during the zero-field-cooling (ZFC) process, which plays an important role in magnetic flux concentration for the magnetic lens [1]. When an external magnetic field is applied along the +$z$-axis direction to the GdBaCuO magnetic lens, the same magnetic field penetrates into the central bore from the slits. The shielding current flows as shown by the red arrows in figure 4-1(b) and an additional magnetic field exists along the +$z$-axis direction, mainly due to the counterclockwise shielding current nearest to the central bore. As a result, the magnetic field is enhanced along the +$z$-axis direction, which is then higher than the applied field.

The GdBaCuO magnetic lens was encapsulated in a stainless steel (SS) holder to prevent fracture of the bulk due to the large Lorentz force during the magnetization process and was connected thermally to the cold stage of the refrigerator. The $MgB_2$ cylindrical bulk was reinforced by a SS cylinder (ID = 60 mm, OD = 66 mm and H = 60 mm), and the top SS plate (ID = 36 mm, OD = 66 mm and H = 3 mm), which were effective in preventing mechanical fracture [7, 8]. These SS holders apply a compressive stress to the bulk cylinder and bulk lens during the cooling process from room temperature to the operating temperature (*e.g.*, 20 K) due to the difference in the coefficient of thermal expansion between SS and the bulk superconducting materials. Two CERNOX™ thermometers were attached for monitoring the temperature of the HTFML; one was mounted directly on the top surface of the $MgB_2$ cylinder, and the other was placed on the top surface of the SS holder of the GdBaCuO lens. Thin indium sheets were inserted between the bulks and the cold stage of the refrigerator (or SS holder) to obtain good thermal contact. The temperature of the cold stage was controlled using a Pt-Co thermometer and a resistive heater, attached to bottom surface of the cold stage. The concentrated field, $B_c$, was measured in the central bore of the HTFML by an axial-type Hall sensor (F W Bell, BHA-921). The HTFML device was placed in a vacuum chamber and then evacuated by a vacuum

pump system.

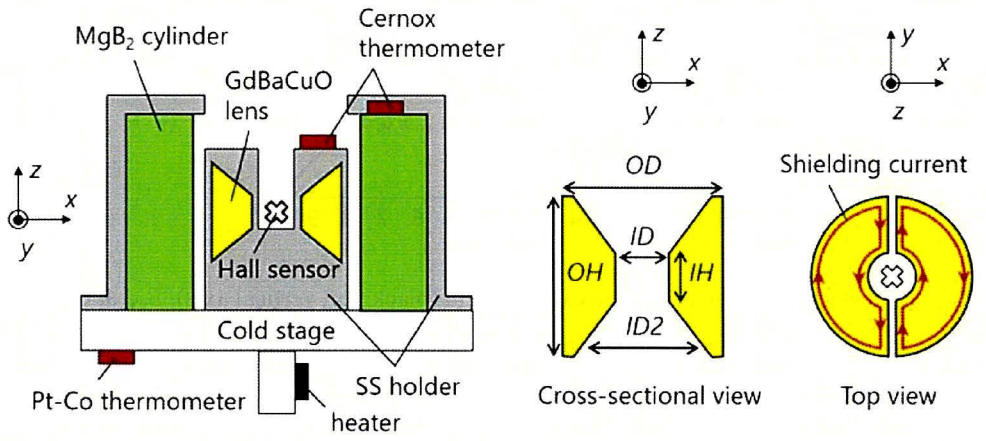


Figure 4-1. (a) Cross-sectional view of the schematic illustration of the experimental setup for the HTFML on the cold stage of a refrigerator. (b) Cross-sectional and top views of the GdBaCuO magnetic lens with slits. When a magnetic field is applied along the +$z$-axis direction to the GdBaCuO magnetic lens, the magnetic field penetrates from the slits and the shielding current flows as shown by the red arrows. As a result, the magnetic field increases along the +$z$-direction due to the shielding current.

### 4.2.2 Magnetization procedure

Figure 4-2 shows the time sequence of the external field (left vertical axis), $B_{ex}$, at the center of the HTFML and the operating temperature (right vertical axis), $T$, during the magnetizing process of the HTFML. The magnetizing external field, $B_{app}$, corresponds to the maximum value of $B_{ex}$. The HTFML device set in the vacuum chamber was inserted into a cryocooled 10 T superconducting solenoid magnet (JASTEC JMTD-10T100). First, the $MgB_2$ bulk cylinder and GdBaCuO bulk lens were cooled to $T$ = 40 K. In this stage, the $MgB_2$ cylinder is in the normal state and the GdBaCuO lens is in the superconducting state, where the time step ($TS$) is defined as $TS$ = 0. The proof-of-concept experiments of the HTFML were performed according to the following magnetizing process.

(1) The external magnetic field, $B_{ex}$, was ramped up linearly at +0.222 T min$^{-1}$ to $B_{app}$ = 1–3 T over five steps, where $TS$ of the ascending stage is defined as $TS$ = 1–5. This process corresponds to ZFC magnetization of the GdBaCuO lens, in which the magnetic field at the center is essentially higher than $B_{app}$ because of the shielding effect by the magnetic lens.

(2) The temperatures of both the $MgB_2$ cylinder and GdBaCuO lens were decreased to $T$ = 20 K under

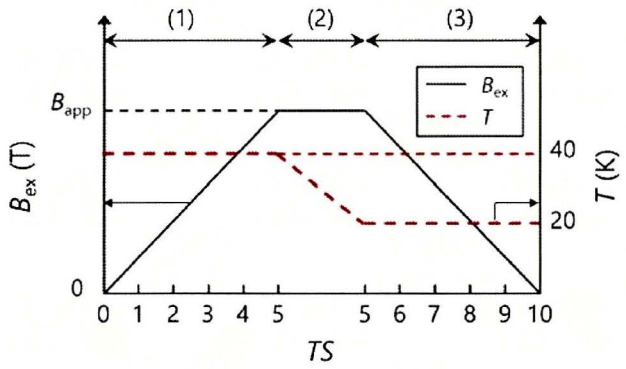


Figure 4-2. Time step ($TS$) sequence of the external field (black: left vertical axis), $B_{ex}$, at the center of the HTFML and the operating temperature (red: right vertical axis), $T$, during the magnetizing process to realize the HTFML. The magnetizing applied field, $B_{app}$, corresponds to the maximum value of $B_{ex}$.

the applied field $B_{app}$, with both materials now in the superconducting state.

(3) $B_{ex}$ was decreased linearly at −0.011 T min$^{-1}$ over five steps ($TS$ = 6–10) down to zero. During this process, the $MgB_2$ cylinder was magnetized by FCM and magnetic flux was trapped in the cylinder. A magnetic field at the center of the magnetic lens still remains due to the existence of the trapped field in the $MgB_2$ cylinder. As a result, the HTFML can reliably generate a magnetic field higher than the trapped field in the single $MgB_2$ TFM cylinder and $B_{app}$, even after $B_{ex}$ = 0 T.

Prior to the HTFML experiments, the trapped field properties of the $MgB_2$ cylinder and the magnetic concentration capability of the GdBaCuO lens were investigated independently using the same time sequence as shown in figure 4-2 under the external magnetic field of $B_{app}$ = 1–3 T, in which either the $MgB_2$ cylinder or GdBaCuO lens was set on the cold stage.

## 4.3 Results and discussion

### 4.3.1 Trapped field capability of the single $MgB_2$ cylinder

To confirm the trapped field capability of $MgB_2$ cylinder, the trapped field properties of the single $MgB_2$ cylinder was measured. Figure 4-3(a) shows the time evolution of the external field, $B_{ex}$, and trapped field, $B_c$, at the center of the single $MgB_2$ cylinder during the same time sequence shown in figure 2 under an external magnetic field of $B_{app}$ = 2.0 T. Figure 4-3(b) shows the time evolution of the temperatures of the cold stage and the $MgB_2$ cylinder for the same process. In the ascending stage, the magnetic field, $B_c$, increased linearly with increasing $B_{ex}$ and the magnitude of $B_c$ was the same as the external field ($B_c$ = $B_{ex}$ = 2.0 T) because the $MgB_2$ cylinder was in normal state ($T$ = 40 K). In the

descending stage, after cooling to 20 K, the $B_{ex}$ was slowly decreased at a constant rate of −0.011 T $min^{-1}$ and the FCM process was performed for the $MgB_2$ cylinder. As a result, a trapped field remained of $B_c$ = 2.0 T after $B_{ex}$ was decreased to zero due to the conventional vortex pinning effect. In figure 3(b), the temperature of the $MgB_2$ cylinder was nearly the same as that of the cold stage because of the good thermal contact.

Figure 4-4 shows the *TS* dependence of the trapped field, $B_c$, at the center of the single $MgB_2$ cylinder under external magnetic fields of $B_{app}$ = 1–3 T. In the ascending stage from *TS* = 0 to 5, the magnetic field increases linearly with increasing *TS* and the magnitude is the same as the external field because the $MgB_2$ cylinder is in normal state. In the descending stage of the FCM process, for the applied fields of $B_{app}$ = 1.0 and 2.0 T, trapped fields of 1.00 T and 1.98 T, respectively, were achieved at *TS* = 10 without flux creep. On the other hand, for higher applied fields of 2.5 and 3.0 T, the *TS* dependence of $B_c$ after *TS* = 5 gradually decreased and the final trapped field was 2.18 T, which suggests the maximum trapped field capability of the $MgB_2$ cylinder at *T* = 20 K. The trapped field cannot increase over 2.18 T, even if applied field is higher than 3.0 T. In the conceptual paper [1], $B_c$ = 2.85 T was predicted at the final step at *T* = 20 K in the bore of $MgB_2$ cylinder for $B_{app}$ = 3.09 T. The lower $B_c$ value in the present experiment results from the lower $J_c(B, T)$ of the present $MgB_2$ cylinder, compared with that used in the simulations in [1].

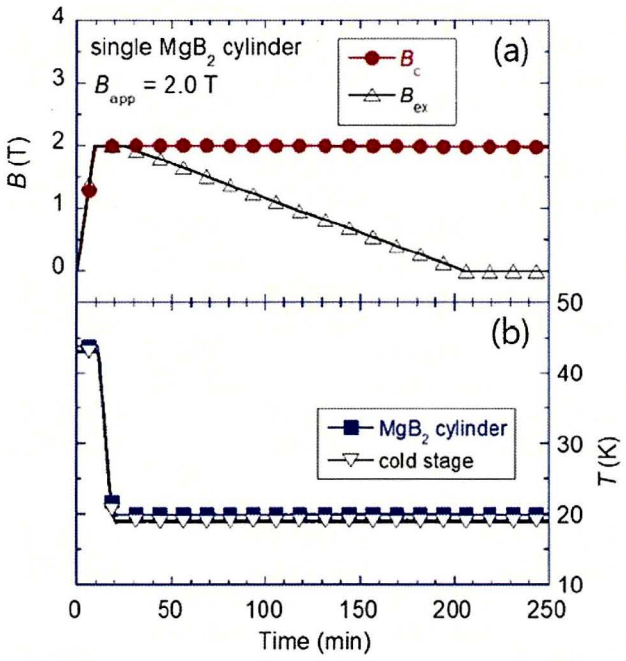


Figure 4-3. Time evolution of (a) the measured magnetic field, $B_c$, at the center of the single $MgB_2$ cylinder and external field, $B_{ex}$, and (b) the temperatures of $MgB_2$ cylinder and cold stage during the magnetization process for an applied field of $B_{app}$ = 2.0 T.

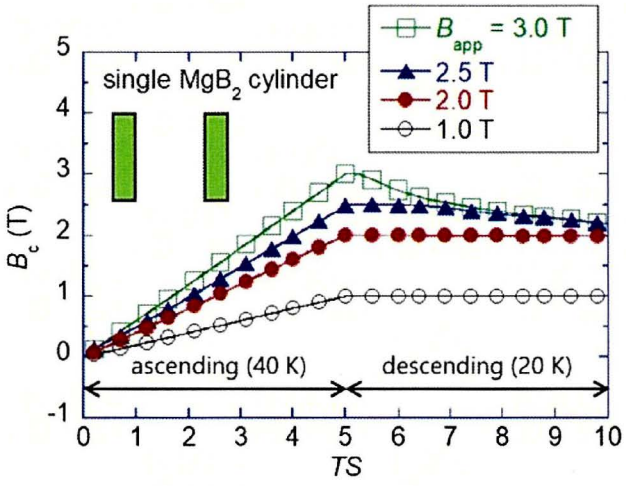


Figure 4-4. Time step (*TS*) dependence of the measured magnetic field, $B_c$, at the center of the single $MgB_2$ cylinder during the magnetization process for applied fields $B_{app}$ = 1.0–3.0 T.

### 4.3.2 Magnetic shielding capability of the single GdBaCuO bulk lens

The magnetic shielding capability of the GdBaCuO bulk lens was measured using the single GdBaCuO bulk lens during the ZFC process. Figure 4-5(a) shows the time evolution of the magnetic field, $B_c$, at the center of the single GdBaCuO bulk lens and the external field, $B_{ex}$, during the same time sequence shown in figure 4-2, under an external magnetic field of $B_{app}$ = 2.0 T. Figure 4-5(b) shows the time evolution of the temperatures of GdBaCuO bulk lens and the cold stage under the same process. In the ascending stage, a clear magnetic field concentration was observed; $B_c$ = 3.76 T was achieved, which resulted in a magnetic field concentration ratio of $B_c/B_{app}$ = 1.88. A temperature rises about 2.1 K took place during ascending stage from 0 to 10 min, originating from magnetic flux penetration into the magnetic lens. When the temperature of the cold stage was set to 20 K, the minimum temperature of the GdBaCuO bulk lens encapsulated by the SS holder was only 26.5 K, which may come from an imperfect thermal contact between the bulk lens and the SS holder. It should be noted that the final $B_c$ value was not zero, but a negative one of −0.48 T. This result suggests that some magnetic flux penetrated into the surface of the bulk lens and a residual magnetic field along the $-z$-direction existed due to the vortex pinning effect.

Figure 4-6 shows the *TS* dependence of the magnetic field, $B_c$, at the center of the single GdBaCuO bulk lens during the ZFC process under applied magnetic fields of $B_{app}$ = 1.0−3.0 T. In the ascending stage from *TS* = 0 to 5, the magnetic field was concentrated by the shielding current. For lower $B_{app}$ = 1 and 2 T, $B_c$ = 2.04 and 3.76 were achieved at *TS* = 5, which correspond to magnetic field concentration ratios, $B_c/B_{app}$, of 2.04 and 1.88, respectively. The $B_c$ values increased for higher $B_{app}$, which were 4.55 T and 5.19 T for $B_{app}$ = 2.5 and 3.0 T at *TS* = 5, respectively. However, the magnetic field concentration ratio, $B_c/B_{app}$, gradually decreased due to increased magnetic flux penetration into the bulk lens. For the final stage (*TS* = 10), at which the external field was zero, the $B_c$ value increased negatively with increasing $B_{app}$ for the same reason. For all the cases, the minimum temperature of the GdBaCuO bulk lens encapsulated by the SS holder was only 26.5 K. To improve the performance of the magnetic lens, lowering its temperature is necessary.

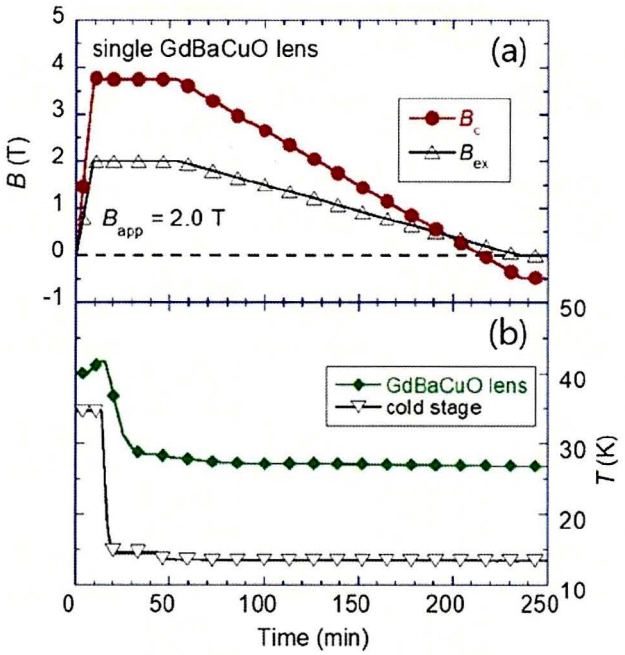


Figure 4-5. Time evolution of (a) the measured magnetic field, $B_c$, at the center of the single GdBaCuO bulk lens and external field, $B_{ex}$, and (b) the temperatures of GdBaCuO bulk lens and cold stage during the magnetization process for an applied field of $B_{app}$ = 2.0 T.

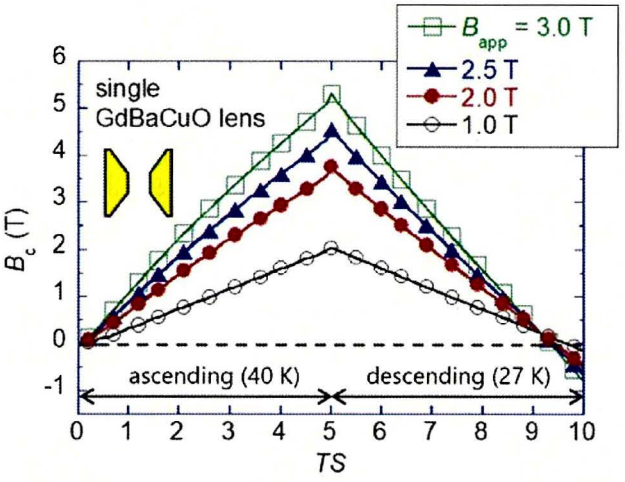


Figure 4-6. *TS* dependence of the measured magnetic field, $B_c$, at the center of the single GdBaCuO magnetic lens during the magnetization process under applied fields, $B_{app}$ = 1.0–3.0 T. For *TS* = 10, the $B_c$ value increased negatively with increasing $B_{app}$.

### 4.3.3 Realization of the HTFML

Finally, the experimental realization of the HTFML using GdBaCuO magnetic lens, combined with the $MgB_2$ bulk cylinder, is present. Figure 4-7(a) shows the time evolution of the magnetic field, $B_c$, at the center of the HTFML during the magnetizing process shown in figure 2 under an external magnetic field of $B_{app}$ = 2.0 T. Figure 4-7(b) shows the time evolution of the temperatures measured at each position. In the ascending stage, the $B_c$ value reached 3.65 T and then slightly decreased to 3.55 T at the end of the descending stage due to flux flow. The magnetic field concentration ratio, $B_c/B_{app}$, was 1.76 at the end of the ramp. The temperatures of the $MgB_2$ cylinder and the GdBaCuO bulk lens on the SS holder were 20.0 and 26.5 K, respectively. These results demonstrate the HTFML effect experimentally for the first time.

Figure 4-8 shows the *TS* dependence of the magnetic field, $B_c$, at the center of the HTFML during the magnetizing process under applied fields of $B_{app}$ = 1.0–3.0 T. At the end of the ascending stage (*TS* = 5), the $B_c$ value for each $B_{app}$ was nearly the same as that for the single GdBaCuO magnetic lens case, as shown in figure 6. In the descending stage, for $B_{app}$ = 1.0 and 2.0 T, the $B_c$ value was nearly the same as that at *TS* = 5. On the other hand, for $B_{app}$ = 2.5 and 3.0 T, the $B_c$ value gradually decreases with increasing *TS*. As a result, the final $B_c$ value for $B_{app}$ = 2.5 and 3.0 T was smaller than that for $B_{app}$ = 2.0 T. The concentrated magnetic field, $B_c$, at *TS* = 5 and 10 at the center of the HTFML, and calculated magnetic field concentration ratio, $B_c/B_{app}$, for the various applied magnetic fields, $B_{app}$, are summarized in table 4-1. A maximum $B_c$ value of 3.55 T was achieved for $B_{app}$ = 2.0 T.

In the concept paper, in which the HTFML was proposed to be constructed using a REBaCuO magnetic lens and $MgB_2$ TFM cylinder, a concentrated magnetic field $B_c$ = 4.73 T was predicted for an external magnetizing field $B_{app}$ = 3 T using numerical simulations [1]. However, the maximum $B_c$ value was as low as 3.55 T experimentally under the same magnetizing process for $B_{app}$ = 2.0 T. This difference occurs for the following reasons. Firstly, the assumed $J_c$ ($B$, $T$) characteristics of the $MgB_2$ and GdBaCuO bulks used in the simulations were higher than those of the actual bulks used in the experiments. Secondly, the minimum temperature of the GdBaCuO bulk lens was only 26.5 K, when the temperature of the cold stage was set to 20.0 K. To enhance the HTFML effect for the present $MgB_2$ cylinder and GdBaCuO bulk lens, the thermal contact between the GdBaCuO bulk lens and the SS holder must be improved. Nevertheless, author's group have realized the HTFML effect experimentally for the first time. Our final goal is to build and test an HTFML using a GdBaCuO cylinder and GdBaCuO lens, for which a $B_c$ value in excess of 10 T (*e.g.*, $B_c$ = 13.5 T [1]) is predicted for a magnetizing process with $B_{app}$ = 10 T. A cryocooled 10 T superconducting solenoid magnet with a large room temperature bore (*e.g.*, 100 mm in ID) has become more readily available in the science and engineering research communities outside of the field of superconductivity. Thus, building on these findings, we aim to provide easily a concentrated magnetic field higher than 10 T in an open

space using this HTFML system.

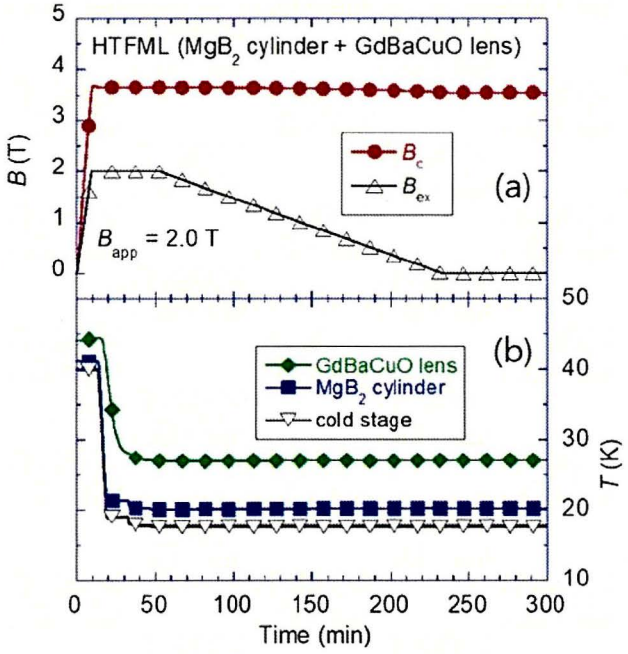


Figure 4-7. Time evolution of (a) the measured magnetic field, $B_c$, at the center of the HTFML and external field, $B_{ex}$, and (b) the temperatures for each measurement point during the magnetizing process for $B_{app}$ = 2.0 T.

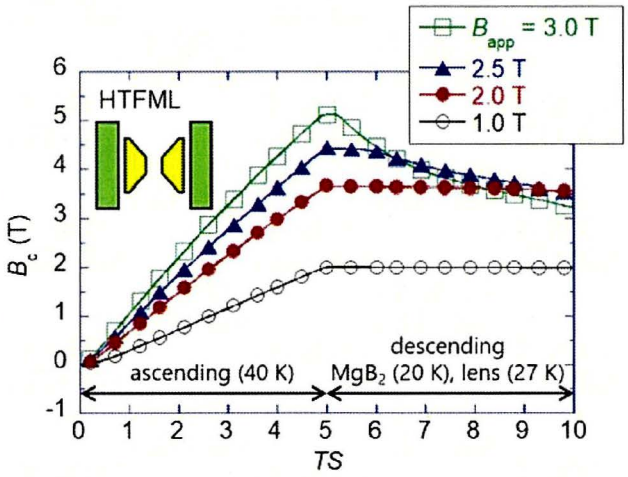


Figure 4-8. *TS* dependence of the measured magnetic field, $B_c$, at the center of the HTFML device during the magnetization process under various applied fields, $B_{app}$ = 1.0–3.0 T

## 4.4 Summary of Chapter 4

We have presented, for the first time, the experimental realization of a HTFML, based on the device design and magnetizing procedure recently proposed. The important results and conclusions in this study are summarized as follows.

(1) The HTFML effect was demonstrated experimentally using GdBaCuO magnetic lens and $MgB_2$ TFM cylinder for the first time, such that a magnetic field can be generated in the central bore of the magnetic lens that is higher than both the trapped field in the single cylindrical bulk TFM and the external magnetizing field, even after the externally applied field decreases to zero.

(2) A maximum concentrated magnetic field of $B_c$ = 3.55 T was achieved in the central bore of the HTFML device after removing an applied field of $B_{app}$ = 2.0 T at T = 20 K. The maximum $B_c$ value was smaller than the one estimated by numerical simulations, which results from the lower $J_c$ ($B$, $T$) and higher operating temperature, compared with those of the numerical predictions.

(3) For higher $B_{app}$, the $B_c$ value was not enhanced because of a weakened lens effect due to magnetic flux penetration into the bulk GdBaCuO material comprising the lens. To enhance the HTFML effect, improving the thermal contact between the HTFML and the cold stage and lowering temperature of the GdBaCuO lens and $MgB_2$ TFM cylinder is necessary for the present setup.

## 4.5 References


[1] Takahashi K, Fujishiro H and Ainslie M D 2018 A new concept of a hybrid trapped field magnet lens *Supercond. Sci. Technol.* 31 044005

[2] Giunchi G, Raineri S, Wesche R and Bruzzone P L 2004 The voltage–current relations for $MgB_2$ obtained by reactive liquid infiltration *Physica C* 401 310–5

[3] Giunchi G, Ripamonti G, Cavallin T and Bassani E 2016 The reactive liquid Mg infiltration process to produce large superconducting bulk $MgB_2$ manufacts *Cryogenics* 46 237–42

[4] Morita M, Sawamura M, Takebayashi S, Kimura K, Teshima H, Tanaka M, Miyamoto K and Hashimoto M 1994 Processing and properties of QMG materials *Physica C* 235–240 209–12

[5] Nariki S, Teshima H and Morita M 2016 Performance and applications of quench melt-growth bulk magnets *Supercond. Sci. Technol.* 29 034002

[6] Namba S *et al.* 2019 *IEEE Trans. Appl. Supercond.* 29 6801605

[7] Fujishiro H, Takahashi K, Naito T, Yanagi Y, Itoh Y and Nakamura T 2018 New proposal of mechanical reinforcement structures to annular REBaCuO bulk magnet for compact and cryogen-free NMR spectrometer *Physica C* 550 52–6

[8] Fujishiro H, Naito T, Yanagi Y, Itoh Y and Nakamura T 2019 Promising effects of a new hat structure and double metal ring for mechanical reinforcement of a REBaCuO ring-shaped bulk

during field-cooled magnetisation at 10 T without fracture *Supercond. Sci. Technol.* 32 065001

# Chapter 5

# Experimental realization of a 10 T-class, all-(RE)BaCuO hybrid trapped field magnet lens

# 5.1 Preface of Chapter 5

In the concept paper, a higher trapped field of $B_c$ = 13.49 T was predicted at 20 K for the applied field of $B_{app}$ = 10 T using inner (RE)BaCuO lens and the outer (RE)BaCuO TFM cylinder. In this case, a special technique must be used to control the temperature of each bulk part individually, such as the use of two cryocoolers, a thermal (heater) method or a mechanical switch [1]. Hence, the magnetizing sequence of the HTFML includes two magnetizing methods: ZFCM for the inner magnetic lens and FCM for the outer TFM cylinder.

As a first step, author's group have realized the HTFML based on the same (RE)BaCuO bulk material for both parts using liquid nitrogen, in which the inner magnetic lens and outer TFM cylinder were housed in separate containers with liquid nitrogen poured into each container sequentially according to the corresponding magnetizing sequence. As a result, $B_c$ = 1.83 T was obtained at 77 K after magnetization with $B_{app}$ = 1.80 T [2]. However, to best exploit the trapped field capability of the outer (RE)BaCuO cylinder and realize a higher $B_c$ over 10 T, the all-(RE)BaCuO HTFML should be cooled to a lower temperature below 50 K and magnetized, where the $J_c(B, T)$ characteristics have a higher value under higher magnetic fields. Furthermore, if the HTFML device can be realized using one cold stage of a cryocooler, the whole system would be more cost-effective, and provide both a higher magnetic field and magnetic field gradient in an open bore space outside the vacuum chamber [3].

In the present chapter, the author has verified experimentally a 10 T-class, all-(RE)BaCuO HTFML magnetized under 50 K using only one cryocooler by a special technique, in which only the inner magnetic lens was tightly connected to the cold stage and cooled at all times, and the outer TFM cylinder was loosely connected to the cold stage before the magnetizing process by introducing a gap between the outer TFM cylinder and cold stage. During the cooling process before magnetization, the outer TFM cylinder then cooled much slower than the inner magnetic lens. As a result, the non-superconducting (normal) state for the outer TFM cylinder and the superconducting state for the inner magnetic lens can be simultaneously realized. A maximum concentrated field of $B_c$ = 9.8 T was achieved for the magnetizing process from $B_{app}$ = 7 T in the present HTFML, consistent with the numerical estimation in our previous conceptual study [4]. The concentrated field values are compared for other HTFML devices reported. These results validate the HTFML as a compact and desktop-type magnet device that can provide 10 T-class magnetic field enhancement from the viewpoint of the magnetizing method.

## 5.2 Experimental setup and magnetizing sequence

Figure 5-1(a) presents the experimental setup of the HTFML, in which the inner magnetic lens and the outer TFM cylinder are encapsulated in a stainless steel (SS) holder for mechanical reinforcement. Side and top views of the actual setup are also presented in the photographs. Figures 5-1(b) and 5-1(c), respectively, show the side and top views of each bulk component of the outer TFM cylinder and the inner magnetic lens. All of the bulks were fabricated by the QMG™ method (Nippon Steel Corporation, Japan) [5]. The outer TFM cylinder was constructed using three stacked EuBaCuO ring bulks (top bulk, middle bulk and bottom bulk). The dimensions of the EuBaCuO cylinder are a 60 mm outer diameter (OD), 36 mm inner diameter (ID) and 54 mm height (H). Each of the EuBaCuO ring bulks was reinforced by an Al alloy ring 5 mm in thickness (OD = 70 mm, ID = 60 mm) adhered by a thin layer of epoxy resin. These bulks were also encapsulated in the SS holder with a "hat structure" 5 mm in thickness for mechanical reinforcement against the Lorentz force generated during magnetization. Such mechanical reinforcement is necessary to avoid fracture of the bulks, particularly for applied fields as high as 10 T. The effect of the "hat structure" of the outer SS holder on the mechanical reinforcement was investigated by numerical simulation, which can provide a compressive stress around 100 MPa from the cooling process due to the difference in the thermal expansion coefficient between the bulk material and SS holder [6]. The effect was experimentally confirmed to avoid fracture of a ring bulk for FCM from $B_{app}$ = 10 T in [7].

As shown in figure 5-1(c), the inner magnetic lens (OD = 36 mm, ID = 10 mm, ID2 = 26 mm, IH = 8 mm, OH = 30 mm) was constructed using two pieces of conical-shaped GdBaCuO bulks, in which a slit with 200 $\mu$m width is inserted in the diagonal direction so that the magnetic flux can be concentrated into the central bore through the slit. The TFM cylinder and magnetic lens are the same used in the previous experiment at 77 K [2]. Note that only the inner lens component, including the SS holder and a copper spacer, was tightly connected to the cold stage through a thin indium sheet. The temperature of the TFM cylinder, magnetic lens and the cold stage of the GM-cycle helium cryocooler was monitored by two Cernox™ thermometers and a Pt-Co thermometer, as shown in figure 5-1(a). The whole device was enclosed in a vacuum chamber. A cryocooled 10 T superconducting magnet (JASTEC, JMTD-10T100) was utilized to ramp up/down the external magnetizing field. The concentrated field was monitored at the center of the lens by an axial-type Hall sensor (F.W. Bell, BHA921), and the external magnetic field was calculated by measuring the electric current through a shunt resistor.

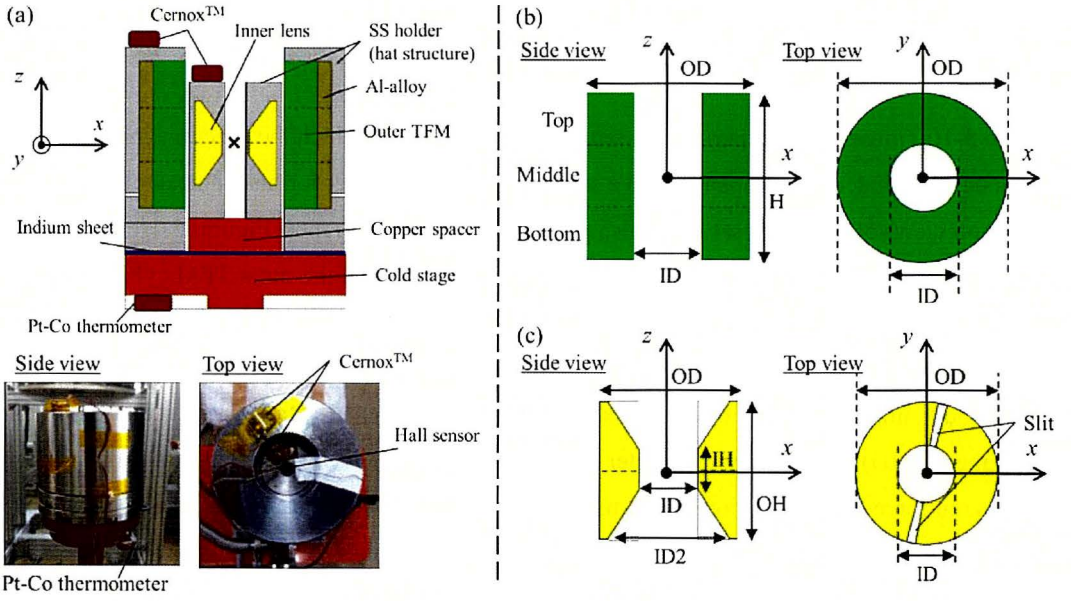


Figure 5-1. (a) Experimental setup of the HTFML, in which the inner magnetic lens and outer TFM cylinder, both made from (RE)BaCuO, are encapsulated in a stainless steel (SS) holder for mechanical reinforcement. The side and top views of the actual setup are also presented in the photographs. Schematic views of (b) the outer TFM cylinder and (c) the inner magnetic lens.

Figure 5-2 shows the time sequence of the temperature for both bulk parts – the inner magnetic lens, $T_L$, and the outer TFM cylinder, $T_T$ – and the external field, $B_{ex}$, and the concentrated magnetic field, $B_c$, at the center of the HTFML, which has been revised for these experiments in comparison to the original conceptual study [4]. To control the temperature of the outer TFM cylinder quasi-independently using one cold stage of the cryocooler, a special technique named the "loose contact method" has been designed. Figure 5-3 shows the conceptual view of the "loose contact method", exploiting two kinds of experimental configurations of the HTFML in the vacuum chamber, aligned in (a) the horizontal direction during the cooling process and (b) the vertical direction during magnetizing process. In the initial preparation of the experimental setup of the HTFML on the cold stage, the outer TFM cylinder was loosely connected to the cold stage by screws and then set in the vacuum chamber. During the cooling stage of (1) in figure 5-2, the cooling process was started, and several hours later, the whole HTFML device was tilted 90 degrees along the horizontal direction using a hand-held rod attached to the bottom of the apparatus. In this stage, as shown in figure 5-3(a), a non-uniform gap, *i.e.*, 0~1 mm, exists at the interface between the TFM cylinder and the cold stage due to gravity. This technique worked sufficiently and the cooling speed of the TFM cylinder was delayed in comparison to that of the magnetic lens. Before proceeding to the magnetization in the ascending stage of (2) in figure 5-2, the whole HTFML device was aligned vertically, where the gap between the TFM cylinder and the cold stage would be $\cong$ 0 mm and the TFM cylinder would contact loosely with the

cold stage by its own weight, as shown in figure 5-3(b). At stage (2), the inner magnetic lens is in the superconducting state ($T_L < T_c$) and ZFCM is performed, but the outer TFM cylinder must be in the normal state ($T_T > T_c$). As mentioned before, the inner lens component was tightly connected to the cold stage and the temperature can be precisely controlled. In the magnetizing process, the whole HTFML device in the vacuum chamber was lifted up and inserted into the bore of the superconducting magnet as shown in figure 5-3(c).

In figure 5-2, the magnetizing applied field, $B_{app}$, corresponds to the maximum value of $B_{ex}$. The magnetizing sequence was constructed from the following process from (1) to (5), which is special for the HTFML exploiting the gap for the outer TFM cylinder.

(1). During the cooling process, where the whole HTFML device is aligned in the horizontal direction: the temperature of the inner magnet lens, $T_L$, (as well as that of the cold stage, $T_s$) is lowered from 300 K to the lowest temperature as possible (roughly, a minimum of $T_L \cong 20$ K in the present experiment). At the end of this stage, the inner magnet lens is in the superconducting state, but the outer TFM cylinder is in the normal state ($> T_c$) due to its delayed cooling speed.

(2). Ascending stage of the magnetizing process (while the cooling process proceeds), where the whole HTFML device is stood upright and aligned in the vertical direction, and then inserted in the superconducting magnet: the external magnetic field, $B_{ex}$, is ramped up linearly to $B_{app}$ at a certain rate (+0.1 T/min. in the present experiment), which corresponds to the ascending stage of ZFCM for the inner magnetic lens. The magnetic field is concentrated in the bore of the magnetic lens, which would be higher than $B_{app}$ because of the shielding effect by the magnetic lens. The temperature of the outer TFM cylinder should be kept over $T_c$ until $B_{app}$ completely penetrates the outer TFM cylinder. It is desirable that the difference in temperature between the outer TFM cylinder, $T_T$, and $T_L$, $\Delta T$ ($= T_T - T_L$), be over 50 ~ 100 K just before magnetization, which enables the separation of the magnetization processes of ZFCM for the magnetic lens and FCM for the TFM cylinder in the later stage.

(3). Cooling process in a static magnetic field: $T_T$ is then decreased gradually to the lowest $T_T \cong$ 50 K, below $T_c$ but higher than $T_L$, due to the imperfect thermal contact to the cold stage through the gap $\cong$ 0 mm. The $B_c$ value can be maintained reliably if $T_L$ is kept at 20 K.

(4). Descending stage of the magnetizing process at the lowest temperature: $B_{ex}$ is decreased linearly down to zero at a certain rate (-0.1 T/min., or -0.002 T/min. for higher $B_{app}$ over 7 T, in the present study). During this process, the outer TFM cylinder is magnetized by FCM and a magnetic field is trapped inside the TFM cylinder within its trapped field capability based on its $J_c(B, T)$ characteristics (if this can be done successfully without the occurrence of large flux jumps caused by the resultant heat generation and/or mechanical fracture of the bulk material).

(5). As a result, the HTFML can reliably generate $B_c$ higher than the trapped field of the single

cylindrical TFM, as well as $B_{app}$, even after $B_{ex} = 0$.

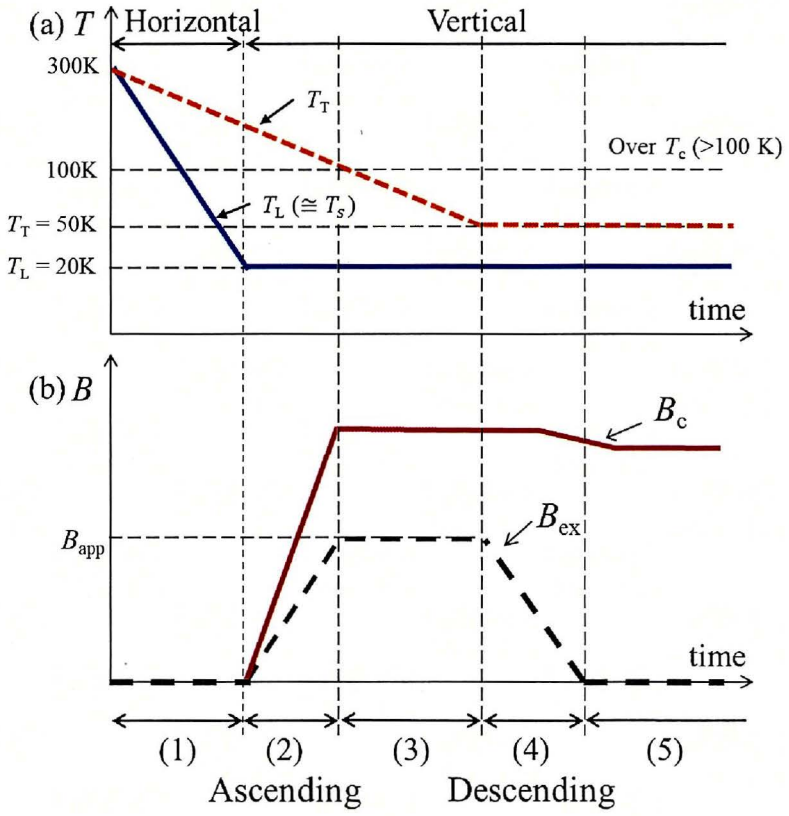


Figure 5-2. Time sequence of (a) the temperature $T$ (the outer TFM cylinder, $T_T$, and the inner magnetic lens, $T_L$) and (b) the magnetic field $B$ (external field, $B_{ex}$, and concentrated magnetic field, $B_c$ at the center of the present HTFML using all-(RE)BaCuO bulks) during the magnetizing process divided into steps from (1) to (5). The magnetizing applied field, $B_{app}$, corresponds to the maximum value of $B_{ex}$.

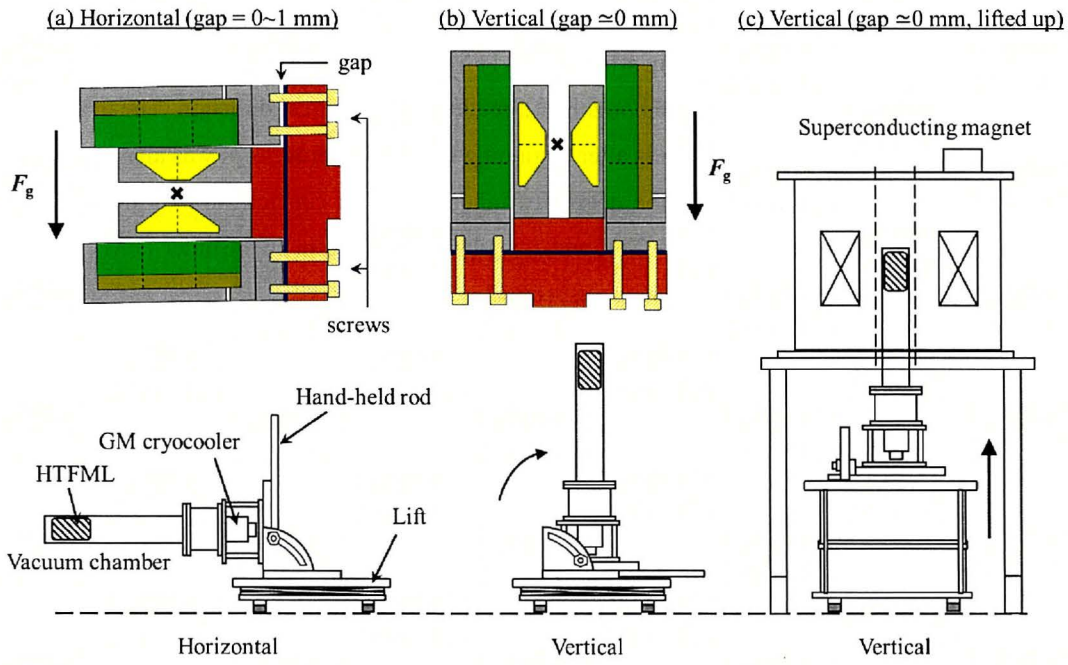


Figure 5-3. Conceptual view of the "loose contact method", exploiting two kinds of experimental configurations of the HTFML in the vacuum chamber, aligned in (a) the horizontal direction during the cooling process and (b) the vertical direction during magnetizing process. (c) The whole HTFML device in the vacuum chamber lifted up and inserted into the bore of the superconducting magnet in the magnetizing process.

Figure 5-4 shows the typical experimental results for the cooling process of the present HTFML exploiting the "loose contact method", in which the HTFML device set in the vacuum chamber was reclined up after $t$ = +11 hours, from the horizontal direction to the vertical direction. The maximum $\Delta T \cong$ 100 K was obtained at $t$ = +8 hours after beginning the cooling process. It was also confirmed that $\Delta T$ would change depending on the degree of inhomogeneous contact through the gap. The lowest temperatures were $T_T$ = 54 K, $T_L$ = 24 K and $T_s$ = 14 K for each point on the outer TFM cylinder, inner magnetic lens and under the cold stage, respectively.

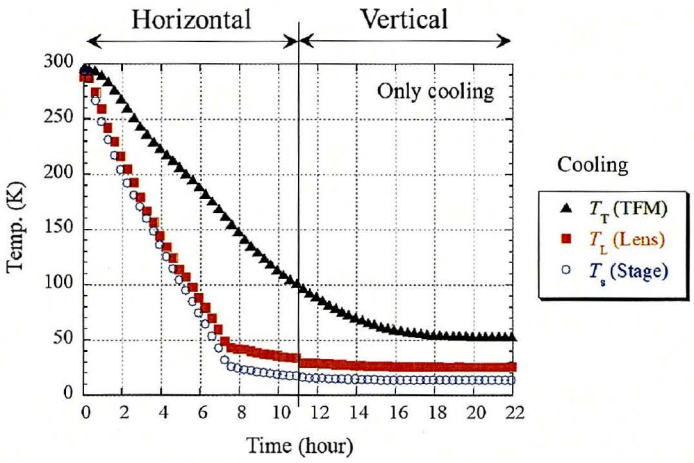


Figure 5-4. Typical experimental results of cooling process of the present HTFML exploiting the "loose contact method", in which the HTFML device set in the vacuum chamber was reclined up at $t$ = +11 hours from the horizontal direction to the vertical direction.

## 5.3 Experimental results

Figure 5-5 shows the time dependence of the temperatures measured at each position – the inner magnetic lens, $T_L$, the outer TFM cylinder, $T_T$, and the cold stage, $T_s$ – and the concentrated field, $B_c$, and the external field, $B_{ex}$, during magnetization with several applied fields, $B_{app}$, of (a) 3 T, (b) 5 T and (c) 7 T, respectively. The lowest value of $T_L$ and $T_T$ for magnetization process is included in the bottom panel of each figure. In the case of $B_{app}$ = 3 T, as shown in figure 5-5(a), the $B_{ex}$ value was ramped up at $t$ = +8.5 hours, when the maximum temperature difference $\Delta T \geq 100$ K was obtained reliably after cooling to $T_L$ = 40 K and $T_T$ = 150 K. The lowest temperatures were, respectively, $T_L$ = 24 K for ZFCM and $T_L$ = 57 K for FCM. Resultantly, $B_c$ = 5.5 T was achieved with little flux creep caused by the non-linear electrical property of the bulk material, even well after FCM process at $t$ = +24 hours. Compared with the higher $B_{app}$ cases of 5 T and 7 T, as shown in figures 5-5(b) and 5-5(c), it was confirmed that the $\Delta T$ value changed in the range of 50 ~100 K, and the lowest temperatures of $T_L$ and $T_T$ were not consistent because the non-uniform thermal contact through the gap is not controllable precisely in the present system. Higher $B_c$ values of 7.9 T and 9.8 T were achieved for $B_{app}$ = 5 T and 7 T, respectively. These experimental results successfully verified the numerical estimations for the 10 T-class HTFML, up to $B_{app}$ = 7 T, for the first time [4]. These values will be compared with conventional HTFMLs at the end of this section. It should be noted that the experimental $T_T$ value was not constant and gradually increased due to the heat generation caused by the movement of magnetic flux during FCM of the outer TFM cylinder, which was remarkably large for higher $B_{app}$. This thermal instability might come from the possibility of larger heat generation in the stacked TFM cylinder, as well as the slower cooling speed and efficiency of the loose contact method in the present setup.

Figures 5-6(a) and 5-6(b), respectively, show similar results of the time dependence of the temperature and magnetic field during magnetization with an applied field of $B_{app}$ = 10 T. During the ZFCM process until $t$ = +14 hours, $B_c$ = 13.9 T was generated at the center of the HTFML device with a background field of $B_{ex}$ = 10 T, which means that the maximum of $B_c$ might be over 13 T, if the outer TFM cylinder could replace external magnetizing magnet after the FCM process. Unfortunately, during the descending stage of the FCM process, the $T_T$ value increased and stayed as high as 68 K, and then the $B_c$ value suddenly dropped at $B_{ex}$ = 5 T due to the occurrence of a large flux jump at $t$ = +18 hours, at which the temperatures also abruptly increased to above $T_c$. After that, the $B_c$ gradually decreased with decreasing $B_{ex}$ and the final $B_c$ value became negative. Such a negative $B_c$ value is typically obtained in the case for the single magnetic lens, in which the magnetic flux is trapped in a part of magnetic lens after completing the conventional ZFCM process. These results indicate that the thermal instability of the outer TFM cylinder could result in a flux jump during FCM and/or the

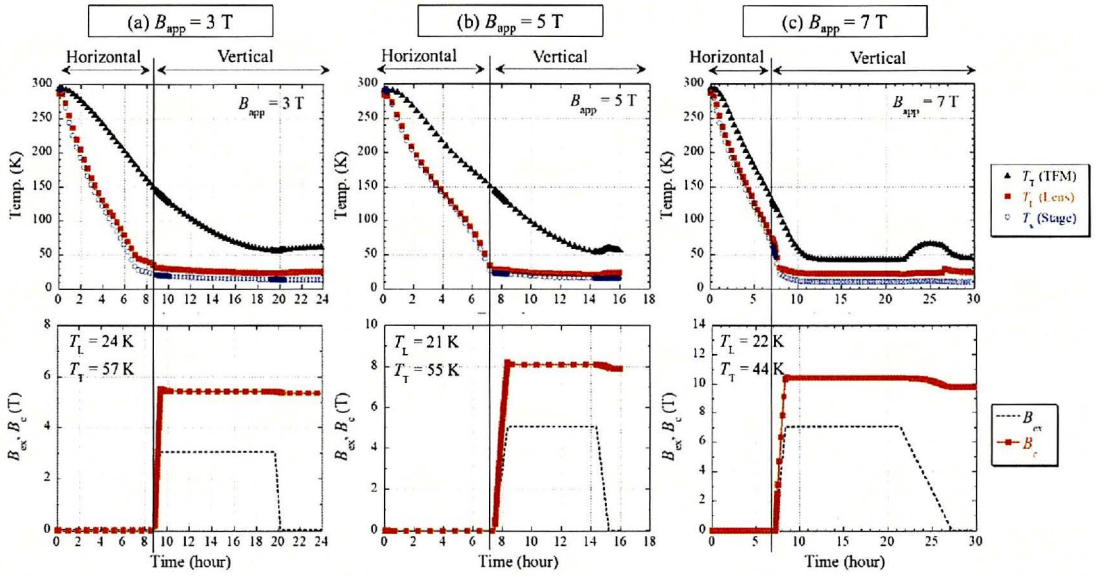


Figure 5-5. Time dependence of the temperatures measured at each position – the outer TFM cylinder, $T_T$, the inner magnetic lens, $T_L$, and the cold stage, $T_s$ – and the concentrated field, $B_c$, and the external field, $B_{ex}$, during magnetization with several applied fields, $B_{app}$, of (a) 3 T, (b) 5 T and (c) 7 T, respectively.

mechanical fracture of the bulk material. To realize a $B_c$ value over 10 T, further investigations are required relating to the following issues: thermal stability of the large, stacked TFM cylinder, and development of a more practical cooling method that can achieve a stable and controllable cooling process for each part of HTFML.

Figure 5-7 summarizes the magnetization curves of the HTFML magnetized from $B_{app}$ = 3, 5, 7 and 10 T, which can compare the difference of the lens effect during the ascending stage, and the flux creep and the final $B_c$ value in the descending stage. In the ascending stage, for every $B_{app}$ value, the $B_c$-$B_{ex}$ relation shows an identical trend, which indicates the good reliability of the shielding effect by the magnetic lens. However, in the descending stage for $B_{app}$ values of 7 T and 10 T, the flux creep seems clearly due to the large temperature rise during FCM (up to 68 K) in the stacked TFM cylinder. In the case of $B_{app}$ = 10 T, a flux jump occurred during the descending stage that may be of mechanical or thermal nature, which will be discussed later. If this flux jump did not occur under a constant and stable temperature during magnetization from $B_{app}$ = 10 T, it is expected that $B_c$ = 13 T would be achieved.

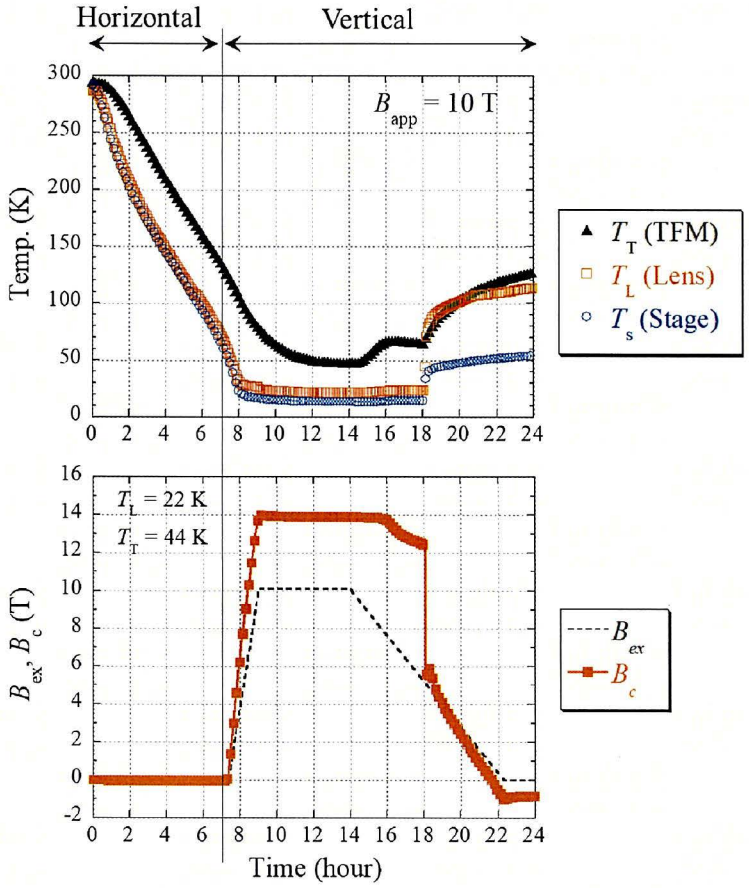


Figure 5-6. Time dependence of the temperatures measured at each position – the outer TFM cylinder, $T_T$, the inner magnetic lens, $T_L$, and the cold stage, $T_s$ – and the concentrated field, $B_c$, and the external field, $B_{ex}$, during magnetization with an applied field, $B_{app}$ = 10 T.

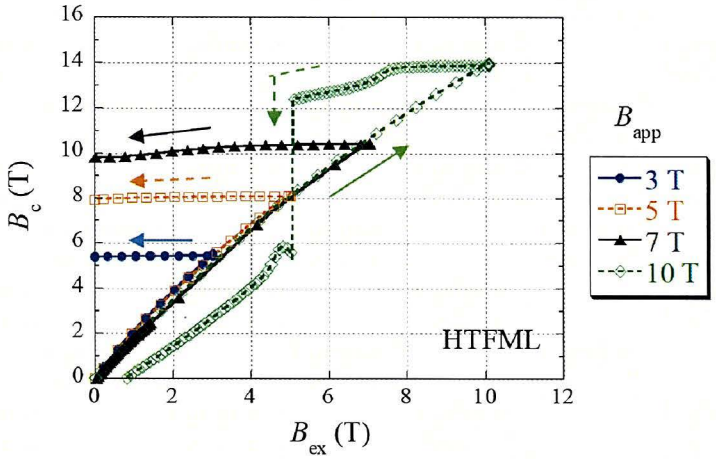


Figure 5-7. Magnetization curves of the HTFML magnetized with applied fields, $B_{app}$ = 3, 5, 7 and 10 T. The lens effect during the ascending stage, and the flux creep and the final trapped field in the descending stage are compared.

To find out whether mechanical fracture occurred after the magnetization of the HTFML from $B_{app}$ = 10 T, the inner magnetic lens and outer TFM cylinder were magnetized separately again. Figure 5-8 shows the magnetization curve of the magnetic lens by itself during the ascending stage of ZFCM with $B_{app}$ = 3 T and $T_L$ = 30 K, after the occurrence of the flux jump during the magnetization of the HTFML from $B_{app}$ = 10 T (labelled "After"). A similar result before the flux jump is shown for comparison (labelled "Before"; see figure 5-5(a)). The measured $B_c$ was enhanced (with respect to $B_{ex}$) by the magnetic lens and increased in proportional to $B_{ex}$, consistent with the "Before" results. This result clearly shows that there was no fracture in the inner magnetic lens after the flux jump.

Figure 5-9 shows the trapped field profiles for the (a) top surfaces and (b) bottom surfaces of each TFM ring bulk (top bulk, middle bulk, and bottom bulk), magnetized by FCM from $B_{app}$ = 1 T in liquid nitrogen after the flux jump, in which the trapped field value was measured 3 mm above the surfaces of each ring bulk. Photographs of each bulk were also taken after the measurement. The fracture point can be seen in the top surface view of the bottom bulk, in which the crack penetrates along the 10 o'clock direction as depicted. In addition, it was confirmed that there is an identical trace of burning at the interface between the top surface of the bottom bulk and the bottom surface of the middle bulk, as marked in each picture. The degree of fracture behavior was determined from the results of the trapped field profile into three-levels: not broken (top bulk), partially broken (middle bulk), and completely broken (bottom bulk), respectively. The bottom bulk, in which the crack destroyed the circumferential current, showed the so-called "C-shaped" magnetic field profile on both surfaces of the bulk and there is no longer the remnant trapped field inside the central region, *i.e.*, $B_T$ = 0 T. In contrast, only the top bulk showed a comparative, uniform field profile with a peak value of $B_T$ = $\pm$0.32 T at the center of both surfaces. This profile might deserve to be described as "not broken". In the middle bulk, evaluated as "partially broken", the bulk showed an inhomogeneous trapped field profile that is not identical for each surface, and the trapped magnetic field is as small as $B_T$ = $\pm$0.02 T at the center. These results offer evidence that the thermal instability of the stacked TFM cylinder caused a flux jump during the FCM process, which resulted in the mechanical fracture of multiple bulks at the same time, even though the mechanical reinforcement using the SS support with the "hat structure" was applied. It is therefore recommended that the stacked bulk cylinder should be kept at a constant temperature with adequate cooling to avoid flux jumps when it is magnetized with higher $B_{app} \cong$ 10 T. In this sense, fundamental studies related to the suppression of the thermal instability of the HTFML should be performed in more detail.

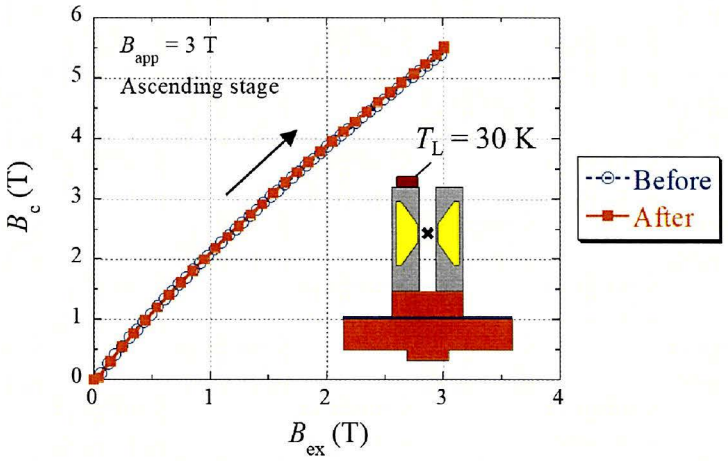


Figure 5-8. Magnetization curve of the single magnetic lens during the ascending stage of ZFCM with the applied field of $B_{app}$ = 3 T, after the happening of the flux jump during the magnetization of the HTFML from $B_{app}$ = 10 T, labelled as "After". The result before the flux jump is referred as "Before" from figure 5-5(a).

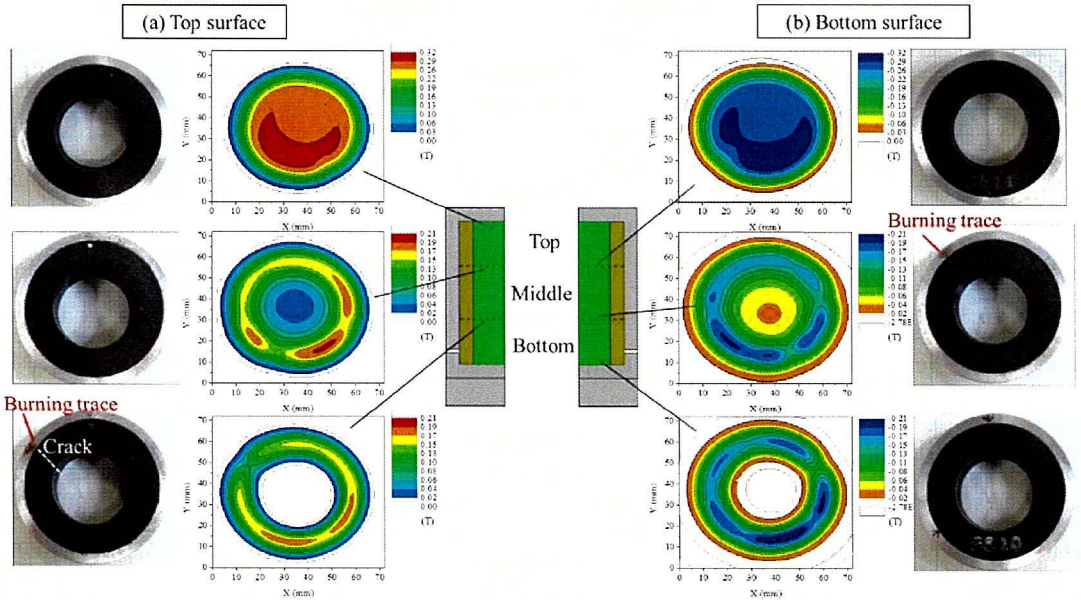


Figure 5-9. Trapped field profiles for (a) the top and (b) the bottom surface of each TFM ring bulk (top bulk, middle bulk, and bottom bulk), magnetized by FCM with the applied field of $B_{app}$ = 1 T in liquid nitrogen after the happening of the flux jump. The trapped field value was measured 3 mm above the surfaces. Photographs of each bulk were also taken after the measurement.

Finally, figure 5-10 summarizes the concentrated field, $B_c$, at the center of the HTFML, as a function of $B_{app}$, compared with previously reported experimental results [2, 8]. Since 2018, the feasibility of the HTFML has been proved particularly for lower $B_{app}$ up to 3 T for two cases: (1) exploiting an

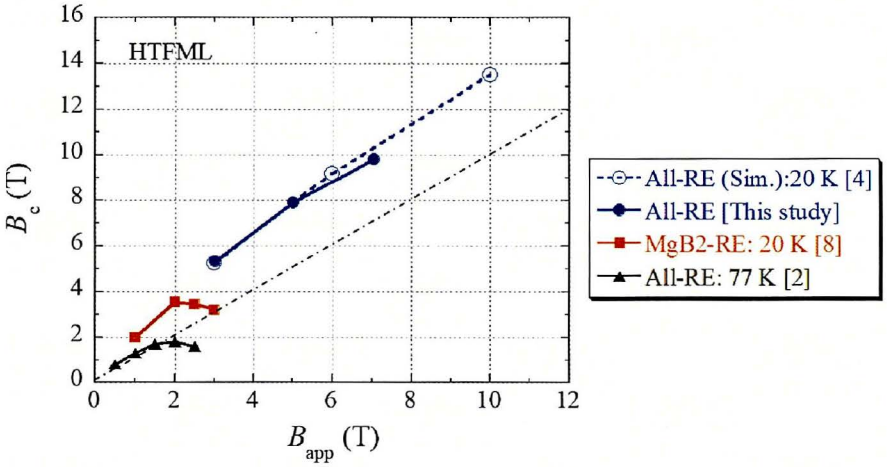


Figure 5-10. The concentrated field, $B_c$, at the center of the HTFML (labelled "All-RE [This study]"), as a function of $B_{app}$, compared with previously reported experimental results. In the previous experiments, the HTFMLs were constructed with the combination of an outer $MgB_2$ TFM cylinder and inner GdBaCuO magnetic lens (labelled "$MgB_2$-RE: 20 K") [8], as well as an all-(RE)BaCuO design at 77 K (labelled "All-RE: 77 K") [2]. The numerical estimations for the HTFML with all-(RE)BaCuO bulks are also included (labelled "All-RE (Sim.): 20 K") [4].

inner GdBaCuO bulk lens and outer $MgB_2$ TFM cylinder, in which a maximum concentrated field of $B_c$ = 3.55 T was achieved for $B_{app}$ = 2 T at 20 K, and (2) replacing the outer $MgB_2$ cylinder with an EuBaCuO one, in which $B_c$ = 1.83 T was achieved for $B_{app}$ = 1.80 T at 77 K. However, these configurations are not appropriate for magnetization with higher $B_{app}$ over 3 T, because of (1) the inferior $J_c(B, T)$ characteristics of the $MgB_2$ bulk and (2) the operating temperature of 77 K. An original concept of the HTFML that could generate over $B_c$ = 10 T requires that both the inner and outer (RE)BaCuO bulks are utilized at lower temperatures below 50 K [4]. In this study, the HTFML exploiting the "loose contact method" using one cold stage of a cryocooler realized such a realistic configuration which could work in a range of $B_{app}$ from 3 T to 7 T. A maximum $B_c$ = 9.8 T value was achieved successfully when magnetizing with $B_{app}$ = 7 T, although the flux creep was larger compared to that of lower $B_{app}$ values. The $B_c$-$B_{app}$ relation obtained from this experiment is consistent with our numerical estimations (indicated by the dotted line), but not for higher $B_{app}$ due to the larger flux creep for $B_{app}$ over 7 T and the mechanical fracture of the bulk materials over 10 T. This issue would be resolved by use of a more practical cooling method that can provide proper individual cooling of each part of the HTFML using one (or two) cold stages, combined with a switch that would work based on its thermal property and/or mechanical function. Furthermore, fundamental studies to understand and improve the thermal and mechanical stability of the stacked TFM cylinder during its magnetization would have an important role in improving the practical design of the HTFML.

## 5.4 Summary of Chapter 5

An all-(RE)BaCuO hybrid trapped field magnet lens (HTFML) magnetized under 50 K has been verified experimentally using only one cryocooler and a special technique named the "loose contact method", where the outer TFM was loosely connected to the cold stage before magnetizing process by introducing a gap between the cold stage. A maximum concentrated field of $B_c = 9.8$ T was achieved after magnetization with an applied field of $B_{app} = 7$ T, which is twice as superior as the other HTFML devices to date. The experimental $B_c$ values, as a function of $B_{app}$, were consistent with the numerical estimation reported in our previous conceptual study. These results validate the HTFML concept as a compact and desktop-type magnet device that can provide 10 T-class magnetic field enhancement from the viewpoint of the magnetizing method.

However, during magnetization with a higher $B_{app}$ of 10 T, the $B_c$ value suddenly dropped due to the occurrence of a large flux jump that resulted in the mechanical fracture of the bottom bulk in the stacked TFM cylinder, even though mechanical reinforcement using the SS support with the "hat structure" was applied. If the flux jump did not occur during magnetization from $B_{app} = 10$ T, it is predicted that $B_c = 13$ T would be achieved. To realize a $B_c$ value of over 10 T, further investigations are needed relating to the thermal stability of the stacked TFM cylinder and the development of a more practical cooling method that can achieve a stable and controllable cooling process for each part of HTFML.

## 5.5 References


[1] Li M, Li L and Xu D 2017 A Mechanical Thermal Switch for Conduction-cooled Cryogenic System *J. Phys.: Conf. Ser.* **897** 012016.

[2] Namba S, Fujishiro H, Hirano T, Naito T and Ainslie M D 2020 Optimized performance of an all-REBaCuO hybrid trapped field magnet lens (HTFML) with liquid nitrogen cooling *Physica C* **575** 1353690.

[3] Takahashi K, Fujishiro H and Ainslie M D 2020 Simulation study for magnetic levitation in pure water exploiting the ultra-high magnetic field gradient product of a hybrid trapped field magnet lens (HTFML) *J. Appl. Phys.* **127** 185106.

[4] Takahashi K, Fujishiro H and Ainslie M D 2018 A new concept of a hybrid trapped field magnet lens *Supercond. Sci. Technol.* **31** 044005.

[5] Morita M, Sawamura M, Takebayashi S, Kimura K, Teshima H, Tanaka M, Miyamoto K and Hashimoto M 1994 Processing and properties of QMG materials *Physica C* **235-240** 209-212.

[6] Fujishiro H, Takahashi K, Naito T, Yanagi Y, Itoh Y and Nakamura T 2018 New proposal of mechanical reinforcement structures to annular REBaCuO bulk magnet for compact and cryogen-

free NMR spectrometer *Physica C* **550** 52-56.

[7] Fujishiro H, Naito T, Yanagi Y, Itoh Y and Nakamura T 2019 Promising effects of a new *hat structure* and double metal ring for mechanical reinforcement of a REBaCuO ring-shaped bulk during field-cooled magnetization at 10 T without fracture *Supercond. Sci. Technol.* **32** 065001.

[8] Namba S, Fujishiro H, Naito T, Ainslie M D and Takahashi K 2019 Experimental realization of a hybrid trapped field magnet lens using a GdBaCuO magnetic lens and MgB2 bulk cylinder *Supercond. Sci. Technol.* **32** 12LT03.

# Chapter 6

# Simulation study for magnetic levitation in pure water exploiting the ultra-high magnetic field gradient product of a hybrid trapped filed magnet lens (HTFML)

# 6.1 Preface of Chapter 6

The realization of superconducting magnets that can generate stationary magnetic fields up to 40 Tesla has been encouraged by many types of fundamental studies related to magnetism: magnetic levitation [1-2] and separation [3-4], crystal growth [5-6] and nuclear magnetic resonance (NMR) [7-8]. The magnetic levitation technique, in particular, needs a strong magnetic field from an external magnet to realize the counter-balanced levitated situation against gravity acting on a diamagnetic material. The technique was first demonstrated for a diamagnetic water drop, in which the magnetic field gradient product, $B_z \cdot dB_z/dz$, was required to be as large as -1400 $T^2/m$ along the upper direction of the vertical magnet [9]. Such a large $B_z \cdot dB_z/dz$ value is required because of the low magnetic susceptibility of water and is difficult to achieve with a conventional superconducting magnet. Thus, up to now, such magnetic levitation has been realized only by using a comparatively large-scale hybrid magnet in a specialized facility [10]. In the past, such large-scale hybrid magnets have been demonstrated with $B_z \cdot dB_z/dz$ values around -1500 $T^2/m$ or better [11-12]. The $B_z \cdot dB_z/dz$ value for a standard 10 T cryo-cooled superconducting magnet is much lower, up to -500 $T^2/m$, which has been enhanced with a ferromagnetic iron yoke up to -1060 $T^2/m$ [2]. The magneto-Archimedes technique, proposed in 1998, also enables the reduction of the required $B_z \cdot dB_z/dz$ for the magnetic levitation of any target objects in a paramagnetic medium gas or liquid (*e.g.*, oxygen or aqueous $MnCl_2$) [13]. This method is utilized for the magnetic separation system for structural isomers of phthalic acid using oxygen and fluorocarbon instead of $MnCl_2$ solution, as introduced in [3]. In such magnetic applications, the whole system, including the magnetic source, separation unit and medium solution, must be considered, based on the physical properties of the target objects. It would be also desirable to avoid using any harmful materials, as well as to construct the separation system in a simple way for ease-of-processing, reliability and stability. The intensity of the magnetic force, $F_m$, is potentially restricted by the performance of the magnet used; however, it is not particularly cost-effective and realistic to build a conventional superconducting magnet or a large-scale magnet in any industrial facilities or laboratories, except for experimental purposes [6]. There is still a demand for a new magnetic field source that can provide both a stronger magnetic field, $B_z$, and magnetic field gradient product, $B_z \cdot dB_z/dz$, if it can be done in a cost-effective and efficient way.

Large, single-grain (RE)BaCuO bulk superconductors can trap or expel magnetic flux, owing to the induced supercurrent flowing inside the material with zero resistance, and that functionality depends on the magnetizing method. Towards practical engineering applications, research advances in bulk superconductivity, including the relevant technologies such as material processing, cryogenic systems and magnetization techniques, are summarized in [14].

Such superconducting bulks, magnetized by FCM as a so-called TFM can trap magnetic flux inside

the bulk.

Superconducting bulks, magnetized by ZFCM, can expel the external magnetic flux from its inside due to its "diamagnetic effect" and, as shown for the magnetic lens in the HTFML, can enhance a magnetic field in the central bore of the lens. The trapped field of the bulk could be enhanced by appropriate selection of the bulk materials for the TFM cylinder and lens, as well as the bulk $J_c$ and diameter. In addition to this function, it is considered that the HTFML could generate an ultra-high magnetic field gradient product, $B_z \cdot dB_z/dz$, which could, for example, be applicable to magnetic separation.

In this chapter, three-dimensional numerical models of the HTFML are constructed to investigate the magnetic field performance, in which realistic sizes and shapes of the bulk components and realistic $J_c$ characteristics are assumed, based on an experimental FCM setup. It is predicted that the HTFML could be highly applicable to magnetic levitation as a compact and strong magnetic field source and can generate a magnetic field gradient product, $B_z \cdot dB_z/dz$, over -3,000 $T^2$/m, which is six times higher than that of a conventional 10 T superconducting magnet (-500 $T^2$/m). These results provide further new understanding of the HTFML device and its potential wider use in industrial applications as a strong magnetic field source.

## 6.2 Numerical simulation framework

Electromagnetic phenomena during the magnetization process are described by the fundamental equations introduced in detail in [15-17]. The *E-J* power law is assumed to represent the highly nonlinear electrical properties of the superconducting material as follows;

$$E = E_c \left(\frac{J}{J_c}\right)^n, \qquad (6\text{-}2)$$

where $E_c$ (=$10^{-4}$ V/m) is the characteristic electric field, $n$ = 20 is the power-law exponent for GdBaCuO and $J_c$ is the critical current density.

Figure 6-1 shows a schematic view of the three-dimensional numerical model of the HTFML device, consisting of the outer GdBaCuO TFM cylinder and inner GdBaCuO lens pair, and the assumed dimensions are exactly the same as those used in the experimental verification of the HTFML presented in [18]. When this HTFML consists of the same superconducting material, *e.g.*, GdBaCuO, for each bulk component, the temperature of each part must be controlled independently, for which a so-called "thermal switch" would be required to control the superconducting state or the normal state during the magnetization process, where both ZFCM process for the inner magnetic lens and FCM process for the outer TFM cylinder are used simultaneously. This magnetizing process could be realized by utilizing an individually controlled cryostat or the same cryostat with different cooling loops for each component. The thermal switch used could be possibly realized mechanically [19], thermally [20] or magnetically.

The $J_c(B)$ characteristics of the GdBaCuO bulk are described by the following equation, proposed by Jirsa *et al.* [21],

$$J_c(B) = \beta \times \left\{ J_{c1} \exp\left(-\frac{B}{B_L}\right) + J_{c2} \frac{B}{B_{max}} \exp\left[\frac{1}{\alpha}\left(1 - \left(\frac{B}{B_{max}}\right)^{\alpha}\right)\right]\right\}, \qquad (6\text{-}3)$$

where each relevant parameter, $J_{c1}$, $B_L$, $J_{c2}$, $B_{max}$, and $\alpha$ are fitted from the experimental $J_c(B)$ profile. In this work, the experimentally measured $J_c(B)$ data for bulk GdBaCuO reported by Kii *et al.* in [22] is assumed, which come from a small sample. The fitting coefficient, $\beta$, was also employed to reproduce the actual trapped field from experimental results.

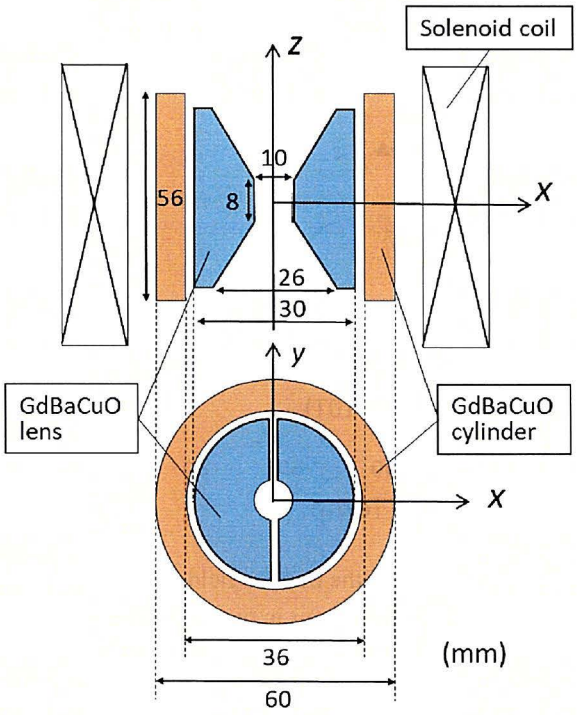


Figure 6-1. Schematic view of the three-dimensional numerical model of the HTFML, consisting of the outer GdBaCuO TFM cylinder and inner GdBaCuO lens pair. The assumed dimensions are exactly the same as those used in the experimental verification of the HTFML presented in [18].

To obtain the $\beta$ value at each temperature, our experimental FCM result for the GdBaCuO bulk ring was referred. Figure 6-2 presents the temperature dependence of the trapped field, $B_T$, in the ring-shaped GdBaCuO bulk (40 mm in inner diameter, 64 mm in outer diameter and 20 mm in height), which was magnetized by FCM from an applied field of 10 T at 50 K and then measured in the heating run as the temperature is increased to 93 K, *i.e.*, above its $T_c$ [23]. The experimental $B_T(T)$ curve would have a tendency to saturate under 50 K due to the full magnetization of the bulk within its $J_c$ capability. When the $J_c(B)$ characteristics obtained by SQUID magnetometer for a small piece of bulk sample ($\beta$ = 1) are used to estimate the $B_T$ value numerically at low temperature, *e.g.*, at 40 K and 20 K, the trapped field was overestimated and this saturation tendency cannot be reproduced. To reproduce the saturation tendency of $B_T(T)$ numerically, $\beta$ should be adjusted to be 0.50 for 40 K and 0.29 for 20 K, based on the extrapolation of the experimental $B_T(T)$ curve at lower temperatures. The parameters related to the data fitting are summarized in Table 6-1.

Figure 6-3 shows the time step sequence of the temperature of the TFM cylinder, $T_{TFM}$, and the magnetic lens, $T_{lens}$, and the external magnetic field, $B_{ex}$, at the center of the magnetic lens during the magnetizing process. At step 0, before the external field is applied, the bulk cylinder is cooled down to $T_H$, *e.g.*, 100 K, above its $T_c$ (= 92 K) from room temperature, and the bulk lens is cooled to $T_L$ (< $T_H$). In this study, two cases – $T_L$ = 40 K and $T_L$ = 20 K – are investigated for comparison. The bulk

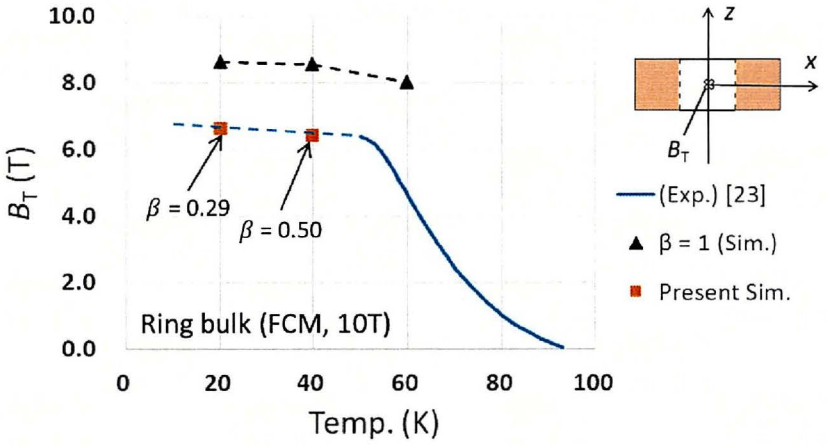


Figure 6-2. The temperature dependence of the trapped field, $B_T$, in the central bore of the ring-shaped GdBaCuO bulk (40 mm in inner diameter, 64 mm in outer diameter and 20 mm in height; referred to as TFM cylinder in figure 6-1), which was magnetized by FCM from an applied field of 10 T at 50 K and then measured in the heating run as the temperature is increased to 93 K. Numerical results of $B_T$ by FCM from 10 T for $\beta$ = 1 shown in equation (3) and the most suitable $B_T$ estimations at 20 K and 40 K are also shown (see text).

Table 6-1. Numerical fitting parameters for the $J_c(B)$ characteristics of bulk GdBaCuO used in equation (3), for 20 K and 40 K, where the $\beta$ value is adjusted to reproduce the experimental result for the trapped field in figure 6-2 (see text).

| $T$ (K) | $J_{c1}$ (A/m$^2$) | $B_L$ (T) | $J_{c2}$ (A/m$^2$) | $B_{max}$ (T) | $\alpha$ | $\beta$ |
|---|---|---|---|---|---|---|
| 20 | 9.0 x 10$^9$ | 1.5 | 5.4 × 10$^9$ | 8.0 | 0.5 | 0.29 |
| 40 | 3.5 x 10$^9$ | 0.9 | 2.7 × 10$^9$ | 6.0 | 0.8 | 0.50 |

temperature is assumed to be constant, under isothermal conditions; thus, any heat generation is ignored during the whole magnetizing process, assuming a near-static magnetic field. The magnetizing field, $B_{app}$, which corresponds to the maximum values of $B_{ex}$ = 3, 5 and 10 T, is applied using a solenoid coil. The magnetizing procedure is divided into two stages: (1) the ascending stage from step 0 to step 5, and (2) the descending stage from step 5 to step 10, where the externally applied field is ramped up and down linearly at ±0.222 T/min.

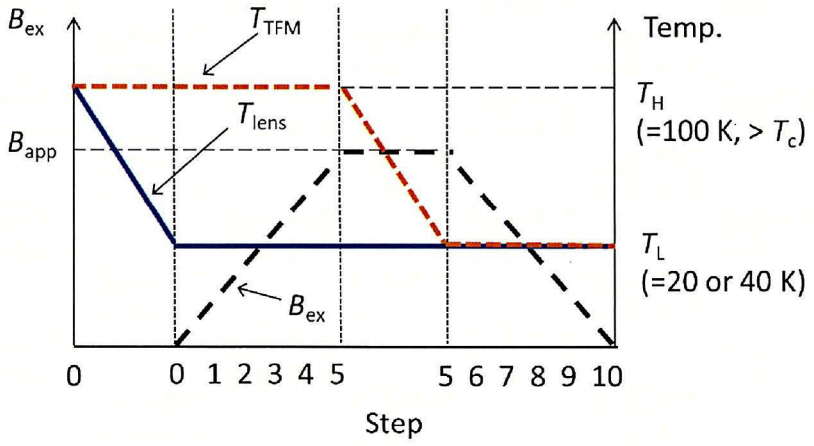


Figure 6-3. Time step sequence of the temperature of the TFM cylinder, $T_{TFM}$, and magnetic lens, $T_{lens}$, and the external magnetic field, $B_{ex}$, at the center of the magnetic lens during the magnetizing process, including the ascending stage from step 0 to 5, and the descending stage until step 10.

## 6.3 Numerical simulation results

The concentrated magnetic field, $B_c$, in the HTFML changes depending on the maximum applied field, $B_{app}$, and magnetizing temperature, $T_L$, which can also be deduced from the $J_c(B, T)$ characteristics indicated by equation (1). In this section, $B_{app}$ = 3, 5 and 10 T was applied at $T_L$ = 20 K and 40 K in an identical HTFML device using all GdBaCuO bulk materials, and those results are used to assess the performance of the HTFML in terms of magnetic field and magnetic field gradient product, $B_z \cdot dB_z/dz$.

Firstly, the magnetic flux dynamics and magnetization mechanisms of the HTFML are explained, by comparing the magnetic field profiles during the magnetization process for each externally applied field. Figure 6-4 shows the magnetic field profiles along the $x$ (radial)-direction at the middle of the magnetic lens, $z$ = 0 mm, during the magnetization process for the applied fields of $B_{app}$ = 3, 5 and 10 T for $T_L$ = 20 K, which is divided into (a) the ascending stage from steps 0 to 5, and (b) the descending stage from steps 5 to 10. In the ascending stage, when the TFM cylinder is kept in the normal state at 100 K, but the magnetic lens is already in the superconducting state at 20 K, the diamagnetic effect of the magnetic lens expels the external field from its inside within its $J_c(B)$ capability. As a result, a concentrated magnetic field of $B_c$ = 4.9 T was obtained in the bore of the lens for $B_{app}$ = 3 T at step 5, which becomes higher with increasing $B_{app}$; *i.e.*, $B_c$ = 7.4 T for $B_{app}$ = 5 T and $B_c$ = 12.5 T for $B_{app}$ = 10 T. It is worth mentioning here that some magnetic flux penetrates into the magnetic lens, positioned from $x$ = 5 to 15 mm, which becomes more obvious for higher $B_{app}$, and this will degrade the resultant concentrated field of the HTFML. In the descending stage, which includes the FCM process for the TFM cylinder at 20 K, the magnetic flux is gradually trapped in the TFM cylinder positioned at $x$ = 18 to 30 mm with increasing time step after step 5. The trapped field in the TFM cylinder at step 10 is roughly equal to $B_{app}$ (or slightly higher because the applied field profile is not completely homogeneous), which corresponds to the so-called partial magnetization of the TFM cylinder below its full capability (see figure 6-5(b), for example). The concentrated magnetic field in the magnetic lens appears to degrade little during the descending stage, compared to the ascending stage, indicating that the ascending stage of the magnetization would determine the remnant concentrated field in the HTFML after its magnetization. These numerical results during the magnetizing process are helpful towards achieving a higher magnetic field and a higher $B_z \cdot dB_z/dz$ value in the HTFML to improve its performance.

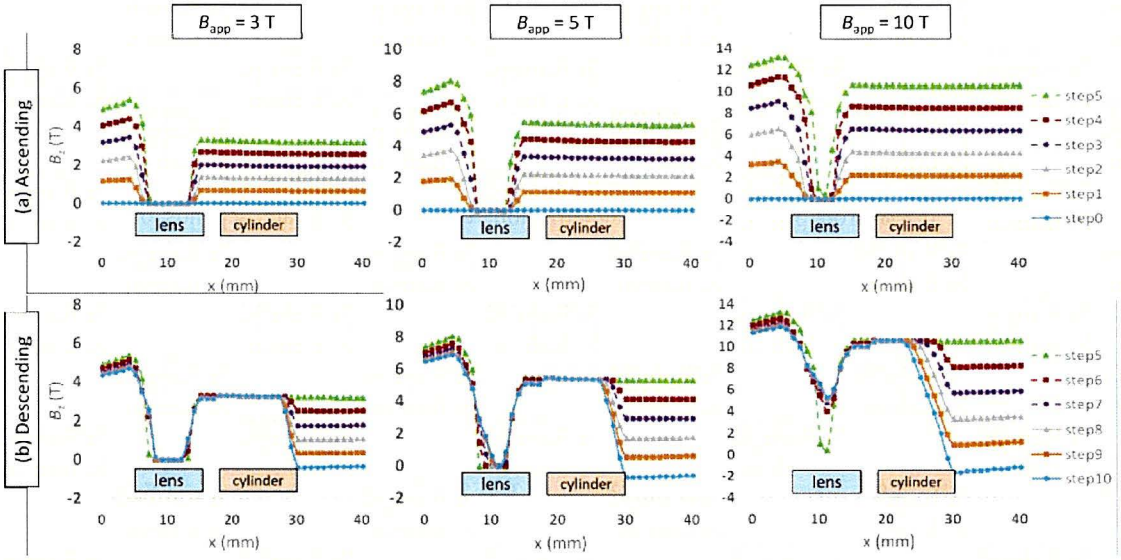


Figure 6-4. Magnetic field profiles along the $x$ (radial)-direction at the middle of the magnetic lens, $z$ = 0 mm, during the magnetization process from an applied field $B_{app}$ = 3, 5 and 10 T at $T_L$ = 20 K, which are divided into (a) the ascending stage from steps 0 to 5 and (b) the descending stage from steps 5 to 10.

Figures 6-5(a) and 6-5(b) show the cross-sectional profiles of the magnetic field, $B_z$, along the $z$ (height)-direction and the induced current density, $J_y$, along the $y$ (circumferential)-direction in the HTFML, after the magnetization process at step 10 for each $B_{app}$ at $T_L$ = 20 K. As already shown in figure 6-4(a), the flux penetration into the magnetic lens is more remarkable for higher applied fields, as shown in figure 6-5(a). In the case of $B_{app}$ = 10 T, there is no region of 0 T inside the magnetic lens, meaning that the magnetic flux completely penetrates the inside of the lens during the magnetization process. In figure 6-5(b), inside each part of the magnetic lens, the induced current flows in the opposite direction to that in the TFM cylinder due to the existence of the slits in the hollow cone (see figure 6-1). The $J_y$ profile also indicates the flux penetration into the magnetic lens for higher $B_{app}$. The magnetic lens can only exhibit the diamagnetic effect with an induced current flowing predominately on its surface, whereas the TFM cylinder generates its strongest trapped field by an induced current flowing through the entire cross-section of the TFM cylinder.

Figures 6-6(a) and 6-6(b) show the time step dependence of the concentrated magnetic field, $B_c$, in the central bore of the magnetic lens ($x = y = z = 0$ mm) and the magnetic field concentration ratio, $B_c/B_{app}$, respectively, extracted from figure 6-4 for each $B_{app}$ at $T_L$ = 20 K. The concentration ratio can be referred to characterize the diamagnetic lens effect, which is determined by the shape of lens, including the outer and inner diameter, the outer and inner height and the angle of the slits [24]. From these results, a higher applied field is needed to achieve a higher concentrated field at any time step, as shown in figure 6-6 (a), although the concentration ratio gradually degrades as the magnetization process proceeds from step 0 to step 10, as shown in figure 6-6(b). The so-called decay behavior in the

bulk magnet due to flux creep usually exhibits an approximately logarithmic time dependence, as reported in the case only using the magnetic lens. If the outer TFM cylinder can provide a homogeneous magnetic field and replace outer magnetizing coil used for magnetizing process, the similar trend would be obtained also in this HTFML as well, which means a concentrated field of 5 T could be maintained by only about 0.1% drop per hour after magnetization; but that decay rate depends on operating temperature and applied magnetic field [25]. It may be needed to develop a new magnetizing sequence to improve a temporal stabilization of magnetic flux after magnetizing process, specifically for magnetic separation.

Figures 6-7(a) and 6-7(b) show the resultant magnetic field, $B_z$, profiles ($x = y = 0$ mm) along the $z$-(height) direction, after magnetization from $B_{app}$ = 10 T at $T_L$ = 20 K, and the magnetic field gradient product, $B_z \cdot dB_z/dz$, profile ($x = y = 0$ mm), respectively. A schematic image of the HTFML is also shown for reference, indicating the corresponding position in the HTFML. A characteristic feature of the HTMFL is based on the existence of magnetic lens located inside the homogeneous trapped field generated from the TFM cylinder, which enables the generation of a higher *inhomogeneous* magnetic field by exploiting the diamagnetic effect of magnetic lens. As a result, the HTFML also has a significant ability to produce an intentional ultra-high magnetic field gradient product of $B_z \cdot dB_z/dz$ = ±3,000 $T^2$/m, just below and above the lens center at $z = \pm 5$ mm, for a concentrated field of $B_c$ = 11. 4 T for $B_{app}$ =10 T. This value is comparable with that produced by a > 20 T-class, large-scale hybrid magnet [26].

Another parameter that determines the HTFML performance is the magnetizing temperature $T_L$ in figure 6-3. Hence, the HTFML performance was explored for the higher magnetizing temperature $T_L$ = 40 K to compare with $T_L$ = 20 K. Figure 6-8 summarizes the applied field dependence of the HTFML properties, including (a) the concentrated magnetic field, $B_c$, at the center of the GdBaCuO lens, (b) maximum $|B_z \cdot dB_z/dz|$ and (c) concentration ratio, $B_c/B_{app}$, for each $T_L$. The difference in $B_c$ is reasonably small for each $T_L$ in figure 6-8(a), but $|B_z \cdot dB_z/dz|$ in figure 6-8(b) at $T_L$ = 20 K is 500 $T^2$/m larger than that at $T_L$ = 40 K for the applied field $B_{app}$ = 10 T. A lower $T_L$ is desirable for a higher applied field, resulting in a higher $B_c$ and higher $|B_z \cdot dB_z/dz|$, although the diamagnetic effect degrades with increasing $B_{app}$ for each $T_L$, as shown by $B_c/B_{app}$ in figure 6-8(c). The obtained $B_c$ and the maximum $B_z \cdot dB_z/dz$ are summarized for each applied field, $B_{app}$, in Table 6-2. There is scope for further improvement of the HTFML performance as a strong magnet in terms of both the magnetic design of each bulk component and their magnetizing conditions.

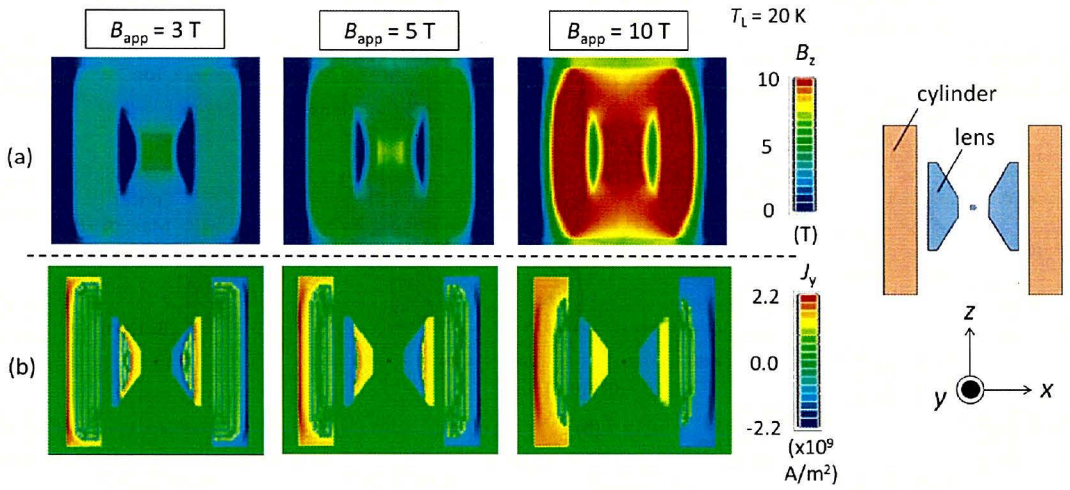


Figure 6-5. Cross-section of (a) the magnetic field, $B_z$, profile along the $z$ (height)-direction and (b) the induced current density, $J_y$, along the $y$ (circumferential)-direction in the HTFML, after the magnetization process at step 10 for each applied field, $B_{app}$, at $T_L$ = 20 K.

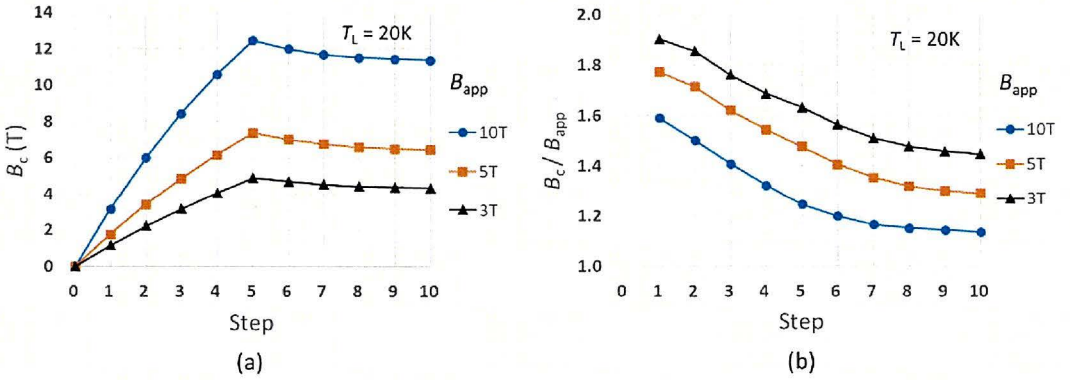


Figure 6-6. Time step dependence of (a) the concentrated magnetic field, $B_c$, in the central bore of GdBaCuO lens ($x = y = z = 0$ mm), and (b) the magnetic field concentration ratio, $B_c/B_{app}$, extracted from figure 6-4 for each $B_{app}$ at $T_L$ = 20 K.

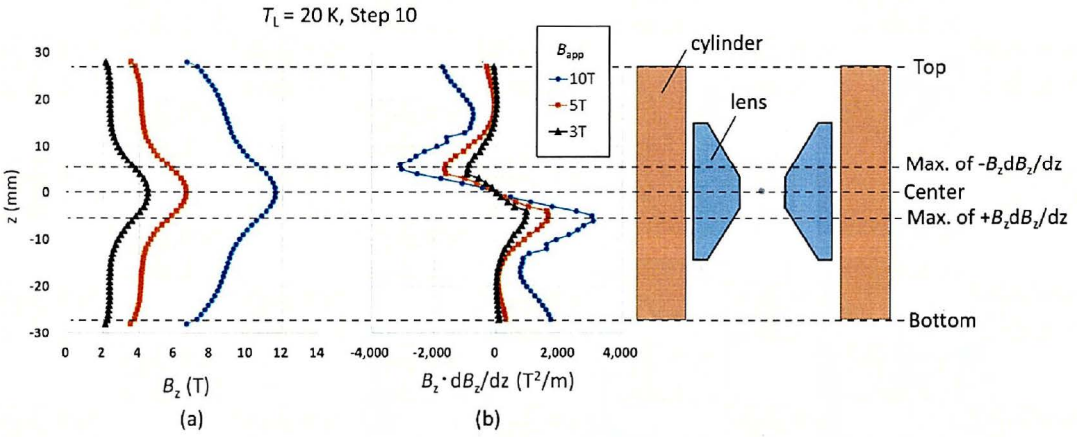


Figure 6-7. Resultant magnetic field, $B_z$, profiles ($x = y = 0$ mm) along the $z$ (height)-direction after the magnetization process (step 10) from $B_{app}$ = 10 T at $T_L$ = 20 K, and the magnetic field gradient product, $B_z \cdot dB_z/dz$, profiles ($x = y = 0$ mm). A schematic image of the HTFML is also shown for reference, indicating the corresponding position in the HTFML.

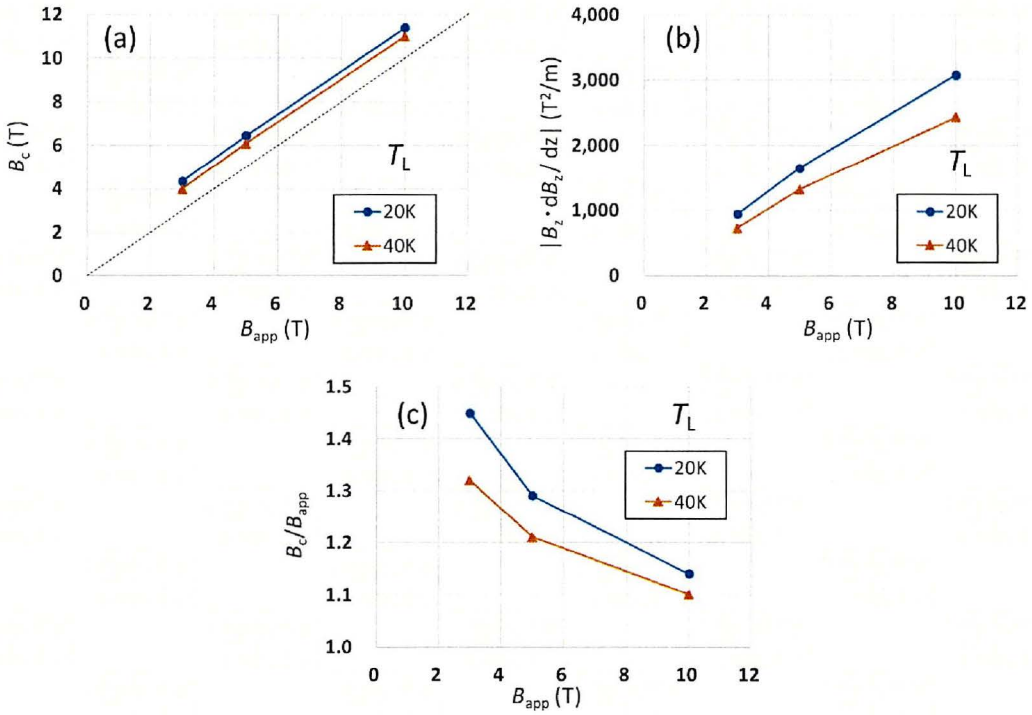


Figure 6-8. Applied field dependence of the HTFML properties for (a) the concentrated magnetic field, $B_c$, at the center of the GdBaCuO lens, (b) the maximum of the magnetic field gradient product, $|B_z \cdot dB_z/dz|$, and (c) the concentration ratio, $B_c/B_{app}$, for each $T_L$.

Table 6-2. Maximum applied field, $B_{app}$, concentrated magnetic field, $B_c$, at the center of the GdBaCuO lens at the final step of the magnetizing process (step 10), magnetic field concentration ratio, $B_c/B_{app}$, and maximum of the magnetic field gradient product, $B_z \cdot dB_z/dz$, at $T_L$ = 20 K and 40 K.

| $T_L$ (K) | $B_{app}$ (T) | $B_c$ (T) | $B_c/B_{app}$ | $B_z \cdot dB_z/dz$ ($T^2/m$) |
|---|---|---|---|---|
| 20 K | 10 | 11.4 | 1.14 | -3,080 |
| | 5 | 6.45 | 1.29 | -1,650 |
| | 3 | 4.34 | 1.45 | -943 |
| 40 K | 10 | 11.0 | 1.10 | -2,430 |
| | 5 | 6.07 | 1.21 | -1,320 |
| | 3 | 3.97 | 1.32 | -724 |

## 6.4 Possibility of magnetic separation using the ultra-high magnetic field gradient product

In this section, the superiority of the HTFML as a strong magnet applied to magnetic levitation or separation is discussed. The HTFML could, for example, be highly applicable to magnetic separation, which needs a large magnetic field gradient product, $B_z \cdot dB_z/dz$, over -2,000 $T^2/m$ to realize the so-called "apparent zero gravity" condition, even in water or air for any diamagnetic objects with the magnetic susceptibility $\approx -10^{-5}$, such as metals, foods or plastics.

The total potential energy per unit mass of a substance dispersed in a medium, *e.g.*, liquid or gas, is expressed by [27],

$$U = -\frac{1}{2\mu_0}(\chi_s - \chi_m)\boldsymbol{B}^2 + (\rho_s - \rho_m)gz, \qquad (6\text{-}4)$$

where $\mu_0$ is the vacuum permeability, $\boldsymbol{B}$ is the field intensity, $g$ is the acceleration due to gravity, and $z$ is the vertical position. $\chi_s$ and $\rho_s$ are the susceptibility and density of the target substance, respectively. $\chi_m$ and $\rho_m$ are the same parameters for the medium, such as liquid or gas. The total magnetic force, $F_z$, along $z$ (central axis)-direction at $x = y = 0$ mm, is

$$F_z = -\frac{\partial U_{(x=y=0)}}{\partial z} = F_m + F_g = \frac{(\chi_s - \chi_m)}{\mu_0} B_z \frac{dB_z}{dz} - (\rho_s - \rho_m)g. \qquad (6\text{-}5)$$

$F_z$ is determined by the $B_z \cdot dB_z/dz$ value, which changes in the vertical bore of the magnet as shown in figure 6-7(b). The equilibrium condition for magneto-Archimedes levitation, which corresponds to $F_z = 0$, can then be written as

$$B_z \frac{dB_z}{dz} = \frac{\rho_s - \rho_m}{\chi_s - \chi_m}\mu_0 g. \qquad (6\text{-}6)$$

Figure 6-9 shows a schematic image of magnetic separation using the HTFML device. Several kinds of substances of different susceptibility and density are dispersed in the medium, *e.g.*, water in the tube. When the tube is inserted into the central bore of the magnetized HTFML device, each substance is re-arranged vertically according to the differences in $\chi_s$ and $\rho_s$ of each substance. Most simply, in this case, a collecting capillary tube could be used for the recovery process and should be placed above the optional height of each substances floated in the glass tube in the HTFML device.

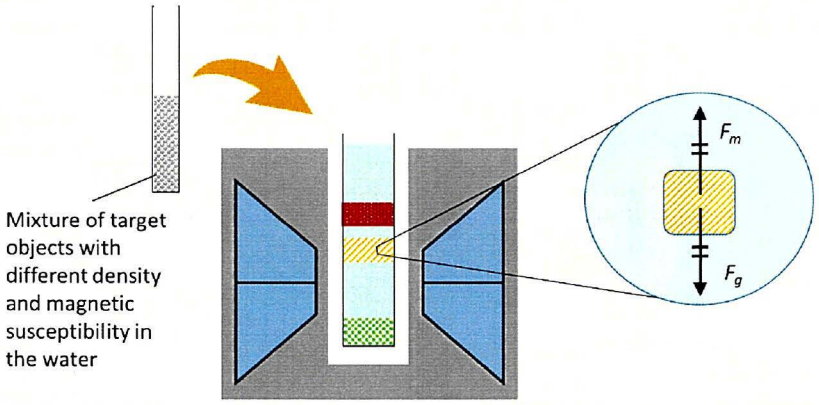


Figure 6-9. Schematic image of magnetic separation using the magnetized HTFML device, in which the force balance between gravity, $F_g$, and the magnetic repulsive force, $F_m$, is realized for each substance in the medium, *e.g.*, water, at particular positions related to the magnetic field gradient product.

Figures 6-10(a) and 6-10(b), respectively, show cross-sectional views of $B_z$ and $B_z \cdot dB_z/dz$ in the $xz$ (vertical)-plane at $y$ = 0 mm and the $xy$ (horizontal)-plane at $z$ = 0 mm of the HTFML, after magnetization from $B_{app}$ = 10 T at 20 K. The effective hollow area for levitation is indicated by the dotted line. As shown in figure 6-10(a), the $B_z \cdot dB_z/dz$ value changes from -3,000 to +3,000 $T^2/m$ along the vertical direction in this area of $\varphi$10 mm x ±30 mm in height in the bore of the magnetic lens for the present HTFML.

For magnetic separation, a large $B_z \cdot dB_z/dz$ would be needed for a variety of cases, especially if the density of the target object is heavy, such as platinum ($\rho_s$ = 21.5 $g/cm^3$), and/or its magnetic susceptibility is exceedingly low, such as water ($\chi_m$ = -9.03 x $10^{-6}$). The use of harmful paramagnetic medium liquids, such as $MnCl_2$ solution, should be avoided for food and medical use [3].

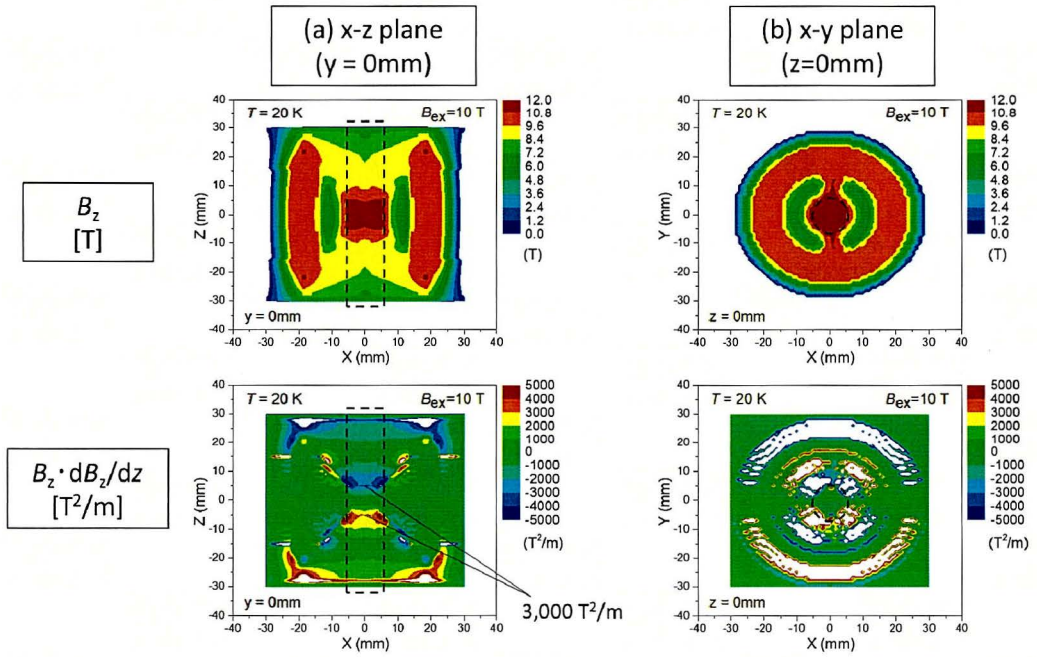


Figure 6-10. Cross-sectional views of the resultant $B_z$, and $B_z \cdot dB_z/dz$ along (a) the *xz* (vertical)-plane at $y$ = 0 mm and (b) the *xy* (horizontal)-plane at $z$ = 0 mm of the HTFML, after magnetization from $B_{app}$ = 10 T at 20 K.

Hereafter, the levitation position of the target object in the HTFML is estimated for kinds of precious metals (Pt, Au, Ag and Cu) based on the magneto-Archimedes effect described by equation (6-4). The relevant physical parameters of the objects, referred from [2], are presented in Table 6-3. The parameters for aqueous $MnCl_2$ solution with concentrations of $MnCl_2$, 50 wt% and 12 wt%, and 0 wt% (i.e., pure water), are also referred from [2, 3, 13]. The required magnetic field gradient product, $B_z \cdot dB_z/dz$, for levitation increases with decreasing concentration of $MnCl_2$ in the solution. All of the precious metals can levitate in the HTFML for $MnCl_2$ concentrations of 50 wt% and 12 wt%. However, for the 0 wt% $MnCl_2$ solution (pure water), only copper needs a higher $B_z \cdot dB_z/dz$ value of over -7,000 $T^2/m$ in water due to its high density and low susceptibility, which exceeds the capability of the present HTFML device. As a result, copper sinks in water, but the other precious metals can stably levitate at different heights in the bore of the HTFML.

Figure 6-11 shows the estimated levitation position of each precious metal in the pure water solution in the central bore of the HTFML magnetized by $B_{app}$ = 10 T at 20 K. Magnetic levitation would be realized in the case when the object is stably lifted from beneath by the repulsive magnetic force; that is, the effective area exists above a negative peak of $B_z \cdot dB_z/dz$ at $z$ = +5 mm for a diamagnetic object and above a positive peak at $z$ = -5 mm for a paramagnetic object. For the precious metals in Table 6-3, magnetic levitation could be realized at $z$ = +11 mm for the diamagnetic gold ($B_z \cdot dB_z/dz$ = -1401 $T^2/m$) and at $z$ = +6 mm for the diamagnetic silver ($B_z \cdot dB_z/dz$ = -2800 $T^2/m$) above the negative

$B_z \cdot dB_z/dz$ peak. On the other hand, magnetic levitation could be realized at $z$ = -8 mm for the paramagnetic platinum ($B_z \cdot dB_z/dz$ = +2210 $T^2$/m) above the positive $B_z \cdot dB_z/dz$ peak. However, copper would settle at the bottom of the tube because it is outside of the present HTFML's magnetic separation capability.

With respect to the recovery method, a suitable one has not been proposed yet, and it should be determined on the basis of the separation method and target material(s). A separation and recovery experiment was reported by Ando *et al.* [27], in which glass particles floated by the magneto-Archimedes method were collected using movable partitions into each compartment in their device.

Table 6-3. Density and susceptibility of the example metals and calculated $B_z \cdot dB_z/dz$ values to levitate them in aqueous $MnCl_2$ solutions with concentrations 50 wt% and 12 wt% $MnCl_2$, and 0 wt% (i.e., pure water). The parameters for aqueous $MnCl_2$ solutions are also shown for reference from [2, 3, 13].

| Metal | Density ($\rho_s$) (g/m$^3$) | Susceptibility ($\chi_s$) | Calculated $B_z \cdot dB_z/dz$ (T$^2$/m) | | |
|---|---|---|---|---|---|
| | | | $MnCl_2$ (50 wt%) | $MnCl_2$ (12 wt%) | $MnCl_2$ (0 wt%; pure water) |
| Platinum | 21.5 | $1.05 \times 10^{-4}$ | -805 | -2388 | +2210 |
| Gold | 19.3 | $-1.70 \times 10^{-4}$ | -380 | -590 | -1401 |
| Silver | 5.56 | $-2.91 \times 10^{-5}$ | -118 | -230 | -2800 |
| Copper | 8.96 | $-2.25 \times 10^{-5}$ | -216 | -417 | -7282 |

| Medium | Density ($\rho_m$) (g/m$^3$) | Susceptibility ($\chi_m$) |
|---|---|---|
| $MnCl_2$ (50 wt%) | 1.33 | $4.13 \times 10^{-4}$ |
| $MnCl_2$ (12 wt%) | 1.10 | $2.10 \times 10^{-4}$ |
| $MnCl_2$ (0 wt%; pure water) | 1.00 | $-9.03 \times 10^{-6}$ |

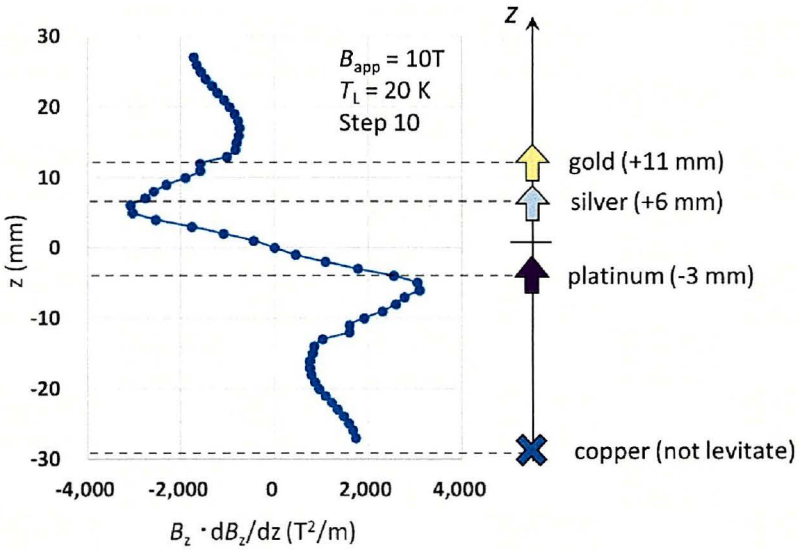


Figure 6-11. Estimated levitation positions for each precious metal in the pure water solution in the central bore of the HTFML magnetized by $B_{app}$ = 10 T at 20 K.

Thus, the superiority of the HTFML to achieve magnetic separation using its ultra-high magnetic

field gradient product has been proposed from the following viewpoints:

(1) Realization of an ultra-high magnetic field gradient product, $B_z \cdot dB_z/dz$: there are a limited number of facilities worldwide that can generate a $B_z \cdot dB_z/dz \sim 2{,}000$ T$^2$/m for magnetic levitation. Figure 6-12 summarizes the relationship between the applied magnetic field, $B_{app}$, and the magnetic field gradient product, $B_z \cdot dB_z/dz$, for superconducting magnets (SM) and large-scale hybrid magnets (HM) around the world [2, 11, 28-33], which are compared to the numerical results for the present HTFML device. The HTFML would generate quasi-permanently, an ultra-high magnetic field gradient product higher than that of conventional SMs and large-scale HMs, even for a lower applied field of 10 T, which is enhanced due to the presence of the magnetic lens.

(2) Compact size and mobility: this kind of high magnetic field source utilizing the HTFML would be a compact and mobile desktop-type superconducting bulk magnet system. Thus, it may be possible to improve the accessibility to strong magnetic fields in a variety of food, medical and industrial applications.

(3) Mass productivity: Superconducting bulk magnets such as REBaCuO, fabricated by the melt-growth technique, and $MgB_2$, fabricated by the reactive Mg liquid infiltration, are available commercially and are being used in commercial products. In addition, a cryogenic refrigerator enables thermal control of the bulks in a compact and light-weight cryostat. The HTFML magnet, which consists of these technology-intensive components, is superior in terms of mass productivity to carry out high-throughput continuous separation in devices with different magnetic field gradient products.

(4) Cost efficiency: Unlike a conventional separation technique based on chemical processes, this HTFML would not need other energy consumptions for magnetic separation due to superconducting current that keeps flowing inside the bulk quasi-permanently, if the operating temperature is preserved, for which the bulk is kept as below $T_c$ in the HTFML. It is possible to establish and operate the HTFML system using a cryogen-free refrigerator, which only needs electric power consumption for operation as a more cost-effective way without any coolants such as liquid nitrogen or liquid helium.

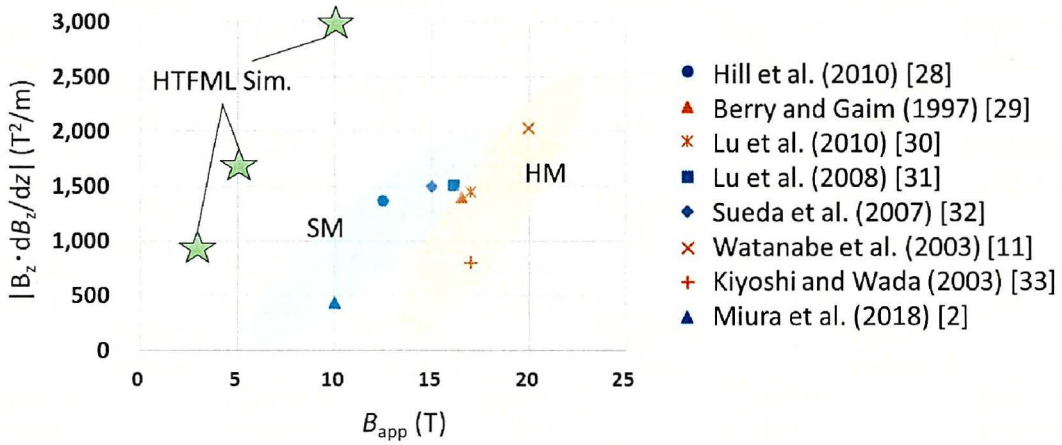


Figure 6-12. Relationship between the applied magnetic field, $B_{app}$, and the magnetic field gradient product, $|B_z \cdot dB_z/dz|$, for superconducting magnets (SM) and large-scale hybrid magnet (HM) around the world [2, 11, 28-33], which are compared to the numerical results for the HTFML.

## 6.5 Summary of Chapter 6

In this chapter, the author has proposed and analyzed a new advantage of the HTFML by numerical simulations, other than the ability to provide a continuous, concentrated magnetic field higher than the applied field reported previously: exploiting the HTFML's ultra-high magnetic field gradient product, $B_z \cdot dB_z/dz$, which could be highly applicable to magnetic levitation and separation as a compact and strong magnetic field source. The HTFML device consisting of a GdBaCuO TFM cylinder and GdBaCuO magnetic lens after magnetization from 10 T can generate a concentrated magnetic field, $B_c$, of 11.4 T and a $B_z \cdot dB_z/dz$ over $\pm$3,000 $T^2/m$, which is higher than that of other superconducting magnets (SM) and large-scale hybrid magnets (HM) around the world. The usefulness of the HTFML device in this respect was discussed based on numerical results for magnetic separation of a mixture of precious metal particles (Pt, Au, Ag and Cu) dispersed in pure water, exploiting the magneto-Archimedes effect. The HTFML device enables the design of a compact and mobile desktop-type superconducting bulk magnet system and can improve the accessibility to strong magnetic fields in a variety of food, medical and industrial applications.

## 6.6 References


[1] M A Weilert, D L Whitaker, H J Maris and G M Seidel 1996 Magnetic Levitation and Noncoalescence of Liquid Helium *Phys. Rev. Lett.* **77** 4840.

[2] O Miura, K Yamagishi and D Yamamoto 2018 Magneto-Archimedes levitation of precious metals under a high magnetic field gradient *J. Phys.: Conf. Ser.* **1054** 012086.

[3] T Kobayashi, T Mori, Y Akiyama, F Mishima and S Nishijima 2017 Study on Separation of Structural Isomer with Magneto-Archimedes method *J. Phys.: Conf. Ser.* **897** 012018.

[4] T Oka, K Tanaka, T Kimura, D Mimura, S Fukui, J Ogawa, T Sato, M Ooizumi, K Yokoyama and M Yamaguchi 2010 Magnetic separation technique for environmental water purification by strong magnetic field generator loading HTS bulk magnets *Physica C* **470** 1799.

[5] K Takahashi, I Mogi, S Awaji, M Motokawa and K Watanabe 2006 Containerless melting and crystallization of diamagnetic organic materials under magnetic levitation condition *J. Phys.: Conf. Ser.* **51** 450.

[6] D-C Yin 2015 Protein crystallization in a magnetic field *Prog. Cryst. Growth Charact. Mater.* **61** 1.

[7] K Hashi, S Ohki, S Matsumoto, G Nishijima, A Goto, K Deguchi, K Yamada, T Noguchi, S Sakai, M Takahashi, Y Yanagisawa, S Iguchi, T Yamazaki, H Maeda, R Tanaka, T Nemoto, H Suematsu, T Miki, K Saito and T Shimizu 2015 Achievement of 1020 MHz NMR *J. Magn. Reson.* **256** 30.

[8] H Maeda, T Yamazaki, Y Nishiyama, M Hamada, K Hashi, T Shimizu, H Suematsu and Y

Yanagisawa 2016 Development of Super - High - Field NMR Operated Beyond 1 GHz Using High - Temperature Superconducting Coils *eMagRes* **5** 1109.

[9] Y Ikezoe, T Kaihatsu, D Sakae, H Uetake, N Hirota and K Kitazawa 2002 Separation of feeble magnetic particles with magneto-Archimedes levitation *Energ. Convers. Manage.* **43** 417.

[10] V S Nikolayev, D Chatain, D Beysens and G Pichavant 2010 Magnetic Gravity Compensation *Microgravity. Sci. Technol.* **23** 113.

[11] K Watanabe, K Takahashi, I Mogi, G Nishijima, S Awaji and M Motokawa 2003 Cryogen-free hybrid magnet for magnetic levitation *Physica C* **386** 485.

[12] Y M Liu, D M Zhu, DM Strayer and U E Israelsson 2010 Magnetic levitation of large water droplets and mice *Adv. Space. Res.* **45** 208.

[13] Y Ikezoe, Y Hirota, J Nakagawa and K Kitazawa 1998 Making water levitate *Nature* **393** 749.

[14] J H Durrell, M D Ainslie, D Zhou, P Vanderbemden, T Bradshaw, S Speller, M Filipenko and D A Cardwell 2018 Bulk superconductors: a roadmap to applications *Supercond. Sci. Technol.* **31** 103501.

[15] H Fujishiro and T Naito 2011 Simulation of temperature and magnetic field distribution in superconducting bulk during pulsed field magnetization *Supercond. Sci. Technol.* **23** 105021.

[16] H Fujishiro, M D Ainslie, K Takahashi, T Naito, Y Yanagi, Y Itoh and T Nakamura 2017 Simulation studies of mechanical stresses in REBaCuO superconducting ring bulks with infinite and finite height reinforced by metal ring during field-cooled magnetization *Supercond. Sci. Technol.* **30** 085008.

[17] K Takahashi, H Fujishiro, T Naito, Y Yanagi, Y Itoh and T Nakamura 2017 Fracture behavior analysis of EuBaCuO superconducting ring bulk reinforced by a stainless steel ring during field-cooled magnetization *Supercond. Sci. Technol.* **30** 115006.

[18] S Namba, H Fujishiro, T Naito, M D Ainslie and K Takahashi 2019 Experimental realization of a hybrid trapped field magnet lens using a GdBaCuO magnetic lens and $MgB_2$ bulk cylinder *Supercond. Sci. Technol.* **32** 12LT03.

[19] M Li, L Li, D Xu 2017 A Mechanical Thermal Switch for Conduction-cooled Cryogenic System *J. Phys.: Conf. Ser.* **897** 012016.

[20] P J Masson, M Breschi, P Tixador and C A Luongo 2007 Design of HTS Axial Flux Motor for Aircraft Propulsion *IEEE Trans. Appl. Supercond.* **17** 1533.

[21] M Jirsa, L Půst, D Dlouhý and M R Koblischka 1997 Fishtail shape in the magnetic hysteresis loop for superconductors:Interplay between different pinning mechanisms *Phys. Rev.* B **55** 3276.

[22] T Kii, R Kinjo, N Kimura, M Shibata, M A Bakr, Y W Choi, M Omer, K Yoshida, K Ishida, T Komai, K Shimahashi, T Sonobe, H Zen, K Masuda and H Ohgaki 2012 Low-Temperature Operation of a Bulk HTSC Staggered Array Undulator *IEEE. Trans. Appl. Supercond.* B **22** 4100904.

[23] H Fujishiro, T Naito, Y Yanagi, Y Itoh and T Nakamura 2019 Promising effects of a new hat structure and double metal ring for mechanical reinforcement of a REBaCuO ring-shaped bulk during field-cooled magnetisation at 10 T without fracture *Supercond. Sci. Technol.* **32** 065001.

[24] S Namba, H Fujishiro, M D Ainslie, K Takahashi, D K Nambri, D Zhou and T Naito 2019 Design Optimization of a Hybrid Trapped Field Magnet Lens (HTFML) *IEEE. Trans. Appl. Supercond.* **29** 6801605.

[25] ZY Zhang, S Matsumoto, R Teranishi and T Kiyoshi 2013 Improving the properties of GdBCO magnetic lenses by adopting a new design and resin impregnation *Supercond. Sci. Technol.* **26** 045001.

[26] K Watanabe, G Nishijima, S Awaji, K Takahashi, K Koyama, N Kobayashi, M Ishizuka, T Itou, T Tsurudome and J Sakurada 2006 Performance of a Cryogen-Free 30 T-Class Hybrid Magnet *IEEE. Trans. Appl. Supercond.* **16** 934.

[27] T Ando, N Hirota and M Maie 2015 Development of recovery device for particulates in fluid by magneto-Archimedes separation *Sep. Prif. Technol.* **149** 197.

[28] R J A Hill, O J Larkin, P Anthony, M R Davey, L Eaves, C E D Rees and C E Dijkstra 2010 Effects of diamagnetic levitation on bacterial growth in liquid *Nat. Proc.* 4216.2.

[29] M V Berry and A K Geim 1997 Of flying frogs and levitrons *Eur. J. Phys.* **18** 307.

[30] Y Liu, D M Zhu, D M Strayer and U E Israelsson 2010 Magnetic levitation of large water droplets and mice *Adv. Space. Res.* **45(1)** 208.

[31] H M Lu, D C Yin, H S Li, L Q Geng, C Y Zhang, Q Q Lu, Y Z Guo, W H Guo, P Shang and N I Wakayama 2008 A containerless levitation setup for liquid processing in a superconducting magnet *Rev. Sci. Instrum.* **79(9)** 093903.

[32] M Sueda, A Katsuki, M Nonomura, R Kobayashi and Y Tanimoto 2007 Effects of High Magnetic Field on Water Surface Phenomena *J. Phys. Cam. C.* **111(39)** 14389.

[33] T Kiyoshi and H Wada 2003 Development of Advanced High-Field Magnets at the Tsukuba Magnet Laboratory *J. Low. Temp. Phys.* **133(1)** 31.

# Chapter 7

# A conceptual study of a High Gradient Trapped Field Magnet (HG-TFM) toward providing a quasi-zero gravity space on Earth

# 7.1 Preface of Chapter 7

Zero gravity in space is known to be a characteristic condition in scientific research fields. Up to now, some experimental research has been carried out exploiting quasi-zero gravity conditions in the International Space Station (ISS) as an environmental parameter, which focuses positively on applications related to life/medical sciences, such as protein crystallization [1] and cell culture [2] without natural convection caused by the gravitational force of the Earth. The so-called "space biology" resulting from this research is an important developing field that could contribute significantly to the Sustainable Development Goals (SDGs).

A large magnetic field in combination with a large field gradient can provide a repulsive force against gravity on the Earth and achieve a counter-balance situation for any diamagnetic materials such as water, common metals and even cells of the human body. In 1990, magnetic levitation of diamagnetic materials such as water and plastics was first demonstrated by Beaugnon *et al* using a hybrid-type superconducting magnet (HM), in which a magnetic field gradient product, $B_z \cdot dB_z/dz$, as high as -1923 $T^2/m$ was applied along the vertical direction against gravity on Earth [3].

Superconducting technologies have satisfied several demands for high magnetic fields including magnetic levitation. Nikolayev *et al* summarizes the specification of existing superconducting magnets worldwide, where the highest $B_z \cdot dB_z/dz$ = -3000 $T^2/m$ with a record-high magnetic field of 30 T has been ever achieved in a HM and superconducting coil magnet (SM) [4]. Cryo-cooled superconducting magnets without liquid helium that can generate $B_z \cdot dB_z/dz$ up to -400 $T^2/m$ with magnetic fields up to 10-12 T are now used practically at the laboratory scale.

The magnetic force, $F_m$, acting on a material increases in proportional to the magnetic field, $B_z$, and the magnetic field gradient, $dB_z/dz$, along the $z$-axis (upper direction) as follows,

$$F_m \propto B_z \cdot \frac{dB_z}{dz}. \qquad (7-1)$$

To enhance $F_m$, there are some trends related to the magnet design, *i.e.*, the improvement of $B_z$ and/or $dB_z/dz$. One example is the gradient-type superconducting magnet developed for protein crystallization, in which an inverse coil made from $Nb_3Sn$ was placed on the hybrid coil, consisting of an inner $Nb_3Sn$ coil and outer NbTi coils. As a result, the magnet can generate a $B_z \cdot dB_z/dz$ as large as -1500 $T^2/m$ around the boundary of both coils [5]. The most significant issue is that such a comparatively large $B_z \cdot dB_z/dz$ value has been realized only in a specialized facility [4]. For practical use of a magnetic quasi-zero gravity condition on ground, it is desirable for the magnetic source to be lightweight, mobile, and cost-effective as a desktop-type apparatus, and preferably

cryogen-free, *i.e.*, operating without the need for any coolant such as liquid helium.

In the case of the HTFML using a GdBaCuO bulk lens and GdBaCuO TFM cylinder, a magnetic field gradient product as high as $B_z \cdot dB_z/dz$ = -3000 $T^2$/m could be generated inside the bulk annuli under the concentrated trapped field of $B_c$ = 11.4 T at 20 K, which allows for a quasi-zero gravity environment in a cost-effective and efficient way [6]. However, the HTFML device has some challenges in its construction and the magnetizing process. The temperature of the GdBaCuO bulk lens and the GdBaCuO TFM cylinder must be controlled individually during ZFCM for the lens part and FCM for the TFM part. A special technique is required in order to control the temperature separately and the magnetization process can take several hours. Moreover, it is quite difficult to realize a room temperature bore for practical applications exploiting the advantages of the HTFML because of a narrow bore less than 10 mm in diameter in the GdBaCuO lens, which is also encapsulated in a stainless steel (SS) holder. This does limit the effective size for practical scientific experiments.

In this study, the author propose a new high gradient TFM (hereafter referred to as HG-TFM) to realize a quasi-zero gravity environment, in which slit ring bulks are combined with bulk TFM cylinders, and the magnetic properties were investigated in detail during and after magnetization using state-of-the-art numerical simulations. A maximum value of $B_z \cdot dB_z/dz$ = -6040 $T^2$/m was obtained after conventional FCM from $B_{app}$ = 10 T at 40 K for an HG-TFM with 10 mm in inner diameter, which may be the highest value ever reported compared to any other magnetic sources. The mechanical properties of the HG-TFM were also investigated to propose a realistic configuration of the HG-TFM device reinforced by a metal support structure that is essential to prevent mechanical fracture of the bulk superconducting material during the FCM process due to its brittle, ceramic nature.

## 7.2 Numerical modelling procedure

Focusing on magnetic force applications for magnetic levitation [7-9], a higher magnetic field gradient product, $B_z \cdot dB_z/dz$, is desirable in the system as indicated by equation (7-1). The magnetic field gradient ($dB_z/dz$) term should be highly considered, as well as the trapped field ($B_z$) term, to improve the value of $B_z \cdot dB_z/dz$ overall.

Figure 7-1(a) presents a cross-sectional schematic of the three-dimensional numerical model of the HG-TFM, in which a conventional ring-shaped TFM cylinder, labelled "full-TFM", is sandwiched by two TFM cylinders with slits 10 deg. wide in the diagonal direction, labelled "slit-TFM". Figures 7-1(b) and 7-1(c) show the top views of the full-TFM and slit-TFM, respectively. The outer diameter (O.D.) of the HG-TFM is 60 mm and the inner diameter (I.D.) is assumed to be either 10, 20 or 36 mm for both TFM components. The height (H) of the full-TFM is 48 mm, for which three ring-shaped bulks 16 mm in H are stacked, and each of the slit-TFMs are 16 mm in H. In the model, the height of the full-TFM is determined so that the trapped field capability to be 10 T for the HG-TFM with wider I.D. = 36 mm and is fixed temporarily for the comparison with various I.D. cases. The number of layers of the full-TFM can be reduced within the capability required in the device. Each bulk is mounted separately in an Al-alloy ring 5 mm in thickness (O.D. = 70 mm, I.D. = 60 mm, H = 16 mm) adhered by a thin layer of epoxy resin. A thin indium sheet layer (0.1 or 1 mm in thickness) is inserted between each bulk to reproduce the boundary condition between each bulk in the realistic HG-TFM. A solenoid coil of 170 mm in O.D., 120 mm in I.D. and 200 mm in H is used to apply the magnetic field for the magnetization process (not shown in figure 7-1). As described earlier, appropriate mechanical reinforcement must be considered for the bulks due to their brittle, ceramic nature for improving the reliability of the magnetization process and the device itself. Several studies have investigated the fracture behavior of the bulk TFMs, which has a high risk of occurring under FCM from applied fields over 10 T at temperatures lower than 50 K, in particular [10-12]. As shown in figure 7-1(a), the model represents a realistic experimental setup for the mechanical reinforcement of the bulk magnets, which will be performed in the near future, employing outer Al-alloy rings and an outer stainless steel (SS) capsule of 5 mm in thickness that can provide a compressive stress over -100 MPa when cooling from room temperature to the operating temperature to perform FCM. The mechanical reinforcement could endure up to $B_{app}$ = 10 T in actual FCM experiments [13, 14].

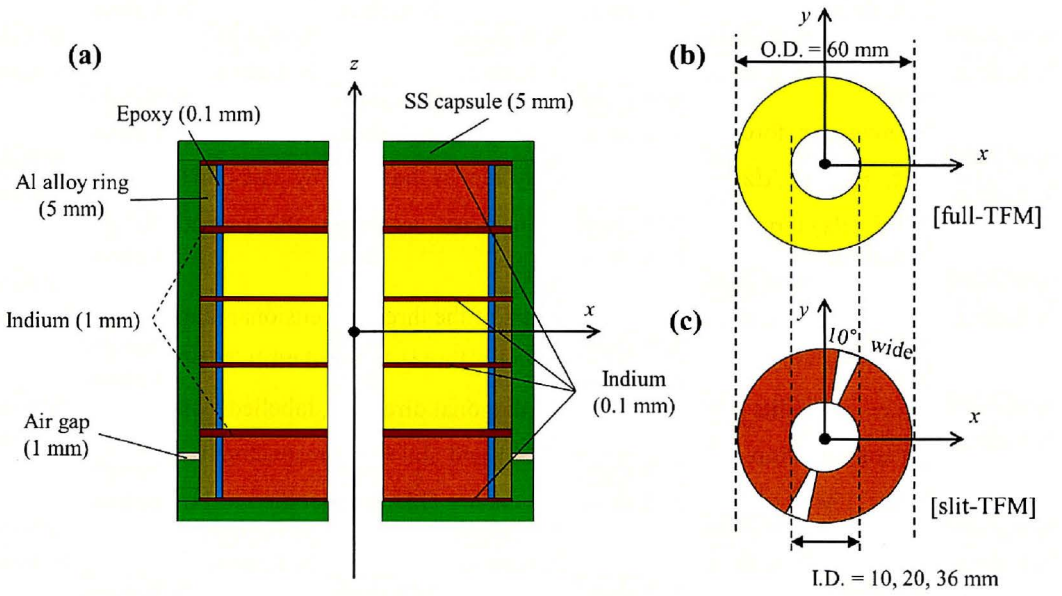


Figure 7-1. (a) Cross-sectional schematic of the three-dimensional numerical model of the HG-TFM, in which a conventional ring-shaped TFM cylinder, labelled "full-TFM" (yellow), is sandwiched by two TFM cylinders with slits 10 deg. wide in the diagonal direction, labelled "slit-TFM" (orange). The top views of the full-TFM and slit-TFM are also shown in (b) and (c), respectively.

Figure 7-2 presents the magnetizing sequence for FCM of the HG-TFM, which is the same as that for a conventional TFM. The external field, $B_{ex}$, is decreased linearly at a ramp rate of -0.222 T/min. from $B_{app}$ = 3, 5 or 10 T at a constant temperature at 40 K. Once the external field is ramped down to 0 T for step 5, the static magnetic field 15 min later (for step 8) is then referred to as the trapped field value, $B_T$. Only the $z$-component is considered for magnetic levitation because gravity acts along the $-z$ direction. The electromagnetic phenomena of the bulk superconductor during the magnetization process are analyzed using the commercial software, Photo-EDDY (Photon Ltd, Japan).

The nonlinear electrical property of the bulk superconductor is derived from the $E$-$J$ power law as follows,

$$E = E_c \left(\frac{J}{J_c}\right)^n, \qquad (7-2)$$

where $E_c = 10^{-4}$ V/m is the characteristic electrical field, $n = 20$ is an appropriate power-law exponent for GdBaCuO bulk, and $J_c$ is the critical current density. The realistic $J_c(B)$ characteristics, including the fish-tail effect under certain magnetic fields, can be represented by the following equation proposed by Jirsa *et al.* [15],

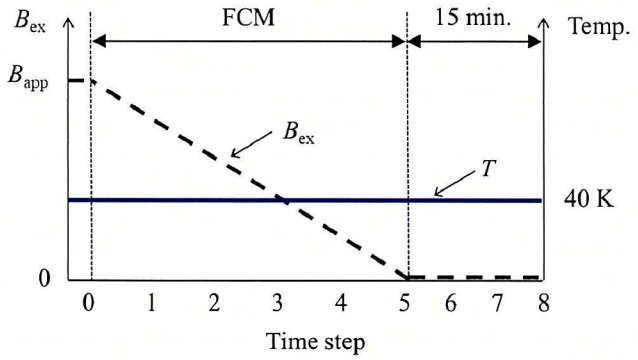


Figure 7-2. Magnetizing sequence for FCM of the HG-TFM, which is the same as that for a conventional TFM. The external field, $B_{ex}$, is decreased linearly at a ramp rate of -0.222 T/min. from $B_{app}$ = 3, 5 or 10 T at a constant temperature at 40 K.

Table 7-1. Numerical fitting parameters for the assumed $J_c(B)$ characteristics of the GdBaCuO bulk used in equation (3), where the $\beta$ value is adjusted to reproduce the experimental result for the trapped field [6].

| $T$ (K) | $J_{c1}$ (A/m$^2$) | $B_L$ (T) | $J_{c2}$ (A/m$^2$) | $B_{max}$ (T) | $\alpha$ | $\beta$ |
|---|---|---|---|---|---|---|
| 40 | 3.5 x $10^9$ | 0.9 | 2.7 × $10^9$ | 6.0 | 0.8 | 0.50 |

$$J_c(B) = \beta \cdot \left\{ J_{c1} \exp\left(-\frac{B}{B_L}\right) + J_{c2} \frac{B}{B_{max}} \exp\left[\frac{1}{\alpha}\left(1 - \left(\frac{B}{B_{max}}\right)^{\alpha}\right)\right]\right\}, \qquad (7-3)$$

where each relevant parameter, $J_{c1}$, $B_L$, $J_{c2}$, $B_{max}$, and $\alpha$ are fitted from the experimental results for a GdBaCuO bulk reported by Kii *et al* [16]. The fitting coefficient, $\beta$, is employed so as to modify the deviation from the actual trapped field value (obtained experimentally) after FCM, particularly at temperatures lower than 50 K [6]. The parameters assumed for the GdBaCuO bulk material for equation (7-3) are summarized in Table 7-1.

## 7.3 Electromagnetic analysis results

Before describing the mechanism of the HG-TFM in detail, the electromagnetic properties of each key component of the HG-TFM – the single full-TFM and the single slit-TFM – were investigated. Figures 7-3(a) and 7-3(b), respectively, show the time step dependence of the magnetic field, $B_z$, during FCM from $B_{app}$ = 3, 5 and 10 T at 40 K at the center of the single full-TFM (I.D. = 10 mm, O.D. = 60 mm, H = 48 mm) and the single slit-TFM (I.D. = 10 mm, O.D. = 60 mm, H = 16 mm, slit 10 deg. wide). For the single full-TFM case shown in figure 7-3(a), the final trapped field, $B_T$, after FCM was almost equivalent to each $B_{app}$ because of partial magnetization within the full capability of the full-TFM, which also enables the generation of a comparatively homogeneous magnetic field inside the bulk bore. Such a high field is realized by an induced supercurrent flowing inside the full-TFM as depicted. Nowadays, it is estimated that the trapped field capability for a disk-shaped bulk pair (O.D. = 24 mm, H = 24 mm) could be over 20 T, based on current state-of-the-art $J_c(B, T)$ characteristics [17]. The schematic view of the magnetic flux distribution and induced current direction in the single full-TFM is shown in figure 7-3(c), in which the conventional magnetic flux lines can be seen.

In the single slit-TFM case shown in figure 7-3(b), when $B_{ex}$ decreased linearly, the $B_z$ steeply decreased and became a negative value. Finally, the $B_z$ value took a negative maximum at step 5 and then slightly recovered to the final $B_T$ value because of the non-linear electrical property of bulk superconductor (see equation (7-2)). At step 8, $B_T$ = -2.8, -3.3, -3.6 T values were obtained at the center of the single slit-TFM for $B_{app}$ = 3, 5 and 10 T, respectively. Figure 7-3(d) also shows the schematic view of the magnetic flux distribution and induced current direction in the single slit-TFM. An induced current flows counterclockwise in each piece separated by the slits, which is the same direction with the full-TFM. However, the downward (-$z$-direction) magnetic flux would penetrate through the slit gap and exist even inside the central bore to build the magnetic loop in each piece of the slit-TFMs, which becomes the opposite direction to that generated by the single full-TFM (+$z$-direction). The HG-TFM then provides a large magnetic field gradient around the interface between the full-TFM with upward magnetic flux lines and the slit-TFM with downward magnetic flux lines.

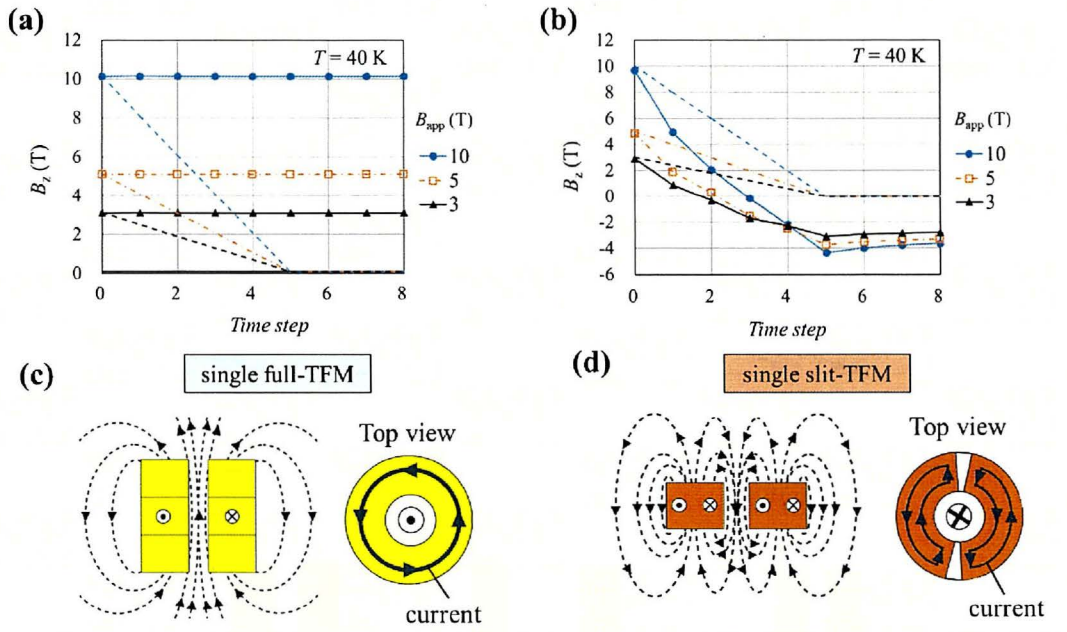


Figure 7-3. The time step dependence of the magnetic field, $B_z$, during FCM from $B_{app}$ = 3, 5 and 10 T at 40 K at the center of (a) the single full-TFM (I.D. = 10 mm, O.D. = 60 mm, H = 48 mm) and (b) the single slit-TFM (I.D. = 10 mm, O.D. = 60 mm, H = 16 mm, slit 10 deg. wide). The schematic view of the magnetic flux distribution and induced current direction in (c) the single full-TFM and (d) the single slit-TFM.

Figures 7-4(a) and 4(b), respectively, show a comparison of the numerical results for the magnetic field, $B_z$, and the magnetic field gradient product, $B_z \cdot dB_z/dz$, after magnetization with $B_{app}$ = 10 T at 40 K along the $z$-axis inside the bulk annuli, comparing three types of TFMs: the HG-TFM, the HTFML and a conventional ring-shaped TFM (single full-TFM). The dimensions of each TFM are shown in the figure, where the dimensions of the full-TFM part were assumed to be identical for each case (I.D. = 10 mm, O.D. = 60 mm, H = 48 mm). The dimensions of the magnetic lens for the HTFML can be referred to elsewhere [6]. In figure 7-4(a), the trapped field, $B_z$, at the center ($z$ = 0 mm) of the HG-TFM and full-TFM should be comparable with the applied field of $B_{app}$ = 10 T. On the other hand, for the HTFML exploiting the diamagnetic lens effect, $B_z$ can be concentrated into the bulk annuli, in which a concentrated trapped field of $B_c$ = 11.0 T was achieved at 40 K at $z$ = 0 mm. In figure 4(b), the HG-TFM shows the highest $B_z \cdot dB_z/dz$ value of -6040 $T^2$/m at the boundary between each TFM part, $z$ = 24 mm, which is remarkably superior than the other two types of TFM. In this sense, to improve the magnetic force efficiently, it would be more desirable to control the magnetic field gradient ($dB_z/dz$) profile by focusing on the gradient itself rather than improving the trapped field ($B_z$). One significant advantage of the HG-TFM is that its superior magnetic properties could be

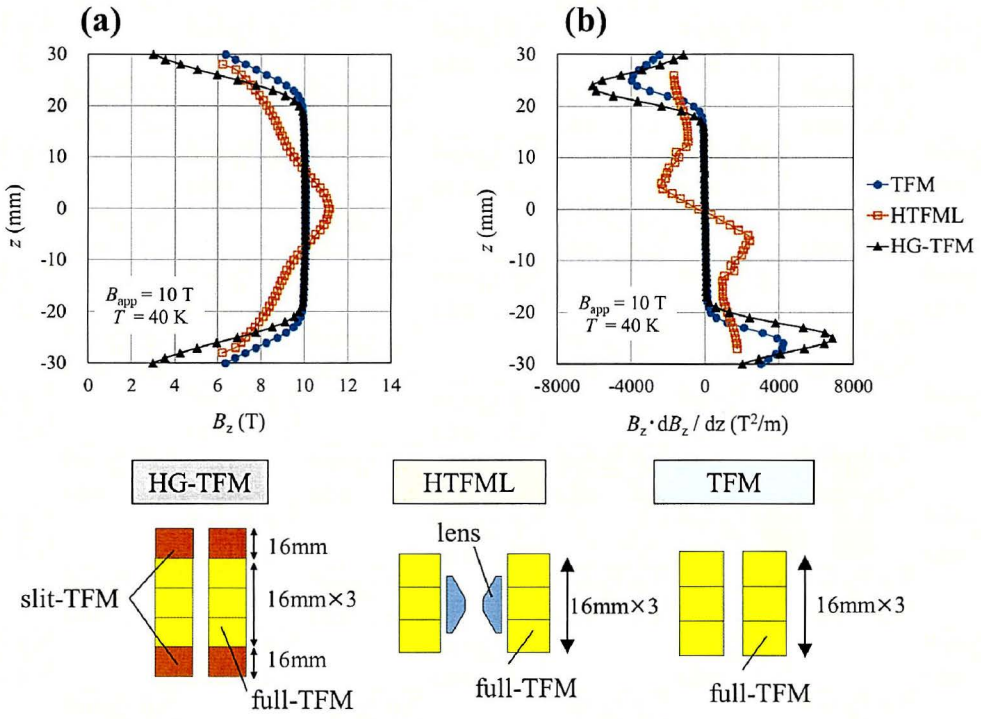


Figure 7-4. Numerical results for (a) the magnetic field, $B_z$, and (b) the magnetic field gradient product, $B_z \cdot dB_z/dz$, after magnetization with $B_{app}$ = 10 T at 40 K along the $z$-axis inside the bulk annuli, comparing three types of TFMs: the HG-TFM, the HTFML and a conventional ring-shaped TFM (single full-TFM).

realized using a conventional FCM process at one temperature and without any additional costs, except for the slit-TFM. Note again that figure 7-4 is an example assuming a narrow 10 mm bore in inner diameter for each system. The magnetic properties of the HG-TFM would change depending on the shape of the bulk material (O.D., I.D., H, slit angle and so on) and the conditions of the magnetization process, such as the magnetizing temperature and $B_{app}$.

Figures 7-5(a) and 7-5(b), respectively, show the magnetic field, $B_z$, and the magnetic field gradient product, $B_z \cdot dB_z/dz$, profiles of the HG-TFM with inner bores of I.D. = 10, 20 and 36 mm along the $z$-direction inside the bulk bore after FCM from $B_{app}$ = 10 T at 40 K, compared with those of a single full-TFM (-24 mm $\leq z \leq$ 24 mm) and single slit-TFM pair ($\pm z$ = 25 ~ 41 mm). In figure 7-5(a), the slit-TFM pair with a narrower bore of I.D. = 10 mm generates a higher negative trapped field (= -3 T) over a wider area at $\pm z$ = 20 ~ 40 mm, which is effective for improving the HG-TFM performance with a larger magnetic field gradient. The negative trapped field of the single slit-TFM pair decreased with increasing I.D. value and there is no remarkable negative value for I.D. = 36 mm. On the other hand, for the cases of the full-TFM and HG-TFM, the $B_z$ profile becomes broad with increasing I.D. value and the shape of the trapped field profile no longer varies between the full-TFM and HG-TFM

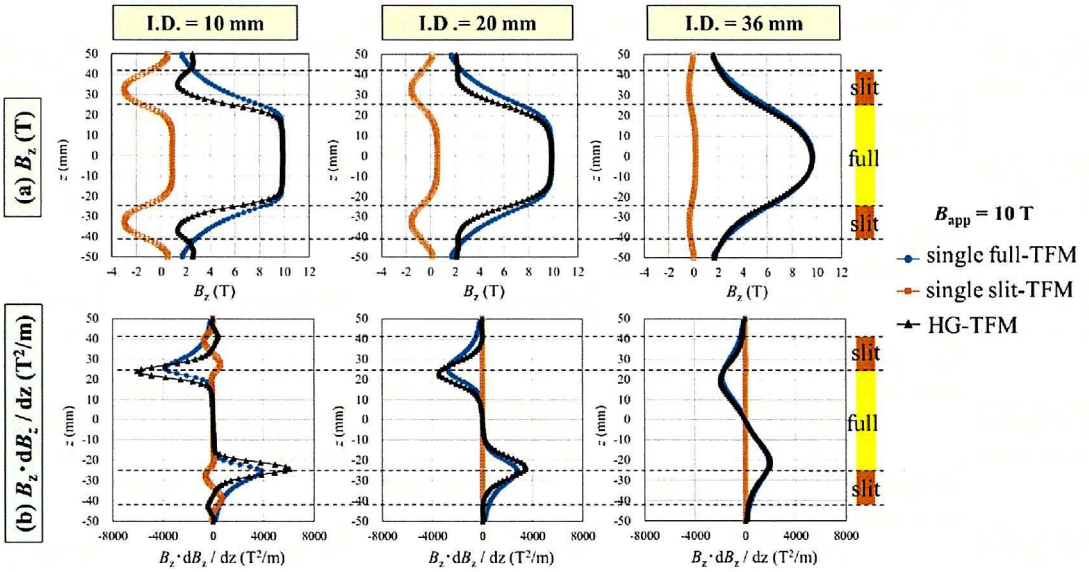


Figure 7-5. (a) The magnetic field, $B_z$, and (b) the magnetic field gradient product, $B_z \cdot dB_z/dz$, profiles of the HG-TFM with inner bores of I.D. = 10, 20 and 36 mm along the $z$-direction inside the bulk bore after FCM from $B_{app}$ = 10 T at 40 K, compared with those of a single full-TFM (-24 mm $\leq z \leq$ 24 mm) and single slit-TFM pair ($\pm z$ = 25 ~ 41 mm).

with I.D. = 36 mm. Since $B_z$ decays significantly with distance outside of the TFM, *i.e.*, at $\pm z \geq 24$ mm, there is less, or no magnetic flux controlled in the HG-TFM with wider I.D. = 36 mm.

In figure 7-5(b), for the HG-TFM, the peak value of $B_z \cdot dB_z/dz$ was enhanced with decreasing I.D. at the boundary position between each TFM around $\pm z$ = 24 mm due to the presence of the slit-TFM. A maximum $B_z \cdot dB_z/dz$ value of 6040 T²/m was achieved for I.D. = 10 mm, which is larger than that for the full-TFM (-3790 T²/m). It should be noted that a $B_z \cdot dB_z/dz$ value as large as -1400 T²/m along the +$z$-direction of the vertical magnet is required to levitate a diamagnetic water drop in air [18]. In this sense, the effective volume for magnetic levitation can be estimated to be $+z$ = 19 ~ 30, 17 ~ 30 and 13 ~ 27 mm inside the bore of the HG-TFM with I.D. = 10, 20 and 36 mm, respectively. For protein crystallization in a diamagnetic solution, a larger $B_z \cdot dB_z/dz$ value of -4450 T²/m is required to realize an apparent zero-gravity condition without buoyancy flow, which is much higher than that estimated numerically [19]. For realizing a higher field gradient product, the HG-TFM with a narrower inner bore is desirable, leading to a trade-off between field gradient product and effective volume.

Figures 7-6(a) and 7-6(b) summarize the final trapped field, $B_T$ (= $B_z$ at step 8), at the center ($x = y = z = 0$) and the maximum field gradient product, $|B_z \cdot dB_z/dz|$, around the boundary position between the full and slit-TFMs of the HG-TFM, as a function of $B_{app}$ for various I.D. cases. The results for the full-TFM cases are also shown for reference. In figure 6(a), the trapped field capability is equivalent for all cases; thus, the relation $B_T = B_{app}$, is established based on the typical FCM process.

However, for the magnetic field gradient product shown in figure 7-6 (b), the HG-TFM would work more effectively for $B_{app}$ higher than 5 T and for narrower bores smaller than I.D. = 20 mm compared to the full-TFM. Table 7-2 summarizes the maxima of the magnetic properties for each case including the HG-TFM, HTFML and full-TFM, extracted from figures 7-4 and 7-6. The HG-TFM with I.D. = 10 mm would provide a maximum $|B_z \cdot dB_z/dz|$ = 6040 T/m$^2$ when $B_T$ = 10 T at 40 K, which may be the record-high value compared to that of other large-scale magnets: superconducting magnets (SM) ~1500 T/m$^2$, and hybrid-type superconducting magnets (HM) ~3000 T/m$^2$ using liquid helium, shown in figure 7-6(b) [4, 20].

In most related studies, based on apparatus using a permanent magnet with a magnetic field ~ 1 T, the magneto-Archimedes method must be exploited to reduce the required magnetic force using a paramagnetic medium solution [21, 22]. The HG-TFM no longer needs such a method, and consequently, can provide simpler, medium-free operation with air or water. These advantages of the HG-TFM can provide the versatility of a quasi-zero gravity space as a desktop-type magnetic source for magnetic levitation processing, which enables the suppression of gravity-induced convection in a wide range of potential industrial applications such as protein crystallization and cell culture [1, 2]. It should be noted that $B_z \cdot dB_z/dz$ values of 1980 and 2760 T$^2$/m can be achieved after FCM from $B_{app}$ = 10 T even for the single full-TFM with I.D. = 36 and 20 mm (without the slit-TFM), respectively, as shown in Table 7-2, which are higher than that achieved by SMs [4]. These results suggest that the single full-TFM can be also applicable for quasi-zero gravity in the open space outside the vacuum chamber with a range of 15-30 mm in diameter. There is a limit for the enlargement of the space in the bore because it is difficult to fabricate good quality bulks > 60 mm in O.D., resulting in a narrower bore compared to that of SMs.

In our previous work [6], where the mechanism of magnetic levitation in the quasi-zero gravity space is explained in detail, it was highlighted that a large magnetic field gradient product up to 3000 T$^2$/m of that particular HTFML design could be highly applicable to magnetic separation. Regarding the effectiveness of the magnetic force for crystal growth, it is shown elsewhere that the magnetic force affects several features: the magnetic field orientation, convection control, reduction of sedimentation and so on [7]. However, there are no theoretical rules yet regarding how the magnetic force works during the process and it differs between the target materials used. Thus, appropriate design of the I.D. of the HG-TFM needs to be explored as related to the particular application, where the magnetic force profile in the HG-TFM could be correlated with the quality of the resultant crystallization.

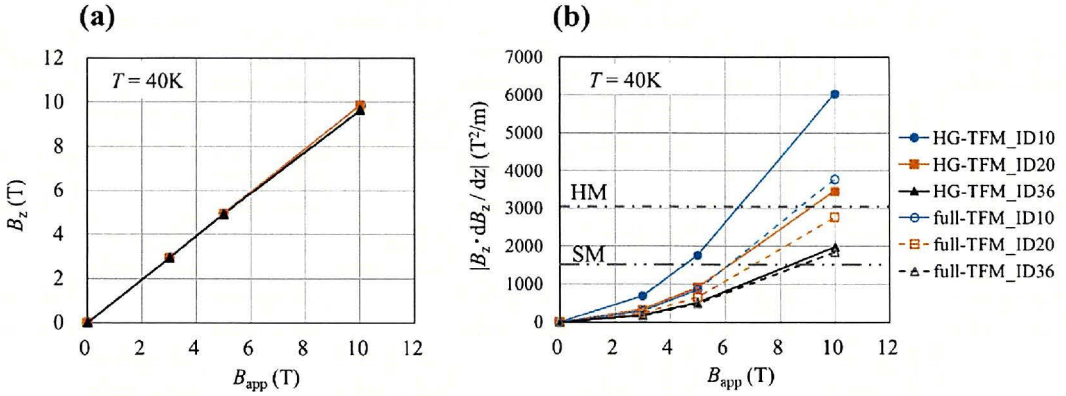


Figure 7-6. (a) The final trapped field, $B_T$ (= $B_z$ at step 8), at the center ($x = y = z = 0$) and (b) the maximum field gradient product, $|B_z \cdot dB_z/dz|$, at the boundary position between the full and slit-TFMs of the HG-TFM, as a function of $B_{app}$ for various I.D. cases. The results are compared to that of the full-TFM cases and other large-scale magnets: superconducting magnets (SM), and hybrid-type superconducting magnets (HM).

Table 7-2. Numerical results of maxima of the magnetic properties for each case including the HG-TFM, HTFML and full-TFM magnetized at 40 K, extracted from figures 7-4 and 7-6.

| | HG-TFM | | | HTFML |
|---|---|---|---|---|
| Bulk I.D. (mm) | 10 | 20 | 36 | 10 |
| $B_z$ ($B_{app}$) (T) | 10 (10) | 10 (10) | 9.8 (10) | 11 (10) |
| $\lvert B_z \cdot dB_z/dz \rvert$ (T²/m) | 6040 | 3460 | 1980 | 2430 |
| (single full-TFM) | (3790) | (2760) | (1850) | (1850) |
| Magnetization | | FCM | | ZFCM+FCM |
| Temperature (K) | | | 40 | |

## 7.4 Mechanical stress analysis results

The mechanical fracture of bulk superconductors has been reported in several studies, where a crack might occur along the circumferential direction mainly due to the hoop stress induced during FCM from applied fields over 10 T at temperatures below 50 K. [10-12]. To date, to prevent such mechanical fracture during magnetization, mechanical reinforcement has been usefully applied using glass fiber reinforced epoxy resin [23] or shrink-fit steel [24]. Author's group also proposed a new hat structure of an outer metal reinforcement ring based on the results of mechanical stress simulations, in which a large (RE)BaCuO ring-shaped bulk (I.D. = 36 mm, O.D. = 60 mm, H = 20 mm) was experimentally confirmed to endure FCM from 10 T without fracture [13]. For the HTFML consisting of a (RE)BaCuO lens and (RE)BaCuO TFM cylinder, the mechanical properties have been analyzed during the magnetizing process from $B_{app}$ = 10 T [25], in which the necessity of adequate mechanical reinforcement was strongly suggested, at least for the GdBaCuO TFM cylinder, but possibly the magnetic lens as well. It is also necessary to investigate the mechanical properties of the present HG-TFM as well during FCM, where the full-TFM part is tightly sandwiched by the slit-TFM pair.

After calculating the trapped field profile shown in the previous section, the nodal force was then imported into another software package, Photo-ELAS (Photon Ltd, Japan), for calculating the electromagnetic stress on each mesh element of the bulk TFMs during magnetization, which enables us to assess the reliability of the HG-TFM in terms of the mechanical reinforcement method.

Elastic behavior in an isotropic material can be expressed by Hooke's law, in which the stress tensor, $\sigma_{ij}$, is linearly proportional to the strain tensor, $\varepsilon_{ij}$, as follows

$$\sigma_{ij} = \lambda \cdot \varepsilon_{kk} \cdot \delta_{ij} + 2G \cdot \varepsilon_{ij}, \tag{7-4}$$

$$\lambda = \frac{E \cdot \nu}{(1+\nu)(1-2\nu)}, \tag{7-5}$$

$$G = \frac{E}{2(1+\nu)}, \tag{7-6}$$

where $\lambda$ and $G$ represent Lame's constants, $\delta_{ij}$ is the Kronecker delta function, $E_Y$ is the Young's modulus, and $\nu$ is the Poisson ratio. The mechanical parameters, $E_Y$ and $\nu$, for each component of the HG-TFM are summarized in Table 7-3, which are assumed in the simulation to be isotropic and in the elastic region. Note that all components, including the epoxy resin, indium and air gap, as shown in figure 7-1, were included in the modelling of the HG-TFM, which should be considered for the accurate prediction of the mechanical behavior [26].

Table 7-3. Assumed mechanical parameters ($E_Y$ :Young's modulus and $v$: Poisson ratio) for numerical stress analysis of the HG-TFM shown in figure 7-1 [13, 26].

| | $E_Y$ (GPa) | $v$ |
|---|---|---|
| (RE)BaCuO bulk | 100 | 0.33 |
| Epoxy resin | 3.0 | 0.37 |
| Al alloy (A7075-T6) | 78 | 0.34 |
| Indium | 12.7 | 0.45 |
| SS 304 | 193 | 0.28 |

Figures 7-7(a) and 7-7(b) show a contour map of the Von Mises stress, $\sigma_{VM}$, and the electromagnetic hoop stress along the $y$-direction, $\sigma_{YY}$, respectively, calculated for the full-TFM part of the HG-TFM with inner diameters of I.D. = 10, 20 and 36 mm, just after FCM from 10 T (step 5). In figure 7(a), the $\sigma_{VM}$ value, which is a scalar quantity, represents the total value of the mechanical stresses including all directions. Compared with the maximum $\sigma_{YY}$ value shown in figure 7-7(b), which is close to the maximum $\sigma_{VM}$ value of 90 MPa around the inner periphery of the full-TFM part, it was found that the main component of the electromagnetic stress results from the hoop stress along the $y$-direction in the full-TFM part. The maximum $\sigma_{YY}$ value was almost independent of the bore size because the trapped field is equivalent for each HG-TFM with different bore sizes as shown in figure 7-6(a). These numerical results for the stress profile are similar to that reported for the annular (RE)BaCuO bulk magnet system (full-TFM) for an NMR spectrometer [14], in which an electromagnetic hoop stress about 100 MPa was generated at the inner peripheral region of the annular bulks reinforced by a similar structure. This means that the present reinforcement technique would work even for the present HG-TFM system. Considering the compressive stress of -100 MPa from the reinforcement by the Al-alloy rings and the SS capsule during the cooling process before FCM, the maximum total stress would be less than the fracture strength of typical Ag-doped (RE)BaCuO bulks of 50 - 70 MPa [27]. As a result, the full-TFM part should be appropriately reinforced and not break (see ref. 21).

Figures 7-8(a) to 7-8(c) show the contour map of the Von Mises stress, $\sigma_{VM}$, the electromagnetic hoop stress along the $y$-direction, $\sigma_{YY}$, and the electromagnetic radial stress along the $x$-direction, $\sigma_{XX}$, respectively, for the slit-TFM pair of the HG-TFM with inner diameters of I.D. = 10, 20 and 36 mm, just after FCM from 10 T. For the case of I.D. = 10 mm, a maximum Von Mises stress of $\sigma_{VM}$ = 54 MPa exists at the surfaces of the slit-TFM pair facing the full-TFM part. The $\sigma_{XX}$ profile for each I.D., as shown in figure 7-8(c), is similar to that for $\sigma_{VM}$. On the other hand, the $\sigma_{YY}$ contribution to the Von Mises stress, as shown in figure 8(b), is relatively small. These results suggest that the main component of the electromagnetic stress results from the electromagnetic radial stress along the $x$-

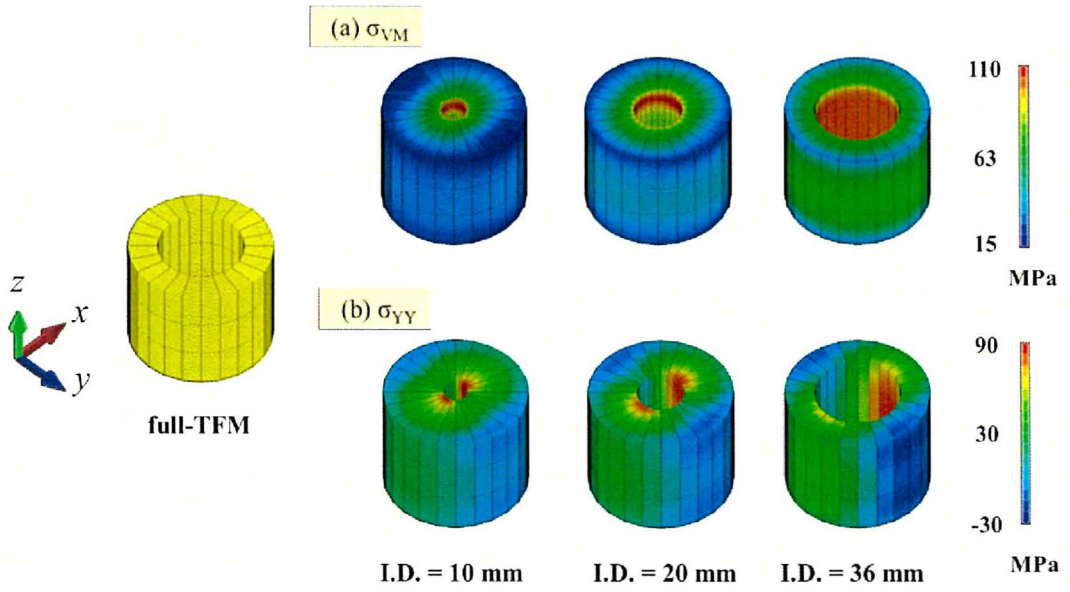


Figure 7-7. Contour map of (a) the Von Mises stress, $\sigma_{VM}$, and (b) the electromagnetic hoop stress along the $y$-direction, $\sigma_{YY}$, calculated for the full-TFM part of the HG-TFM with inner diameters of I.D. = 10, 20 and 36 mm, at step 5 just after FCM from 10 T.

direction, $\sigma_{XX}$, in the case of I.D. = 10 mm and I.D. = 20 mm. However, for the wider I.D. = 36 mm, the electromagnetic stress mainly results from the hoop stress along the $y$-direction, $\sigma_{YY}$. Since an induced current flows in two regions in the slit-TFM independently due to the existence of slits, the resultant trapped field and the mechanical stress become lower, compared to the full-TFM, even if the slit-TFM is magnetized by FCM from 10 T.

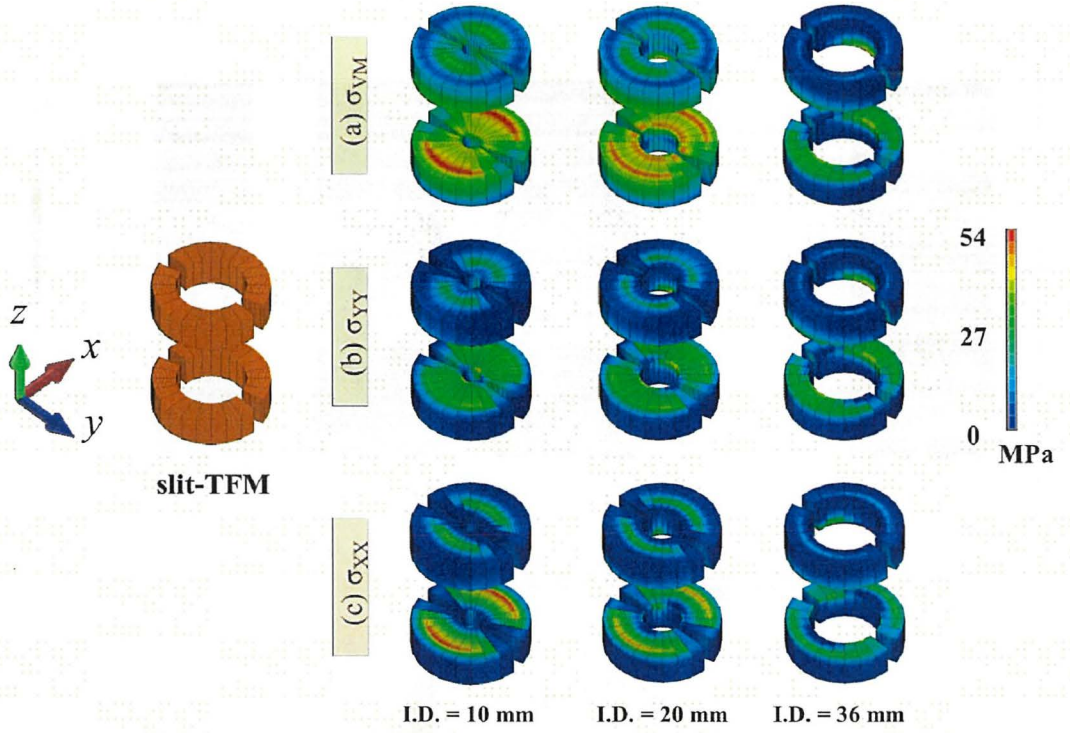


Figure 7-8. Contour map of (a) the Von Mises stress, $\sigma_{VM}$, (b) the electromagnetic hoop stress along the $y$-direction, $\sigma_{YY}$, and (c) the electromagnetic radial stress along the $x$-direction, $\sigma_{XX}$, for the slit-TFM pair of the HG-TFM with inner diameters of I.D. = 10, 20 and 36 mm, just after FCM from 10 T.

During the magnetization of the HG-TFM exploiting slit-TFMs stacked on the full-TFM, an extra stress component may be generated due to the repulsive force between each TFM part. Figure 7-9(a) shows a cross-sectional contour map of the electromagnetic stress along the vertical direction, $\sigma_{ZZ}$, for the HG-TFM with various inner diameters, just after the FCM process from 10 T. The positive $\sigma_{ZZ}$ value is concentrated mainly in the inner periphery of the slit-TFM facing the full-TFM, and the magnitude of $\sigma_{ZZ}$ increases with increasing I.D. These results suggest that a repulsive force exists in this region. However, the positive $\sigma_{ZZ}$ region vanishes at the outer interface of the slit-TFM facing the full-TFM ($z = \pm 24$ mm, $-15 \leq x \leq 30$ mm for I.D. = 36 mm case), which indicates the possibility of an attractive force or very small repulsive force there. Figure 7-9(b) shows the $\sigma_{ZZ}$ distribution along the $z$-direction at the inner periphery ($x$ = 18 mm) and at the outer periphery ($x$ = 30 mm) for the HG-TFM with I.D. = 36 mm, which were extracted from figure 7-9(a). At the inner periphery, the $\sigma_{ZZ}$ value changes from positive to negative around the interface ($z = \pm 24$ mm). These results indicate that a repulsive force exists at the inner interface. On the other hand, at the outer periphery, the $\sigma_{ZZ}$ value is negative and continuous for both the slit-TFM and full-TFM, suggesting that an attractive magnetic force might exist at the outer interface. Similar trends were also observed for the HG-TFM

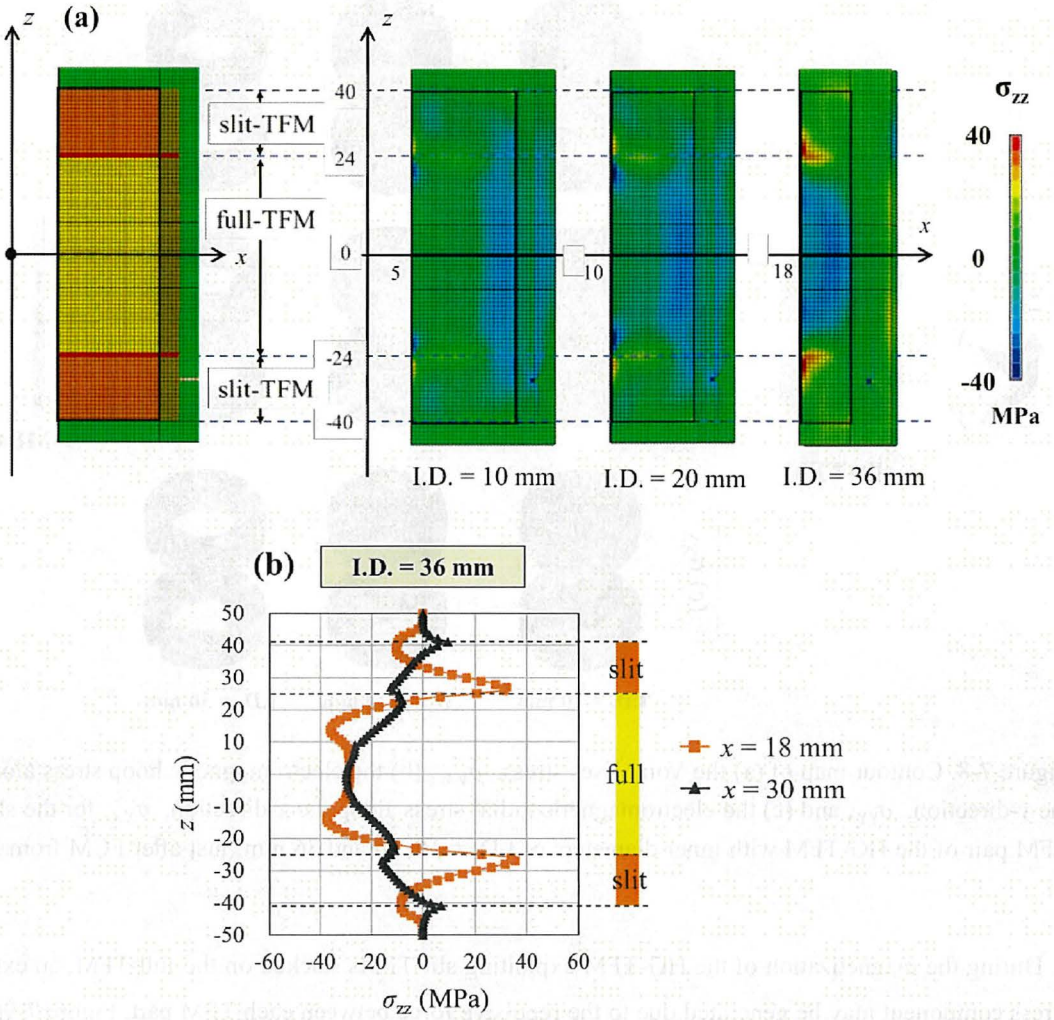


Figure 7-9. (a) Cross-sectional contour map of the electromagnetic stress along the vertical direction, $\sigma_{ZZ}$, for the HG-TFM with various inner diameters, just after the FCM process from 10 T. (b) The $\sigma_{ZZ}$ distribution along the $z$-direction at the inner periphery ($x$ = 18 mm) and at the outer periphery ($x$ = 30 mm) for the HG-TFM with I.D. = 36 mm, extracted from (a).

for I.D.s = 10 and 20 mm.

Figure 7-10(a) shows a schematic view of the magnetic flux profile for the HG-TFM after FCM. To understand the distribution of the magnetic flux lines at the interface visually, the full-TFM and the slit-TFM pair are placed at a distance. It can be confirmed visually that the magnetic flux lines co-exist at the interface and form the superposition of the magnetic fields that is destructive around the central bore or constructive around the bulk periphery.

Figure 7-10(b) shows a contour map of the final trapped field, $B_T$, of the HG-TFM with I.D. = 20 mm after FCM from 10 T. It should be noted that a trapped field along the +$z$-direction exists at the periphery of the slit-TFM (region A), which has a similar $B_T$ strength of 10 T as for the full-TFM.

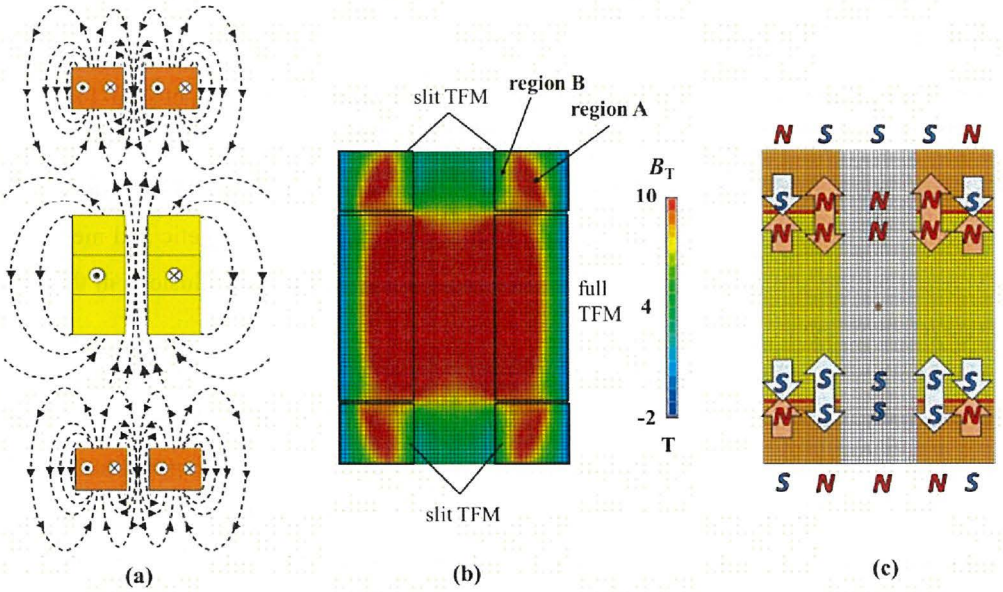


Figure 7-10. (a) Schematic view of the magnetic flux profile for the HG-TFM after FCM. (b) Contour map of the final trapped field, $B_T$, of the HG-TFM with I.D. = 20 mm after FCM from 10 T. (c) The effective magnetic poles of the HG-TFM after FCM. The outer periphery region (region A) and inner periphery region (region B) of the slit-TFM can be considered as opposing magnetic poles.

These results suggest that "region A" is magnetically attracted to the magnetized full-TFM. On the other hand, there exists little field trapped downward along the $z$-direction in the inner periphery region of the slit-TFM ("region B"). These results indicate that a repulsive magnetic force exists in the counter side in the full-TFM, which can be understood well from the schematic view of the magnetic flux lines in figure 7-10(a).

Let us describe these results using a magnetic pole model. Figure 7-10(c) shows the effective magnetic poles of the HG-TFM after FCM, which presents the mechanism of the larger magnetic gradient of the HG-TFM. The outer periphery region (region A) and inner periphery region (region B) of the slit-TFM can be considered as opposing magnetic poles. As a result, region A is attractive (an N-S or S-N pair) and region B is repulsive (N-N or S-S pair) with respect to the magnetized full-TFM at the interface. Since both TFM parts are mounted in an Al-alloy ring and the whole HG-TFM is encapsulated in an SS capsule, $\sigma_{ZZ}$ acts as a compressive stress, and that maxima is around 50 MPa for the full-TFM and 35 MPa for slit-TFM in the HG-TFM with I.D. = 36 mm. However, in the narrower bore cases, I.D. = 10 and 20 mm, $\sigma_{ZZ}$, decreases despite the superior $B_z \cdot dB_z/dz$ performance. In any case, there is little fracture risk due to the compressive stress for the HG-TFM during FCM from 10 T, since the compressive fracture strength of (RE)BaCuO bulk is about one order of magnitude higher than the tensile mechanical strength [28].

## 7.5 Summary of Chapter 7

The author has proposed a new concept of a High Gradient Trapped Field Magnet (HG-TFM). The HG-TFM is made from (RE)BaCuO bulk superconductors to realize a quasi-zero gravity space using magnetic force, in which a slit ring bulk (slit-TFM) was tightly stacked with a TFM cylinder (full-TFM). State-of-the-art numerical simulations were used to investigate the magnetic and mechanical properties detail during and after magnetization. The important results and conclusions in this study are summarized as follows.

1) A maximum value of the magnetic field gradient product of $B_z \cdot dB_z/dz$ = -6040 $T^2$/m was obtained after conventional FCM from $B_{app}$ = 10 T of the HG-TFM with a 60 mm outer diameter and 10 mm inner diameter. This value may be the highest ever reported compared to any other magnetic sources. The superiority of the HG-TFM is the easier magnetization process including a single temperature and a simpler construction without any additional cost, but also the higher $B_z \cdot dB_z/dz$ can be provided in an open space outside the vacuum chamber.
2) The $B_z \cdot dB_z/dz$ value increased with decreasing inner diameter of the HG-TFM and with increasing applied field, $B_{app}$, during FCM. Even if the inner diameter of the HG-TFM is 36 mm, a $B_z \cdot dB_z/dz$ value of 1980 $T^2$/m can be achieved, which is slightly higher than 1850 $T^2$/m for the single full-TFM case.
3) The electromagnetic stress during the FCM process was also investigated to analyze the mechanical behavior of HG-TFM device. The electromagnetic stress in the HG-TFM device during the FCM process mainly results from the hoop stress along the $y$-direction, $\sigma_{YY}$, for the full-TFM.
4) The outer and inner periphery regions of the slit-TFM can be considered as opposing magnetic poles. The outer periphery region is attractive (N-S or S-N pair) and the inner periphery region is repulsive (N-N or S-S pair) with respect to the magnetized full-TFM at the interface. However, it was confirmed that there is little fracture risk for the bulks during FCM from 10 T in the proposed realistic configuration of the HG-TFM, where both TFM parts are mounted in Al-alloy rings and the whole HG-TFM is encapsulated in an SS capsule.
5) A quasi-zero gravity space can be realized using the HG-TFM with its large $B_z \cdot dB_z/dz$ value in an open space outside the vacuum chamber even without the magneto-Archimedes method. The HG-TFM device is a compact and cryogen-free desktop-type magnetic source to provide a large magnetic force and can be applicable to scientific research, such as in the life/medical sciences for protein crystallization and cell culture.

## 7.6 References


[1] McPherson A and DeLucas L J 2015 Microgravity protein crystallization *NPJ. Microgravity* **1** 15010.

[2] Imura T, Nakagawa K, Kawahara Y and Yuge L 2018 Stem cell culture in microgravity and its application in cell-based therapy *Stem Cells Dev.* **27** 1298-1302.

[3] Beaugnon E and Tournier R 2003 Levitation of organic materials *Nature* **349** 470.

[4] Nikolayev V S, Chatain D, Beysens D and Pichavant G 2011 Magnetic gravity compensation *Microgravity. Sci. Technol.* **23** 113-122.

[5] Wada H *et al* 2012 Application of High-Field Superconducting Magnet to Protein Crystallization *Phys. Procedia Technol.* **36** 953-957.

[6] Takahashi K, Fujishiro H and Ainslie M D 2020 Simulation study for magnetic levitation in pure water exploiting the ultra-high magnetic field gradient product of a hybrid trapped field magnet lens (HTFML) *J. Appl. Phys.* **127** 185106.

[7] Yin D-C 2015 Protein crystallization in a magnetic field *Prog. Cryst. Growth Chract. Mater.* **61** 1-26.

[8] Kobayashi T, Mori T, Akiyama Y, Mishima F and Nishijima S 2017 Study on Separation of Structural Isomer with Magneto-Archimedes method *J. Phys.: Conf. Ser.* **897** 012018.

[9] Miura O, Yamagishi K and Yamamoto D 2018 Magneto-Archimedes levitation of precious metals under a high magnetic field gradient *J. Phys.: Conf. Ser.* **1054** 012086.

[10] Ren Y, Weinstein R, Liu J, Sawh R P and Foster C 1995 Damage caused by magnetic pressure at high trapped field in quasi-permanent magnets composed of melt-textured Y-Ba-Cu-O superconductor *Physica C* **251** 15-26.

[11] Yanagi Y, Yoshikawa M, Itoh Y, Oka T, Ikuta H and Mizutani U 2004 Generation of extremely strong magnetic fields in open space by using metal-ring-reinforced 60 mmφ Sm-Ba-Cu-O superconducting bulk *Physica C* **412-414** 744-749.

[12] Miyamoto T, Nagashima K, Sakai N and Murakami M 2000 Direct measurements of mechanical properties for large-grain bulk superconductors *Physica C* **340** 41-50.

[13] Fujishiro H, Naito T, Yanagi Y, Itoh Y and Nakamura T 2019 Promising effects of a new *hat structure* and double metal ring for mechanical reinforcement of a REBaCuO ring-shaped bulk during field-cooled magnetization at 10T without fracture *Supercond. Sci. Technol.* **32** 065001.

[14] Fujishiro H, Takahashi K, Naito T, Yanagi Y, Itoh Y and Nakamura T 2018 New proposal of mechanical reinforcement structures to annular REBaCuO bulk magnet for compact and cryogen-free NMR spectrometer *Physica C* **550** 52-56.

[15] Jirsa M, Půst L, Dlouhý D and Koblischka M R 1997 Fishtail shape in the magnetic hysteresis loop for superconductors: Interplay between different pinning mechanisms *Phys. Rev. B* **55** 3276–

3284.

[16] Kii T *et al* 2012 Low-Temperature Operation of a Bulk HTSC Staggered Array Undulator *IEEE Trans. Appl. Supercond.* **22** 4100904.

[17] Huang K *et al* 2020 Composite stacks for reliable >17 T trapped fields in bulk superconductor magnets *Supercond. Sci. Technol.* **33** 02LT01.

[18] Ikezoe Y, Kaihatsu T, Sakae D, Uetake H, Hirota N and Kitazawa K 2002 Separation of feeble magnetic particles with magneto-Archimedes levitation *Energ. Convers. Manage.* **43** 417-425.

[19] Ramachandran N and Leslie F W 2005 Using magnetic fields to control convection during protein crystallization-analysis and validation studies *J. Cryst. Growth* **274** 297-306.

[20] Yan E-K, Zhang C-Y, He J and Yin D-C 2016 An Overview of Hardware for Protein Crystallization in a Magnetic Field *Int. J. Mol. Sci.* **17** 1906.

[21] Zhao P, Xie J, Gu F, Sharmin N, Hall P and Fu J 2018 Separation of mixed waste plastics via magnetic levitation *Waste Manag.* **76** 46-54.

[22] Mirica K A, Shevkoplyas S S, Phillips S T, Gupta M and Whitesides G M 2009 Measuring Densities of Solids and Liquids Using Magnetic Levitation: Fundamentals *J. Am. Chem. Soc.* **131** 10049-10058.

[23] Tomita M and Murakami M 2003 High-temperature superconductor bulk magnets that can trap magnetic fields of over 17 tesla at 29 K *Nature* **421** 517-520.

[24] Durrell J H *et al* 2014 A trapped field of 17.6 T in melt-processed, bulk Gd-Ba-Cu-O reinforced with shrink-fit steel *Supercond. Sci. Technol.* **27** 082001.

[25] Namba S, Fujishiro H, Ainslie M D, Takahashi K, Namburi D K, Zhou D and Naito T 2019 Design Optimization of a Hybrid Trapped Field Magnet Lens (HTFML) *IEEE Trans. Appl. Supercond.* **29** 6801605.

[26] Namba S, Fujishiro H, Naito T, Ainslie M D and Huang K Y 2019 Electromagnetic strain measurements and two-directional mechanical stress estimation for a REBaCuO ring bulk reinforced by a metal ring during field-cooled magnetization *Supercond. Sci. Technol.* **32** 125001.

[27] Katagiri K, Murakami A, Shoji Y, Teshima H, Sawamura M, Iwamoto A, Mito T and Murakami M 2004 Tensile and bending mechanical properties of bulk superconductors at room temperature *Physica C* **412-414** 633-637.

[28] Kan R, Katagiri K, Murakami A, Kasaba K, Shoji Y, Noto K, Sakai N and Murakami M 2004 Deformation and Fracture Behavior of Sm123 Bulk Superconductors by Compressive Loading at Room Temperature *IEEE Trans. Appl. Supercond.* **14** 1114-1117.

# Chapter 8

# Conclusion

This Ph.D. thesis summarized the development progress of a hybrid-type, superconducting bulk magnets, which is superior to the magnetic properties as well as the versatility, as a compact desktop-type, magnetic field source. A conceptual numerical study of the HTFML has been verified experimentally for two cases: Case-1: using outer $MgB_2$ cylinder and inner GdBaCuO magnetic lens, and Case-2: using all-REBaCuO system. Furthermore, a new concept of a HG-TFM was proposed for realizing the quasi-zero gravity environment on the earth for the potential application such as protein crystallization and cell culture. The important prospects of the development are reviewed, periodically for each chapter in the following.

## Chapter 2: A new concept of a hybrid trapped field magnet lens

A new concept of a "hybrid trapped field magnet lens (HTFML)," consisting of a superconducting bulk cylinder TFM using the "vortex pinning effect," combined with a bulk magnetic lens using the "diamagnetic shielding effect," can reliably generate a magnetic field at the center of the magnetic lens higher than the trapped field by TFM and the maximum external magnetizing field, even after the externally applied field decreases to zero. The proposed magnetizing sequence was tested using numerical simulations for two examples: 1) an $MgB_2$ cylinder and GdBaCuO lens pair ("case-1") and 2) a GdBaCuO cylinder and GdBaCuO lens pair ("case-2"). In "case-1," using the outer $MgB_2$ cylinder and inner GdBaCuO lens pair, the $MgB_2$ cylinder was magnetized by FCM with an applied field, $B_{app}$ = 3 T, during the descending stage, also corresponding to ZFCM of the GdBaCuO lens. The trapped field, $B_T$ = 2.85 T, in the $MgB_2$ TFM cylinder was concentrated by the introduction of GdBaCuO lens, and a concentrated magnetic field, $B_c$ = 4.73 T, was reliably achieved at the centre of the lens. In "case-2," using the outer GdBaCuO TFM cylinder and inner GdBaCuO lens pair, a higher $B_c$ = 13.49 T, was reliably achieved at the centre of the magnetic lens for $B_{app}$ = 10 T.

This HTFML device could be new from the reason that the trapped field is improved from viewpoints of the magnetizing technique in contrast with a conventional approach by only superconducting characteristics itself.

## Chapter 3: Design Optimization of a Hybrid Trapped Field Magnet Lens (HTFML)

For the design of the magnetic lens, a systematic investigation was carried out by a numerical simulation. Each geometric parameter of the magnetic lens was varied, and a concentrated field at the center were compared. The HTFML with an optimized lens can achieve concentrated magnetic fields of $B_c$ = 5.6 and 12.8 T at the center of the lens for applied magnetic fields of $B_{app}$ = 3 and 10 T, respectively. More practically, the mechanical stress was also estimated in the HTFML. For $B_{app}$ = 10 T, a maximum tensile stress of 35 and 135 MPa exist in the magnetic lens and the TFM cylinder, respectively, during the magnetizing process. These results suggest that adequate mechanical reinforcement is needed in a practical design in order to avoid mechanical fracture at high magnetic

fields.

## Chapter 4: Experimental realization of a hybrid trapped field magnet lens using a GdBaCuO magnetic lens and $MgB_2$ bulk cylinder

The author's group has first verified a concept of the HTFML using GdBaCuO magnetic lens and $MgB_2$ TFM cylinder, experimentally. A maximum concentrated magnetic field of $B_c$ = 3.55 T was achieved in the central bore of the HTFML device after removing an applied field of $B_{app}$ = 2.0 T at T = 20 K. The maximum $B_c$ value was smaller than the one estimated by numerical simulations, which results from the lower $J_c$ ($B$, $T$) of the outer $MgB_2$ cylinder, compared with those of the numerical predictions. For higher $B_{app}$, the $B_c$ value was not enhanced because of the lower $J_c$ ($B$, $T$) of the outer $MgB_2$ cylinder. In other words, to resolve this issue and realize a higher $B_c$, the most important thing in the magnetic and thermal design of the HTFML is that the outer TFM cylinder can replace an external coil magnet with a comparatively homogeneous magnetic field.

## Chapter 5: Experimental realization of a 10 T-class, all-(RE)BaCuO hybrid trapped field magnet lens

In the HTFML, the outer TFM cylinder should be kept at a certain high temperature over $T_c$, in principle, until the ZFCM process of the inner magnetic lens finished. An all-(RE)BaCuO HTFML system was verified under 50 K, using only one cryocooler and a special technique named the "loose contact method", where the outer TFM was loosely connected to the cold stage before magnetizing process by introducing a gap between the cold stage. A maximum concentrated field of $B_c$ = 9.8 T was achieved after magnetization with an applied field of $B_{app}$ = 7 T, which is twice as superior as the other HTFML devices with $B_{app}$ (= $B_T$) up to 3 T to date. During magnetization with a higher $B_{app}$ of 10 T, the $B_c$ value suddenly dropped due to the occurrence of a large flux jump that resulted in the mechanical fracture of the bottom bulk in the stacked TFM cylinder, even though mechanical reinforcement using a stainless-steel support was applied. There are no other reports for which the TFM cylinder was utilized with such a high field. Hence, to realize a $B_c$ value of over 10 T, further fundamental investigations are needed relating to the thermal stability of the stacked TFM cylinder.

## Chapter 6: Simulation study for magnetic levitation in pure water exploiting the ultra-high magnetic field gradient product of a hybrid trapped filed magnet lens (HTFML)

As another applicational prospects, the author presented a new advantage of the HTFML by numerical simulations, other than the ability to provide a continuous, concentrated magnetic field higher than the applied field reported previously: exploiting the HTFML's ultra-high magnetic field gradient product, $B_z \cdot dB_z/dz$, which could be highly applicable to magnetic levitation and separation.

The HTFML device consisting of a GdBaCuO TFM cylinder and GdBaCuO magnetic lens after magnetization from 10 T can generate a concentrated magnetic field, $B_c$, of 11.4 T and a $B_z \cdot dB_z/dz$ over $\pm$3,000 $T^2/m$, which is higher than that of other superconducting magnets (SM) and large-scale hybrid magnets (HM) around the world. The HTFML device enables the design of a compact and mobile desktop-type superconducting bulk magnet system and can improve the accessibility to strong magnetic fields in a variety of food, medical and industrial applications.

## Chapter 7: A conceptual study of a High Gradient Trapped Field Magnet (HG-TFM) toward providing a quasi-zero gravity space on Earth

For the high field application which require the strong magnetic force, there are some trends related to the magnet design, *i.e.*, the improvement of magnetic field $B_z$ and/or magnetic field gradient $dB_z/dz$. The previous HTFML would have some issues on the versatility of operation as a desktop-type magnet device that requires a longer, complex magnetizing process exploiting ZFCM and FCM and provide a narrower open bore below 10 mm.

The author proposed a new concept of a High Gradient Trapped Field Magnet (HG-TFM) using numerical simulation. The HG-TFM is made from (RE)BaCuO bulk superconductors, in which a slit ring bulk (slit-TFM) that generate the minus, trapped field inversely, was tightly stacked with a conventional, large stacked TFM cylinder (full-TFM). A maximum value of the magnetic field gradient product of $B_z \cdot dB_z/dz$ = -6040 $T^2/m$ was obtained after conventional FCM from $B_{app}$ = 10 T of the HG-TFM with a 60 mm outer diameter and 10 mm inner diameter. This value may be the highest ever reported compared to any other magnetic sources. The superiority of the HG-TFM is the easier magnetization process including a single temperature and a simpler construction without any additional cost. A quasi-zero gravity space can be provided in a compact, cryogen-free desktop-type HG-TFM device, which would be installed even in the laboratory scale and applicable to scientific research, such as in the life/medical sciences for protein crystallization and cell culture.

# Acknowledgements

First, I would like to express my sincere gratitude to my honored supervisor Prof. Hiroyuki Fujishiro for his supervision these past five years. Thank you for providing me this precious opportunity to continue the applicational study leading the field of the bulk superconductivity. Besides, I deeply thank to my co-author Dr. Mark D Ainslie of University of Cambridge, U. K., who supported me to discuss the latest news at the forefront of research.

I would like to thank the rest of committee members: Prof. Yasuhiro Kamada and Prof. Michiaki Matsukawa, for their valuable comments and discussions. I am also grateful to the Iwate University staff. This research would not have been possible without their grateful supports to the research activity, but also any financial supports. Thanks also to the members of Prof. Tomoyuki Naito's laboratory. Without their grateful supports, I would have never finished this outstanding work within one and half of year in Ph.D. course.